# A PSEUDOSPECTRAL ANALYSIS OF LAMINAR NATURAL CONVECTION FLOW AND HEAT TRANSFER BETWEEN TWO INCLINED PARALLEL PLATES

A THESIS SUBMITTED TO
THE GRADUATE SCHOOL OF NATURAL AND APPLIED SCIENCES
OF
MIDDLE EAST TECHNICAL UNIVERSITY

BY

SERKAN KASAPOĞLU

IN PARTIAL FULFILLMENT OF THE REQUIREMENTS
FOR
THE DEGREE OF MASTER OF SCIENCE
IN
MECHANICAL ENGINEERING

SEPTEMBER 2005

Approval of the Graduate School of Natural and Applied Sciences

Prof Dr. Canan Özgen
Director

I certify that this thesis satisfies all the requirements as a thesis for the degree of Master of Science.

Prof. Dr. Kemal İder
Head of Department

This is to certify that we have read this thesis and that in our opinion it is fully adequate, in scope and quality, as a thesis for the degree of Master of Science .

Asst. Prof. Dr. İlker Tarı
Supervisor

Examining Committee Members

Instructor Dr. Tahsin Çetinkaya (METU, ME)

Asst. Prof. Dr. İlker Tarı (METU, ME)

Asst. Prof. Dr. Cüneyt Sert (METU, ME)

Asst. Prof. Dr. Derek Baker (METU, ME)

Dr. Ayhan Yılmazer (Hacettepe Unv., NEE)

**I hereby declare that all information in this document has been obtained and presented in accordance with academic rules and ethical conduct. I also declare that, as required by these rules and conduct, I have fully cited and referenced all material and results that are not original to this work.**

Name, Last Name: Serkan KASAPOĞLU

Signature :

# ABSTRACT

## A PSEUDOSPECTRAL ANALYSIS OF LAMINAR NATURAL CONVECTION FLOW AND HEAT TRANSFER BETWEEN TWO INCLINED PARALLEL PLATES

Kasapoğlu, Serkan
MS., Department of Mechanical Engineering
Supervisor : Asst. Prof. Dr. İlker Tarı
September 2005, 110 pages

Three dimensional laminar natural convection flow of and heat transfer in incompressible air between two inclined parallel plates are analyzed with the Boussinesq approximation by using spectral methods. The plates are assumed to be infinitely long in streamwise and spanwise directions. For these directions, periodic boundary conditions are used and for the normal direction constant wall temperature and no slip boundary conditions are used. Unsteady Navier-Stokes and energy equations are solved using a pseudospectral C code in order to obtain velocity and temperature profiles inside the channel. Fourier series are used to expand the variables in x and z directions, while Chebyshev polynomials are used to expand the variables in y direction. By using the temperature distribution between the plates, local and average Nusselt numbers (Nu) are calculated. Nu values are correlated with $\varphi$ ,which is the inclination angle, and with $Ra \cos\varphi$ to compare the results with the literature. Additionally, non-dimensional velocity values and streamlines of the fluid are presented with proper plots.

Keywords: Natural Convection, Spectral Methods, Inclined Parallel Plates.

# ÖZ

## EĞİK İKİ PARALEL PLAKA ARASINDAKİ LAMİNER DOĞAL KONVEKSİYON AKIŞIN VE ISI TRANSFERİNİN PSEUDOSPEKTRAL ANALİZİ

Kasapoğlu, Serkan
Yüksek Lisans, Makine Mühendisliği Bölümü
Tez Yöneticisi: Yard. Doç. Dr. İlker Tarı
Eylül 2005, 110 sayfa

Eğik iki paralel plaka arasındaki sıkıştırılamaz ve Boussinesq varsayımlı havanın üç boyutlu laminer doğal konveksiyon akışı ve ısı transferi spektral metodlar kullanılarak analiz edildi. Plakalar akış yönünde, ve genişlik yönünde sonsuz uzunlukta kabul edildi. Bu yönlerde periyodik sınır şartları kullanıldı, yüzeye dik yönde ise sabit duvar sıcaklığı ve kaygan olmayan sınır şartları kullanıldı. Kanal içindeki hız ve sıcaklık profillerini elde etmek için zamana bağlı Navier-Stokes ve enerji denklemleri pseudospektral C kodu vasıtasıyla çözüldü. Fourier serisi, değişkenleri x ve z yönünde açmak için, Chebyshev polinomları ise değişkenleri y yönünde seriye açmak için kullanıldı. Plakalar arasındaki sıcaklık dağılımı kullanılarak lokal ve ortalama Nusselt sayıları hesaplandı. Literatür çalışmalarıyla karşılaştırma yapabilmek için, Nu değerleri $\varphi$ ve $Ra\cos\varphi$ ile ilişkilendirildi. Buna ek olarak akışkanın boyutsuz hız değerleri ve akış çizgileri uygun grafiklerle sunuldu.

Anahtar Kelimeler: Doğal Konveksiyon, Spektral Metodlar, Eğik Paralel Plakalar.

*To my family and my love, Hande*

# ACKNOWLEDGEMENTS

I would like to express my deepest gratitude to my supervisor, Asst. Prof. Dr. İlker Tarı for his guidance, patience and invaluable help throughout this study.

I would also like to thank Prof. Dr. Hafit Yüncü and Prof. Dr. Zafer Dursunkaya for sharing their valuable theoretical and practical knowledge throughout my Master of Science program.

I wish to express my pleasure to my heat transfer colleagues; Barbaros Çetin, Elif Dirgin, Özgür Bayer, Yavuz Kayserilioğlu, and to heat transfer laboratory technician Mr. Mustafa Yalçın for their support and motivation during my graduate study.

I am really grateful especially to my friends; Cenk Evren Kükrer, Enver Doruk Özdemir, Tahsin Çağrı Şişman, Etkin Özen for their continuous help and contributions throughout this study. Finally I want to thank my officemates Erdinç İyiay and Pınar Kafalı for their patience especially on my last months and for providing me entertaining moments during my study.

# TABLE OF CONTENTS

PLAGIARISM ........................................................................................... iii
ABSTRACT ............................................................................................. iv
ÖZ............................................................................................................ v
ACKNOWLEDGEMENTS ...................................................................... vii
TABLE OF CONTENTS ........................................................................ viii
LIST OF TABLES ................................................................................... xi
LIST OF FIGURES................................................................................. xii
NOMENCLATURE................................................................................ xvi

CHAPTERS

1. INTRODUCTION.................................................................................. 1
  1.1. Objective ........................................................................................ 1
  1.2. The Considered Domain................................................................. 2
  1.3. The Phenomenon............................................................................ 3
  1.4. Organization of the Thesis ............................................................ 4
2. LITERATURE SURVEY ....................................................................... 5
  2.1. Literature for the Natural Convection Flow between Two Inclined Parallel Plates ....................................................................................... 5
    2.1.1. Experimental Studies................................................................ 5
    2.1.2. Numerical Studies .................................................................... 9
  2.2. Literature for the Natural Convection Flow over the Inclined Flat Plate.......................................................................................... 10
    2.2.1. Experimental Studies.............................................................. 10
    2.2.2. Analytical and Numerical Studies .......................................... 12

3. SPECTRAL METHODS .................................................. 15
3.1. Introduction .................................................. 15
3.1.1. Method of Weighted Residuals .................................................. 15
3.1.2. Comparison of Spectral Methods with Finite Element and Finite Difference Methods .................................................. 17
3.2. Fourier series .................................................. 19
3.2.1. Calculation of Fourier coefficients .................................................. 20
3.2.2. Discrete Fourier series .................................................. 21
3.2.3. Fast Fourier Transform .................................................. 22
3.3. Chebyshev Methods .................................................. 23
3.3.1. Chebyshev Polynomials .................................................. 23
3.3.2. Calculation of Chebyshev coefficients .................................................. 24
3.3.3. Discrete Chebyshev series and Collocation Method .................................................. 24
3.4. Description of Temporal Discretization Techniques .................................................. 26
3.4.1. Two-step methods .................................................. 27
3.4.1.1. Semi-implicit AB/CN Scheme .................................................. 28
3.4.1.2. Semi-implicit AB/BDI2 Scheme .................................................. 28
4. SPECTRAL METHODS SOLUTION OF THE GOVERNING EQUATIONS .................................................. 29
4.1. Geometry, Domain and Assumptions .................................................. 29
4.2. Formulation of Governing Equations .................................................. 30
4.3. Solution of N-S by Using Spectral Methods .................................................. 33
4.3.1. Reformulation of the Problem .................................................. 33
4.3.2. Series Expansion .................................................. 39
4.3.3. Temporal Discretization .................................................. 39
4.3.3.1. Semi-implicit AB/CN Scheme .................................................. 40
4.3.3.2. Semi-implicit AB/BDI2 Scheme .................................................. 41

4.3.4. Spatial Discretization ........ 43
  4.3.4.1. Semi-implicit AB/CN Scheme ........ 43
  4.3.4.2. Semi-implicit AB/BDI2 Scheme ........ 45
4.3.5. Spectral Integration of N-S ........ 48
4.3.6. Computational Procedure ........ 54
5. RESULTS AND DISCUSSION ........ 58
5.1. Introduction ........ 58
5.2. Calculation of Nusselt (Nu) Number ........ 60
5.3. The Convergence Criteria ........ 63
5.4. Comparison of AB/CN and AB/BDI2 Schemes ........ 65
5.5. The Results of 3-D Runs for Air ........ 68
5.6. Analysis of a Sample Case with a Finer Grid (64 x 128 x 64) ........ 100
5.7. Critical Tilt Angle Analysis ........ 103
6. CONCLUSION ........ 105
REFERENCES ........ 108

# LIST OF TABLES

Table 5.1. The Maximum and Minimum Average Nu Values with the Average Nu Values obtained by Eqns. 5.8-9 when t* = 2-10 ....... 64

Table 5.2. Average Nu Values of Present Study with Eqns. 5.8-9 and Relative Percentage Error Values of Present Study with respect to Eqns. 5.8-9 ............................................................ 99

Table 5.3. Average Nu Values for three grid arrangements......................... 100

# LIST OF FIGURES

Figure 1.1. Computational domain of inclined parallel plates with an inclination angle $\varphi$ from the horizontal. ........ 2

Figure 3.1. Illustration of three types of refinements [28] ........ 18

Figure 5.1. Dimensionless u versus $t^*$ when $Ra = 20000$ and $\varphi = 15^\circ$ with AB/BDI2 Scheme at [32][16][16] ........ 66

Figure 5.2. Dimensionless u versus $t^*$ when $Ra = 20000$ and $\varphi = 15^\circ$ with AB/CN Scheme at [32][16][16] ........ 66

Figure 5.3. Dimensionless u versus $t^*$ when $Ra\, cos\, \varphi = 10000$ and $\varphi = 15^\circ$ with AB/CN Scheme at [2][2][2] ........ 67

Figure 5.4. Average Nu value versus $t^*$ where $Ra\, cos\, \varphi = 1708$ and $\varphi = 15^\circ$ ........ 69

Figure 5.5. Streamlines in y-z plane when $Ra \cos \varphi = 1708$ and $\varphi = 15^\circ$ at $t^* = 6$ ........ 70

Figure 5.6. Local Nu value in streamwise direction where $Ra\, cos\, \varphi = 10000$ and $\varphi = 15^\circ$ ........ 71

Figure 5.7. Local Nu value in spanwise direction where $Ra\, cos\, \varphi = 10000$ and $\varphi = 15^\circ$ ........ 72

Figure 5.8. Streamlines in y-z plane when $Ra \cos \varphi = 10000$ and $\varphi = 15^\circ$ at $t^* = 6$ ........ 72

Figure 5.9. Average Nu value versus $t^*$ where $Ra\, cos\, \varphi = 10000$ and $\varphi = 15^\circ$ ........ 73

Figure 5.10. Local Nu value in streamwise direction where $Ra\, cos\, \varphi = 50000$ and $\varphi = 15^\circ$ ........ 74

Figure 5.11. Local Nu value in spanwise direction where $Ra\,cos\,\varphi = 50000$ and $\varphi = 15^{\circ}$ .......... 75

Figure 5.12. Streamlines in y-z plane when $Ra\cos\varphi = 50000$ and $\varphi = 15^{\circ}$ at $t^{*} = 10$ .......... 76

Figure 5.13. Average Nu value versus $t^{*}$ where $Ra\,cos\,\varphi = 50000$ and $\varphi = 15^{\circ}$ .......... 77

Figure 5.14. Average Nu value versus $t^{*}$ where $Ra\,cos\,\varphi = 1708$ and $\varphi = 30^{\circ}$ .......... 77

Figure 5.15. Local Nu value in streamwise direction where $Ra\,cos\,\varphi = 10000$ and $\varphi = 30^{\circ}$ .......... 78

Figure 5.16. Local Nu value in spanwise direction where $Ra\,cos\,\varphi = 10000$ and $\varphi = 30^{\circ}$ .......... 79

Figure 5.17. Streamlines in y-z plane when $Ra\cos\varphi = 10000$ and $\varphi = 30^{\circ}$ at $t^{*} = 7$ .......... 80

Figure 5.18. Average Nu value versus $t^{*}$ where $Ra\,cos\,\varphi = 10000$ and $\varphi = 30^{\circ}$ .......... 81

Figure 5.19. Average Nu value versus $t^{*}$ where $Ra\,cos\,\varphi = 50000$ and $\varphi = 30^{\circ}$ .......... 81

Figure 5.20. Streamlines in y-z plane when $Ra\,cos\,\varphi = 50000$ and $\varphi = 30^{\circ}$ at $t^{*} = 10$ .......... 82

Figure 5.21. Streamlines in x-y plane when $Ra\,cos\,\varphi = 50000$ and $\varphi = 30^{\circ}$ at $t^{*} = 10$ .......... 82

Figure 5.22. Dimensionless $u$ versus $t^{*}$ where $Ra\,cos\,\varphi = 1708$ and $\varphi = 15^{\circ}$ at [2][2][2] .......... 83

Figure 5.23. Dimensionless υ versus $t^{*}$ where $Ra\,cos\,\varphi = 1708$ and $\varphi = 15^{\circ}$ at [2][2][2] .......... 84

Figure 5.24. Dimensionless $w$ versus $t^*$ where $Ra\,cos\,\varphi = 1708$ and $\varphi = 15^\circ$ at [2][2][2] ........ 84

Figure 5.25. Dimensionless $u$ versus $t^*$ where $Ra\,cos\,\varphi = 10000$ and $\varphi = 15^\circ$ at [2][2][2] ........ 85

Figure 5.26. Dimensionless $\upsilon$ versus $t^*$ where $Ra\,cos\,\varphi = 10000$ and $\varphi = 15^\circ$ at [2][2][2] ........ 86

Figure 5.27. Dimensionless $w$ versus $t^*$ where $Ra\,cos\,\varphi = 10000$ and $\varphi = 15^\circ$ at [2][2][2] ........ 86

Figure 5.28. Dimensionless $u$ versus $t^*$ where $Ra\,cos\,\varphi = 50000$ and $\varphi = 15^\circ$ at [2][2][2] ........ 87

Figure 5.29. Dimensionless $\upsilon$ versus $t^*$ where $Ra\,cos\,\varphi = 50000$ and $\varphi = 15^\circ$ at [2][2][2] ........ 88

Figure 5.30. Dimensionless $w$ versus $t^*$ where $Ra\,cos\,\varphi = 50000$ and $\varphi = 15^\circ$ at [2][2][2] ........ 88

Figure 5.31. Dimensionless $u$ versus $t^*$ where $Ra\,cos\,\varphi = 1708$ and $\varphi = 30^\circ$ at [2][2][2] ........ 89

Figure 5.32. Dimensionless $\upsilon$ versus $t^*$ where $Ra\,cos\,\varphi = 1708$ and $\varphi = 30^\circ$ at [2][2][2] ........ 90

Figure 5.33. Dimensionless $w$ versus $t^*$ where $Ra\,cos\,\varphi = 1708$ and $\varphi = 30^\circ$ at [2][2][2] ........ 90

Figure 5.34. Dimensionless $u$ versus $t^*$ where $Ra\,cos\,\varphi = 10000$ and $\varphi = 30^\circ$ at [2][2][2] ........ 91

Figure 5.35. Dimensionless $\upsilon$ versus $t^*$ where $Ra\,cos\,\varphi = 10000$ and $\varphi = 30^\circ$ at [2][2][2] ........ 92

Figure 5.36. Dimensionless $w$ versus $t^*$ where $Ra\,cos\,\varphi = 10000$ and $\varphi = 30^\circ$ at [2][2][2] ........ 92

Figure 5.37. Dimensionless $u$ versus $t^*$ where $Ra\,cos\,\varphi = 50000$ and $\varphi = 30^\circ$ at [2][2][2] ........ 93
Figure 5.38. Dimensionless $\upsilon$ versus $t^*$ where $Ra\,cos\,\varphi = 50000$ and $\varphi = 30^\circ$ at [2][2][2] ........ 94
Figure 5.39. Dimensionless $w$ versus $t^*$ where $Ra\,cos\,\varphi = 50000$ and $\varphi = 30^\circ$ at [2][2][2] ........ 94
Figure 5.40. Average Nu versus $Ra\,cos\,\varphi$ where $\varphi = 15^\circ$ ........ 95
Figure 5.41. Average Nu versus $Ra\,cos\,\varphi$ where $\varphi = 30^\circ$ ........ 96
Figure 5.42. Average Nu versus $Ra\,cos\,\varphi$ where $\varphi = 45^\circ$ ........ 97
Figure 5.43. Average Nu versus $Ra\,cos\,\varphi$ where $\varphi = 60^\circ$ ........ 98
Figure 5.44. Local Nu value in streamwise direction where $Ra\,cos\,\varphi = 10000$ and $\varphi = 15^\circ$ with $64 \times 128 \times 64$ grid arrangement ........ 101
Figure 5.45. Local Nu value in spanwise direction where $Ra\,cos\,\varphi = 10000$ and $\varphi = 15^\circ$ with $64 \times 128 \times 64$ grid arrangement ........ 102
Figure 5.46. Average Nu value versus $t^*$ where $Ra\,cos\,\varphi = 10000$ and $\varphi = 15^\circ$ with $64 \times 128 \times 64$ grid arrangement ........ 102
Figure 5.47. Average Nu value versus tilt angle for $Ra = 20000$ and $\Pr = 0.7$ for two dimensional case ........ 104
Figure 5.48. Average Nu versus tilt angle when $Ra\,cos\,\varphi = 3500$ for three dimensional case ........ 104

# NOMENCLATURE

| | |
|---|---|
| $w_*$ | weight function used in Eqn. (3.4) |
| $I_N$ | dimension of the discrete set of Eqn. (3.4) |
| $\delta$ | Dirac-delta function |
| $\delta_{k,l}$ | Kronecker delta |
| a | advective velocity term used in Eqn. (3.37) |
| $\varepsilon$ | arbitrary constant used in Eqn. (3.38) |
| $\gamma_1, \gamma_2$ | arbitrary constants used in Eqn. (3.38) |
| $\theta_1, \theta_2$ | arbitrary constants used in Eqn. (3.38) |
| $\partial_x, \partial_y, \partial_z$ | first order partial derivatives with respect to x, y and z, respectively |
| $\partial_{xx}, \partial_{yy}, \partial_{zz}$ | second order partial derivatives with respect to x, y and z, respectively |
| $D^2$ | second order partial derivative with respect to y |
| $u$ | velocity in the streamwise direction, m/s |
| $\upsilon$ | velocity in the normal direction, m/s |
| $w$ | velocity in the spanwise direction, m/s |
| $\bar{L}$ | characteristic length, m |
| $\bar{U}$ | characteristic velocity, m/s |
| Re | Reynolds number, $Re = \dfrac{\bar{L}\bar{U}}{\nu}$ |
| Pr | Prandtl number, $Pr = \dfrac{\nu}{\alpha}$ |
| Ra | Rayleigh number, $Ra = \dfrac{\bar{L}^3 \beta \mathbf{g} \Delta T}{\alpha \nu}$ |

| | |
|---|---|
| Nu | Nusselt number |
| T | fluid temperature, K |
| $p$ | pressure, kPa |
| $g$ | gravitational acceleration, $\mathrm{m/s^2}$ |
| $L_x, L_y, L_z$ | distance defined in the x, y and z directions, respectively for the computational domain |
| $\omega_x, \omega_y, \omega_z$ | vorticity components in $x, y, z$ directions, respectively |
| x | streamwise coordinate |
| y | normal coordinate |
| z | spanwise coordinate |
| t | time, s |
| h | convective heat transfer coefficient, $\mathrm{W/m^2K}$ |
| k | thermal conductivity, $\mathrm{W/mK}$ |
| FFT | Fast Fourier Transform |
| AB/BDI2 | Adams-Bashforth / Backward-Differentiation |
| AB/CN | Adams-Bashforth / Crank-Nicolson |

Greek Symbols

| | |
|---|---|
| $\nu$ | kinematic viscosity, $\mathrm{m^2/s}$ |
| $\beta$ | thermal expansion coefficient of the fluid, $\mathrm{K^{-1}}$ |
| $\alpha$ | thermal diffusivity of the fluid, $\mathrm{m^2/s}$ |
| $\varphi$ | inclination angle from horizontal |
| $\theta$ | temperature difference between the fluid and the upper wall |
| $\alpha_1, \alpha_2$ | wavenumbers in x and z directions, respectively |

### Subscripts

| | |
|---|---|
| p | particular solution |
| i, j, k | locations in x, y and z directions, respectively |
| w | wall values |
| $\infty$ | bulk property of the fluid |

### Superscripts

| | |
|---|---|
| * | non-dimensional parameters |
| n | location in time |
| ~, ^ | variables in Fourier and Chebyshev space, respectively |

# CHAPTER 1

# INTRODUCTION

Fluid motions that develop related to the action of a body force field such as the gravitational field are called natural flows and heat transfer corresponding to such flows is known as natural or free convection. These flows can also be called buoyancy induced flows because the movement of the fluid results from the buoyancy forces that arise from density differences, which stem from the instabilities in temperature, fluctuations in concentration of chemical species and many other effects [1].

Natural convection flow in an inclined channel or an inclined tube is especially useful to drive the fluid during the heat transfer process. Before pumping, inclined tubes and channels were used widely in heat exchangers and steam generators.

## 1.1. Objective

In this study, natural convection flow between two inclined parallel plates is simulated numerically. A pseudospectral method based computer code is used in order to obtain the velocity and temperature fields by solving Navier-Stokes and energy equations. Using the temperature field and from wall temperature, gradient local and average Nusselt numbers (Nu) are calculated. The change of Nu with the inclination angle from the horizontal is investigated.

Additionally, the critical tilt angle for air is calculated and compared with the literature. The previous studies in the literature are either experimental or numerical with low order methods such as finite difference and finite element. Using a higher order pseudospectral method, better accuracy is expected to be obtained. Instead of solving boundary layer equations, Navier-Stokes equations are expanded in Fourier series in streamwise and spanwise directions, and Chebyshev polynomials in the direction normal to the plates. After the discretizations in time and space are performed, the resulting tridiagonal matrix equations are solved.

## 1.2. The Considered Domain

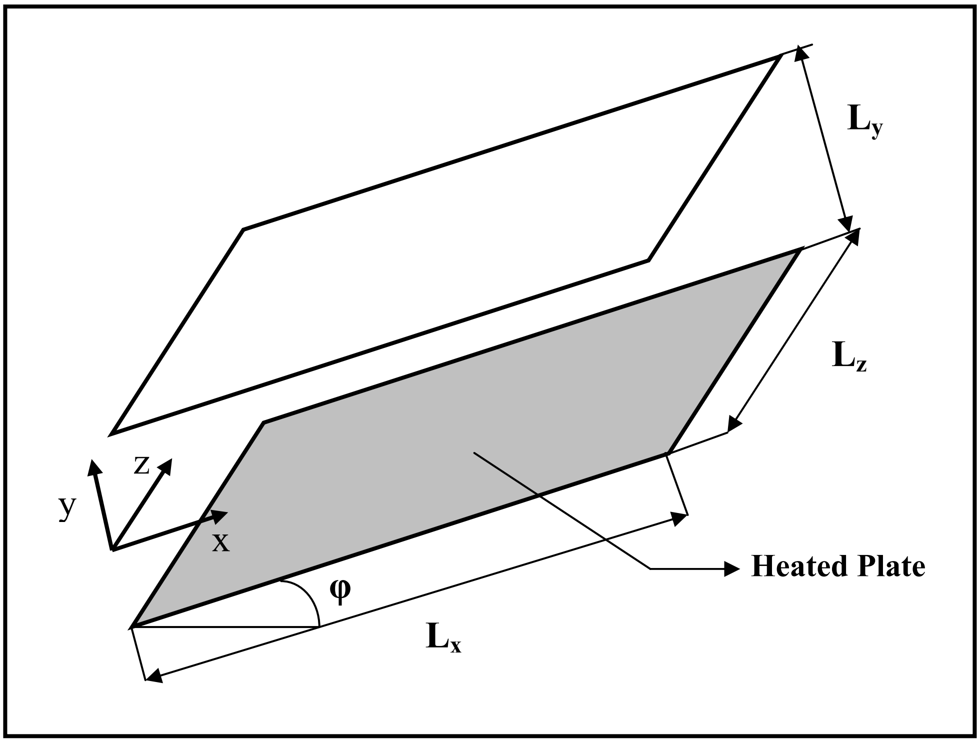

**Figure 1.1.** Computational domain of inclined parallel plates with an inclination angle $\varphi$ from the horizontal.

The domain shown in Figure 1.1 is an inclined channel between two parallel plates. $L_x = L_z = 2\pi$ and $L_y = 2$ . The plate dimensions are $L_x \times L_z$ . In both streamwise (x) and spanwise (z) directions, velocity and thermal boundary conditions are periodical. Therefore the model represents a part of an infinite channel far away from the entrance. On plates no-slip conditions exist. The plate temperature distribution can be specified and bottom plate temperature is always higher than that of the upper plate. Thus the fluid is driven with buoyancy effects.

The channel inclination angle from the horizontal, $\varphi$ can be selected freely. There exist an angle at which the flow mode transition occurs and Nu becomes minimum. That angle is called the critical tilt angle. One of the objectives of this study is also to determine the critical tilt angle for air with the numerical method.

## 1.3. The Phenomenon

When an inclined channel is heated from below and if the channel is open on both ends, the fluid flows due to temperature induced density differences. The main flow direction is the x direction but there also form some vortex structures in y-z plane carrying fluid between the bottom and the top plate. The phenomenon itself is an inherent thermally driven hydrodynamical instability.

A similar event occurs for the single inclined heated plate case. In that case, the formed vortex structures are called longitudinal vortices [2]. Their existence and their contributions on enhancement of heat transfer is shown in the literature.

Even though, the literature of both the single inclined plate and the inclined channel between two inclined plates are investigated, only the latter one is numerically examined.

Another case may be the enclosure between two plates. In that case, somewhat regular convection cells form. The general form of the structure remains the same regardless of the inclination angle.

Among all these cases, the buoyancy driven flow between two parallel inclined plates is considered as the most appropriate one. Since to analyze each one of these phenomena requires a totally different model, the channel case is selected for our investigation.

## 1.4. Organization of the Thesis

Following this general introduction, the introduction to the previous literature is given in Chapter 2. Chapter 3 presents the general information about the spectral methods that are used in this study. In Chapter 4, the solution details of the governing equations are presented. The results are given and discussed in Chapter 5. The thesis concludes with general remarks about the results with the Conclusion Chapter.

# CHAPTER 2

# LITERATURE SURVEY

In this chapter, the literature of the inclined buoyancy driven flows for both the flat plate case and the channel between the parallel plates are examined.

## 2.1. Literature for the Natural Convection Flow between Two Inclined Parallel Plates

### 2.1.1. Experimental Studies

Ruth, Hollands, and Raithby [3] analyzed experimentally heat transfer and natural convective motion in inclined air layers heated from below, for inclination angles of $0 \leq \varphi \leq 30^{\circ}$ and the product of Rayleigh number (Ra) with cosine of the tilt angle ($\varphi$) $100 < Ra \cos\varphi < 10000$. In this study, it is investigated that as is first noted by Hollands et al. [4], the experimental heat transfer values for $\varphi$ of larger than $20^{\circ}$ are not only dependent on $Ra \cos\varphi$ as expected from theoretical analysis. The reason for the difference between the theory and the experiment is referred to in this study as the secondary transition in the streamwise direction.

Hollands, Unny, Raithby, and Konicek [4] demonstrated experimentally free convective heat transfer through inclined air layers of high aspect ratio heated from below. The range of Rayleigh numbers was taken between the subcritical value and $10^5$.

Furthermore, angle of inclination was measured from horizontal between 0 and 70 deg. In this paper, $Ra$ in the horizontal air layer Nusselt number (Nu) correlation was replaced by $Ra\,cos\,\varphi$ to compare the experimental results. But it is understood that this modified horizontal case correlation did not give good results for the immediate postconductive regime. For this reason, it can be readily said that Nu is not only a function of $Ra\,cos\,\varphi$ in that regime.

ElSherbiny, Hollands, and Raithby [5] performed an experimental study of heat transfer by free convection across vertical and inclined air layers. Two parallel isothermal flat plates were used in order to bound the air layer and a wall with low thermal conductivity constant was used around the edges. Measurements were done for the range of Rayleigh numbers from $10^3$ to $10^8$, the various inclinations from horizontal to vertical and an aspect ratio of 5. The effect of emissivity of the bounding wall was also investigated with a low and a high value of the wall emissivity. This study emphasized the requirement for introducing all the related dimensionless groups when presenting results, and helped to elucidate the interaction between the boundaries and the fluid flow.

Dropkin and Somerscales [6] presented an experimental investigation of buoyancy induced flow in liquids bounded by two parallel plates with an inclination at various angles from the horizontal. The ranges for the Ra and Pr numbers are given as $5\times10^4$–$7.17\times10^8$, and 0.02-11,560, respectively. The measurements were made in rectangular and circular containers with copper plates and insulating walls. Water, silicone oil and mercury were chosen in order to take into account the properties of the liquids. This paper indicates that Nusselt can be correlated as follows: $Nu = C\ Ra^{1/8}\ Pr^{0.074}$, where C is a constant dependent on the angle of inclination and it varies from 0.069 for horizontal case to 0.049 for vertical case.

ElSherbiny, Raithby, and Hollands [7] made an experimental analysis of natural convection mode of heat transfer across vertical and inclined air layers. Air was confined to flat isothermal plates at different temperatures and temperature was distributed linearly on the edges because of their high conductivity. Measurements were reported for six aspect ratios between 5 and 110. The horizontal aspect ratio was chosen sufficiently large in order not to affect the heat transfer results. The range of Ra is between $10^2$ and $2\times10^7$. This study allowed the role of aspect ratio to be clarified and additionally several heat transfer correlations about across vertical and inclined air layers were presented.

Ozoe, Sayama, and Churchill [8] studied laminar natural convection in silicone oil and air in a long rectangular channel experimentally. The aspect ratio (width/ height) of the cross section of the channel was taken as 1, 2, 3, 4.2, 8.4, 15.5 and Ra was varied between $3\times10^3$ and $10^5$. Moreover, the effect of inclination and of the aspect ratio on the rate of heat transfer was analyzed experimentally. It was concluded that the tilt angle corresponding to the minimum and maximum rates of heat transfer is strongly dependent on the aspect ratio and is weakly dependent on Ra. Furthermore, it was observed that at the angle of minimum heat transfer a transition starts in the mode of circulation.

Azevedo and Sparrow [9] conducted an experimental heat transfer and visualization study in water to examine the effect of the angle of inclination on natural convection in a parallel walled channel. Three types of heating modes were utilized. They can be classified as follows: (I) both walls heated and isothermal, (II) heating from above and (III) heating from below. The discrepancy between Nu correlations when the modes (II) and (III) were used was shown clearly. Moreover, it was observed that recirculation zones can be seen adjacent to the unheated wall of top heated and one sided heated channels. Additionally, longitudinal vortices exist above a critical Ra while heating from below.

Inaba [10] investigated free convection motion and the heat transfer rate in an inclined rectangular air layer experimentally for various tilt angles from 0 to 180 degrees. Additionally, the measurements were performed for different aspect ratios between 5 and 83, and for Rayleigh numbers between $1.2\times10^3$ and $2\times10^6$. Non-dimensional correlations for the heat transfer rate across the air layer were proposed in the relationship between Nu, Ra and the inclination angles.

Onur, Sivrioğlu, and Aktaş [11] demonstrated buoyancy induced air flow between inclined plates with an experimental study. The lower plate was heated isothermally while the upper one was thermally insulated and unheated. The experiments were performed for different temperature differences in order to understand the effect of the plate spacing and inclination on heat transfer. Angles of inclination were taken as $0^\circ$, $30^\circ$ and $45^\circ$ measured from the vertical axis. The separation distance, which is the plate spacing measure between the plates, ranged from 2 mm to 33 mm. As a result, an increase or decrease in heat transfer rate occurs depending on the spacing between plates at any given angle of inclination.

Onur and Aktaş [12] conducted an experimental study in which a hot plate facing downwards was heated isothermally; the lower plate was insulated and unheated in order to study natural convection between inclined plates. Inclination angles were chosen to be $0^\circ$, $30^\circ$ and $45^\circ$ with respect to the vertical. This study was conducted to see the effect of the plate spacing and also the inclination on the natural flow. It can be stated that the separation distance of plates strongly affects the Nu and heat transfer results do not strongly depend on tilt angle.

### 2.1.2. Numerical Studies

Ozoe, Fujii, Lior, and Churchill [13] computed the three dimensional velocity and temperature fields, and the mean Nusselt number of a rectangular enclosure heated from below, perfectly insulated on the lateral surfaces and with an inclination about the longitudinal direction by using a finite difference method. Calculations were restricted to $Ra$ = 4000, $Pr$ = 10, and a single finite grid spacing. The results of this study can be used for theoretical prediction of heat transfer in finite rectangular enclosures, but due to limitations applied in this work, it is incomplete and should be revised for other grid spacings, Pr, and Rayleigh numbers.

Ozoe, Yamamoto, and Churchill [14] have carried out a numerical study to develop theoretical solutions for an inclined three dimensional square channel. Additionally, the critical angle for transition to the two dimensional regime was determined. The finite difference method was used to solve the conservation of mass, energy and momentum equations. These equations were written in terms of the vector potential and the vorticity. It was observed that the average Nu first declines as the angle of inclination is given to the channel, and as the inclination is further increased, Nu increases due to the improved and developed rate of circulation of the single, 2-D roll cell.

Yang and Zhu [15] performed direct numerical simulation of the two dimensional governing equations for natural convection in the inclined parallel walled channel by using the accurate projection method, Pm III. The results of the numerical solution were compared with the experimental data of Azevedo and Sparrow [9]. It was confirmed that when water whose Pr is approximately 5, and spacing ratio of less than 1/20 during the tilt angle ranges from 45 to 90 deg were used, the overall Nu is a monotonic function of the product of the Ra and the ratio of the channel width to the length times the sine of the inclination angle from horizontal.

Başkaya, Aktaş, and Onur [16] studied the effects of plate spacing and angle of inclination on natural convection between asymmetrically heated vertical and inclined parallel plates. The upper heated plate is facing downwards; the lower plate is passively heated by the upper one. The angles of inclination were taken same as taken in Onur et al [11]. The governing equations were solved by using a commercial computational code PHOENICS. Computational results were compared with experimental data from the literature. It can be concluded from this study that, the spacing between the plates affects the overall heat transfer from the channel and heat transfer decreases with an increase in the inclination angle, moreover it increases with increasing Ra.

## 2.2. Literature for the Natural Convection Flow over the Inclined Flat Plate

In addition to the literature review about natural convection in inclined channels, gravity induced convection about an inclined flat plate is also investigated in this thesis. Moreover the existence of longitudinal vortices and their effect on heat transfer are discovered during the survey. For the sake of completeness, papers about free convection over an inclined flat plate are also presented as follows:

### 2.2.1. Experimental Studies

Fujii and Imura [17] conducted an experimental study concerning natural convection heat transfer from an arbitrarily inclined flat plate. Two plates of 30 cm height, 15 cm width and 5 cm height, 10 cm width were heated from one side of the surface. The results were represented in the relation average Nu versus Ra.

For the inclined heated plate facing upwards, it was found that the larger the angle of inclination from the vertical becomes, the smaller the transition Ra becomes. In addition to that, variation of Nusselt numbers with the inclination was illustrated by the change of the flow pattern.

Shaukatullah and Gebhart [18] investigated boundary region flow formed over an inclined surface dissipating uniform heat flux by using a thermocouple and two hot film anemometer probes in the form of inverted V. In this experiment, measurements of temperature, the longitudinal and the transverse components of velocity were made. As a result, a single longitudinal vortex system was observed. Spanwise variation of temperature, velocity fields and also heat transfer stemmed from the aforementioned observation. They also stated that those variations started first for the angles of inclinations from vertical greater than $11^{\circ}$.

Cheng and Kim [19] have made a visualization study for vortex instability of laminar natural convection flow along inclined isothermal plates that have an inclination range of 0 to 20 degrees with 5 degrees increments by using a low speed wind tunnel. The temperature difference between the plate surface and ambient air was taken from 15.5 to 37.5 $^{\circ}$C, and the local Grashof number was from $1.02 \times 10^6$ to $2.13 \times 10^8$. As a consequence of this visualization study, a two-dimensional laminar flow, a transition regime for developing longitudinal vortices and a turbulent regime after the breakdown of longitudinal vortices were observed and identified. It was stated that this experiment provides considerable physical insight into the structure and nature of the developing longitudinal vortices in the transition regime.

Zuercher, Jacobs and Chen [20] conducted experiments to study the longitudinal vortices that emerge in the boundary layer on the upper surface of an inclined isothermally heated plate in water. The inclination angle from vertical was varied from 20 to 60 degrees, and the temperature difference was also chosen from 2 to 23$^{\circ}$C. A double-pass Schlieren system and particle image velocimetry (PIV) were utilized in order to visualize the vortices and measure the velocities, respectively. With the aid of Schlieren images for Pr = 5.8, the wavelength of the vortices and critical modified Reynolds numbers were determined. This study was the first experiment in which the growth rate of the vortices has been found using PIV measurements.

### 2.2.2. Analytical and Numerical Studies

Kierkus [21] made a perturbation analysis for two-dimensional laminar free convection about an inclined isothermal plate, using the classical boundary layer solution as the zeroth order approximation. First order perturbation solution has been found for the velocity and temperature fields. Pr was taken as 0.7 and inclination angles of $0, \pm 15^{\circ}, \pm 30^{\circ}, \pm 45^{\circ}$ were used in order to compare with experimental data. Positive and negative inclination angles were measured with respect to the vertical axis and mean above the plate and below the plate, respectively. Good agreement was found between theoretical and experimental results.

Haaland and Sparrow [22] investigated the linear stability of laminar free convection flow adjacent to a heated, inclined, upward-facing plate to observe the form longitudinal vortices. The problem was formulated in such a manner that basic flow and temperature fields depend on the streamwise coordinate. According to the linear stability theory, basic flow is treated as a parallel flow, but disturbance effects of the transverse velocity of the basic flow can not be ignored. This phenomenon gives rise to disturbance vorticity and temperature to be contained or bottled within the boundary layer of the basic flow. This is called the bottling effect. Two approaches, parallel flow model and non-parallelism of the basic flow were compared in this study.

It is discovered that the critical Grashof numbers of both models differ from each other by several orders of magnitude. It was also shown that when the tilt angle from the vertical is increased, vortex-type instability is more likely to occur.

Chen and Tzuoo [23] studied the vortex instability characteristics of laminar free convection flow over horizontal and inclined isothermal surfaces analytically by using linear stability analysis. The effects of the angle of inclination on the main flow and thermal fields were also examined. The results were presented for wall shear stress, surface heat transfer, neutral stability curve and critical Grashof number for Prandtl numbers of 0.7 and 7 with a wide range of angles of inclination from horizontal. It was stated as a consequence that the greater the angle of inclination, the lower the susceptibility of the flow to the vortex mode of instability.

Lin [24] examined the longitudinal vortex formation in natural convection flow over horizontal and inclined plates numerically. The criterion to decide the position of the onset of longitudinal vortices was defined in this study. Finite difference scheme was used in the purpose of solving the linearized perturbation equations of the flow. After performing such a study, it was revealed that an increase in the tilt angle from horizontal increases the value of critical Grashof number also. Grashof number was found to be also dependent on Prandtl number and wave number. Moreover, the flow was more stable to the vortex mode of instability as the inclination angle was increased due to the decrease in normal buoyancy force. On the other hand, the Prandtl number has been realized to be a destabilizing effect on the flow and the critical values of the Grashof number decrease with an increase in the Prandtl number.

Jeschke and Beer [25] investigated the linear and nonlinear growth of longitudinal vortices and the development of the secondary instabilities in a laminar boundary layer numerically and experimentally. A constant heat flux inclined flat plate in water was chosen for this purpose.

The numerical method was based on a formal perturbation method which leads to a set of governing equations for the linear and nonlinear vortex regime. Nonlinear effects were seen only after a long period of linear vortex growth. Liquid-crystal thermography based on wide-band liquid crystals was used for experimental study to provide full-field, highly accurate wall temperature measurements and visualizations. After comparing the numerical and experimental results, it was clear that vortices cause practically all of the increase of mean heat transfer values during the transition process whereas secondary instabilities only have a minor effect.

Biertümpfel and Beer [26] studied heat transfer from a liquid to a solid wall in natural convection in the regime of transition to turbulent experimentally and numerically. It was observed that firstly three dimensional longitudinal vortices start to grow in the streamwise direction with a pair wise counter-rotating. That means the flow propagates by doing a screw-like motion in x direction. As these laminar vortices grow further, transition from laminar to turbulent occurs with the onset of unsteady, wavy, sinuous-like motion, i.e. secondary instability. It was concluded that the presence of longitudinal vortices lead to an increase in heat transfer, especially in the presence of secondary instabilities in transition stage. This increase was even higher than that was expected for a turbulent flow. Thermochromic liquid crystals were used for experimental measurements and FLUENT was used for numerical simulation of the flow.

# CHAPTER 3

# SPECTRAL METHODS

## 3.1. Introduction

In this chapter, introductory information about the general characteristics of spectral methods is given. The choice of spectral approximation for representation of a given function is shown by using the method of weighted residuals [27]. Additionally, a comparison of spectral methods with finite element and finite difference methods is also given in this section [28]. In the following sections, Fourier and Chebyshev methods are introduced, and several specific applications of these methods, which are used in this thesis, such as Fast Fourier Transform (FFT) and the recurrence relation for differentiation in Chebyshev method, are also presented.

### 3.1.1. Method of Weighted Residuals

In weighted residual methods, functions are approximated in terms of a truncated series expansion as follows:

$$f\left(x\right) \approx f_N\left(x\right) = \sum_{k=0}^{N} \tilde{f}_k \varphi_k\left(x\right) \tag{3.1}$$

where $\tilde{f}_k$ are the expansion coefficients and $\varphi_k\left(x\right)$ are basis functions. There is also a quantity defined as residual which should be equal to zero in an approximate sense by using the following scalar product:

$$(f,g)_w = \int_a^b f(x)g(x)w(x)dx \qquad (3.2)$$

$f(x)$ and $g(x)$ are defined on [a,b] and $w(x)$ is the weight function. The residual function $R_N(x)$ can be defined as:

$$R_N(x) = f(x) - f_N(x) \qquad (3.3)$$

According to the weighted residuals method, $R_N(x)$ can be vanished approximately by setting the following scalar product to zero.

$$(R_N, \psi_i)_{w*} = \int_a^b R_N(x)\psi_i(x)w_*(x)dx = 0, \quad i \in I_N \qquad (3.4)$$

where $\psi_i(x)$ are the test functions, $w_*(x)$ is the weight function. $I_N$ is the dimension of the discrete set and it depends on the problem. Weighted residual methods can be classified into two types of methods with respect to the choice of $\psi_i$ and $w_*$. These are Galerkin-type and collocation method. The Galerkin-type method corresponds to that chosen test functions are equal to basis functions in Eq. (3.1) and are orthogonal with respect to weight functions; on the other hand collocation method can be defined in such a manner that residual function $R_N(x)$ is equal to zero in selected collocation points. In order to do this, weight function and test function are defined as

$$\psi_i = \delta(x - x_i) \text{ and } w_* = 1 \qquad (3.5)$$

where $\delta$ is the Dirac-delta function. $x_i$ are selected on [a,b]. In other words, it can be said that the residual is exactly zero at certain points when collocation method is considered, meanwhile its scalar product is zero in the Galerkin-method.

Spectral methods belong to the family of weighted residual methods and basis functions defined in Eq. (3.1) are orthogonal with respect to some weight function. In order to get more detailed information about Galerkin and Collocation Methods, one can be referred to Peyret [27].

### 3.1.2. Comparison of Spectral Methods with Finite Element and Finite Difference Methods

Finite element methods differ from spectral methods in a basic way that the former ones divide the interval into a number of sub-intervals, and choose local functions of fixed degree which are zero except over a couple of sub-intervals. On the other hand, the latter one uses a global high degree of basis functions as defined in the previous section, e.g. trigonometric polynomials which are non-zero except at isolated points, i.e. collocation points.

Finite element method uses three different ways to increase the accuracy. They can be defined namely as h-refinement, p-refinement and r-refinement. In h-refinement, interval size, h is decreased over the whole domain in order to improve the resolution. In p-refinement, the degree of the polynomials in each subdomain is increased. This is a similar way with the one in spectral methods, in which high degree of global basis functions are used. In r-refinement, only the interval size of the regions where more resolution is needed is diminished. These three types of refinements can be illustrated as in Fig. 3.1.

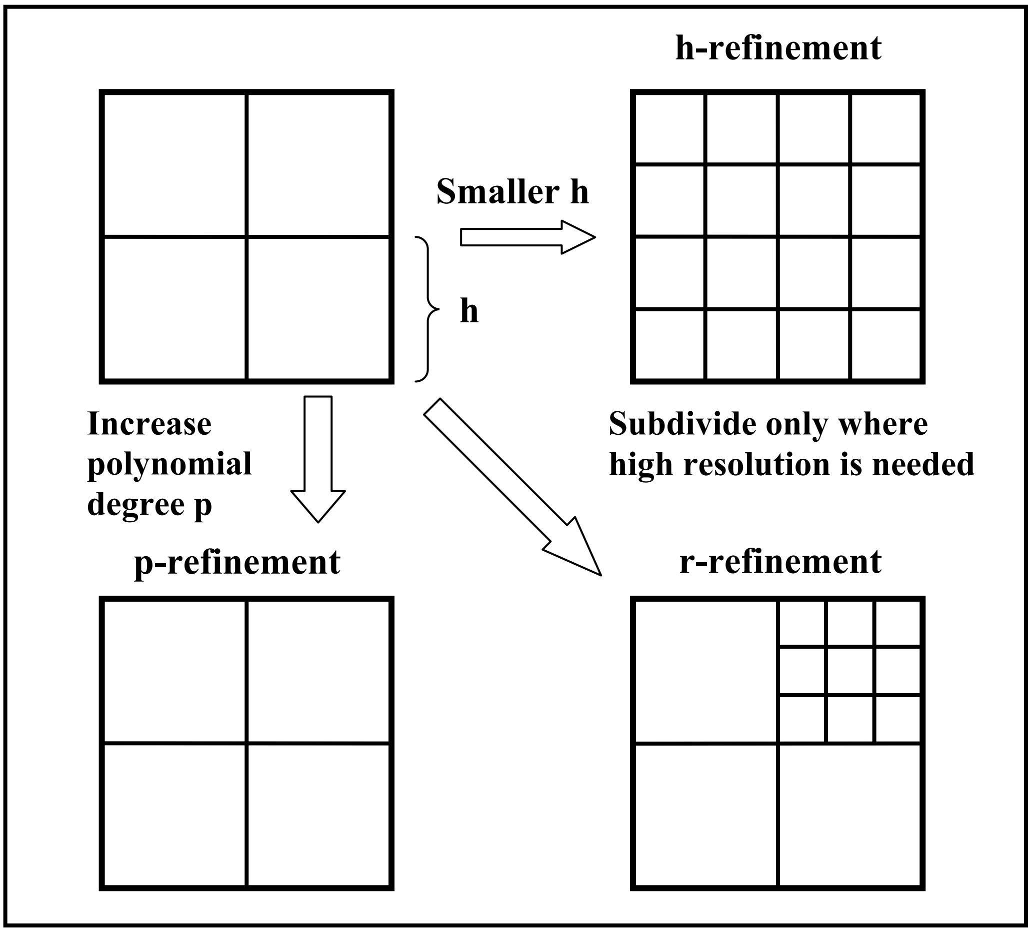

**Figure 3.1.** Illustration of three types of refinements [28]

Finite element methods have two advantages over spectral methods. Firstly, sparse matrix equations can be constructed since local functions are zero except over some sub-intervals. Time-cost is diminished in this way. Secondly, when irregularly shaped geometries are considered, in finite element methods small various geometries can be used in little subintervals. But lower accuracy of a finite element method is the major disadvantage. On the other hand, algebraic equations with full matrices are generated by spectral methods, and high accuracy can be obtained with high order basis functions. However, time cost is increased due to full matrix solvers. Additionally, geometry of the problem should be more smooth and regular.

Finite difference methods use a sequence of overlapping polynomials to approximate the unknown $f(x)$ at the grid points, and also derivatives of local interpolants are used in order to estimate the derivative of $f(x)$. Pseudospectral differentiation formulas are neither three point formulas, like second order finite differences nor even five point formulas like the fourth order finite differences. They are N-point formulas because (N+1) values of desired solution are used to compute (N+1) coefficients of the expansions. For this reason, the order of the method is not fixed, when N, i.e. number of the collocation points, is increased, interval size decreases, and this causes the error to become smaller. Error can be defined in pseudospectral method as $O(h^N)$. Since h is O(1/N), it can readily be seen that error in pseudospectral method becomes $O[(1/N)^N]$. By defining this error term, it can be argued that the error is decreasing faster with an increasing value of N. For more detailed information about accuracy of pseudospectral methods and comparison of them with finite element, and finite difference methods, one can be referred to Boyd [28].

## 3.2. Fourier series

In this section, the basic properties and some special characteristics of Fourier series will be introduced. Calculation of the expansion coefficients is examined by using the Galerkin technique and collocation technique [27]. The second technique is also called Discrete Fourier series. Moreover, FFT technique that is used in this thesis will be discussed [29]. Fourier series have trigonometric basis functions, for this reason they are usually adapted to periodic functions. If the adapted function is not periodic, the convergence of the associated series will not be uniform near the boundaries.

### 3.2.1. Calculation of Fourier coefficients

The function $f\left(x\right)$ can be written in terms of truncated series expansion as in the form of Eq. (3.1) and it can be shown like that;

$$f_K\left(x\right)=\sum_{k=-K}^{K}\tilde{f}_k e^{\underline{i}kx}, \tag{3.6}$$

where $\underline{i}^2$ = -1. There are $2K+1$ complex coefficients to be calculated, however since real $f\left(x\right)$ is assumed, then two expansion coefficients with an opposite indices become complex conjugates:

$$\tilde{f}_{-k}=\overline{\tilde{f}}_k \tag{3.7}$$

and also $\tilde{f}_0$ is real. For this reason, in practice $\tilde{f}_k$ are calculated for $k=0,\ldots,K$ and the other coefficients are found by the help of the Eq. (3.7). The scalar product in Eq. (3.2) is valid with respect to unity as the weight function then Eq. (3.2) becomes:

$$\left(f,g\right)=\int_0^{2\pi} f\bar{g}dx \tag{3.8}$$

by the aid of Eq. (3.8), the orthogonality property of the complex exponential functions can be obtained as follows:

$$\int_0^{2\pi} e^{\underline{i}mx}e^{-\underline{i}nx}dx=\begin{cases}2\pi & \text{if } \ m=n\\ 0 & \text{if } \ m\neq n\end{cases} \tag{3.9}$$

After making these necessary calculations, Fourier expansion coefficients can be readily obtained by using Galerkin-type technique described in Section 3.1.1. In order to do this, the residual function is set equal to zero in the average sense as follows:

$$\begin{aligned}&\left(R_K,e^{\underline{i}lx}\right)=0, \quad l=-K,\ldots,K\\ &R_K=f-f_K\end{aligned} \tag{3.10}$$

by using Eqs. (3.6) and (3.8),

$$\int_{0}^{2\pi}\left[ fe^{-\underline{i}lx} - \sum_{k=-K}^{K} \tilde{f}_k e^{i(k-l)x} \right]dx = 0 \tag{3.11}$$

Finally, $\tilde{f}_k$ can be obtained from Eqs. (3.9) and (3.11) as the expression given below:

$$\tilde{f}_k = \frac{1}{2\pi}\int_{0}^{2\pi} fe^{-\underline{i}kx}dx, \quad k = -K,\dots,K \tag{3.12}$$

In the following section, Fourier coefficients will be calculated by using collocation method, i.e. annulling residual function at the collocation points.

### 3.2.2. Discrete Fourier series

In this section, apart from the Galerkin-type technique, the general technique of collocation is used in order to determine the discrete coefficients of the Fourier series. The collocation points in the Fourier series can be written as:

$$x_i = \frac{2\pi i}{N}, \ i = 0,\dots,N \tag{3.13}$$

Again the function $f(x)$ is assumed as periodic; therefore the value of the function at the first and the last collocation points are equal to each other. The function is expanded in a Fourier series as in the Eq. (3.6):

$$f_K(x) = \sum_{k=-K}^{K} \tilde{f}_k e^{\underline{i}kx} \tag{3.14}$$

Since residual function is equal to zero at collocation points, then by using the definition of residual function in Eq. (3.10), one can obtain

$$\sum_{k=-K}^{K} \tilde{f}_k e^{\underline{i}kx_i} = f(x_i), \quad i = 1,\dots,N. \tag{3.15}$$

Expansion coefficients $\tilde{f}_k$ can be determined by utilizing the discrete orthogonality relation

$$\sum_{i=1}^{N} e^{\underline{i}(k-l)\frac{2\pi i}{N}} = \begin{cases} N & \text{if} \quad k-l=mN,\ m=0,\ \pm 1,\ \pm 2,\dots, \\ 0 & \text{otherwise.} \end{cases} \tag{3.16}$$

Finally by multiplying both sides of Eq. (3.15) with $e^{-\underline{i}lx}$ and taking the sum from $i=1$ to $i=N$. At the last step by using the relation in Eq. (3.16), one can obtain

$$\tilde{f}_k = \frac{1}{N}\sum_{i=1}^{N} f\left(x_i\right) e^{-\underline{i}kx_i},\ k=-K,\dots,K. \tag{3.17}$$

### 3.2.3. Fast Fourier Transform

Fast Fourier Transform (FFT) is the basic and general algorithm for evaluating the discrete Fourier transform and its reverse. One can find the Fourier coefficients of the series by applying Eq. (3.17) and it becomes

$$\tilde{f}_k = \frac{1}{N}\sum_{i=1}^{N} f\left(x_i\right) e^{-\underline{i}k\frac{2\pi i}{N}}, \qquad k=-K,\dots,K \tag{3.18}$$

where $K=\dfrac{N-1}{2}$ from the previous section and $f\left(x_i\right)$ can also be written as

$$f\left(x_i\right) = \sum_{k=-K}^{K} \tilde{f}_k e^{-\underline{i}k\frac{2\pi i}{N}}, \qquad \mathrm{i}=1,\dots,N \tag{3.19}$$

In most applications, the direct use of complex FFT is very time-consuming. For this reason real transform of the FFT is used to get our results more rapidly. All the terms, i.e. real and imaginary terms, are collected as two sets of real data and both parts are examined separately. For further detailed information about FFT and examples of algorithms, one can refer to Canuto et al. [29].

## 3.3. Chebyshev Methods

In this section, general properties of Chebyshev polynomials [27] are introduced. In the previous section, it is stated that because of the non-uniformity at the boundaries, Fourier series are adapted to periodic functions, for non-periodic functions Chebyshev series expansion is one of the alternatives that can be used. They are accepted as cosine Fourier series, for this reason FFT can also be used for Chebyshev series. Apart from this similarity, Chebyshev series are exempt from the non-uniformity at the boundaries.

### 3.3.1. Chebyshev Polynomials

$T_k(x)$ is the Chebyshev polynomial of first kind of degree k and it is defined at $x \in [-1,1]$. It can also be formulated as follows:

$$T_k(x) = cos(k\, arccos(x)), \; k \in \mathrm{N} \tag{3.20}$$

since the above equation is a cosine function then $T_k(x)$ can be defined in $[-1,1]$. By introducing $x = cos\, z$ into Eq. (3.20), the following relation can be obtained:

$$T_k(x) = cos\, kz \tag{3.21}$$

Chebyshev polynomials are orthogonal with respect to the weight function of,

$$w(x) = \frac{1}{\sqrt{(1-x^2)}}, \; \mathrm{x} \in [\text{-}1,1] \tag{3.22}$$

and by using the scalar product defined by Eq. (3.2) the orthogonality property of Chebyshev polynomials can be written as follows:

$$(T_k, T_l)_w = \int_{-1}^{1} T_k(x) T_l(x)\, w dx = \frac{\pi}{2} b_k \delta_{k,l} \tag{3.23}$$

where $\delta_{k,l}$ is the Kronecker delta and one can define $b_k$ as

$$b_k = \begin{cases} 2 & \text{if } k = 0, \\ 1 & \text{if } k \geq 1. \end{cases} \tag{3.24}$$

### 3.3.2. Calculation of Chebyshev coefficients

Chebyshev approximation of the function $f(x)$ can be written in series expansion form:

$$f_N(x)=\sum_{k=0}^{N}\hat{f}_k T_k(x),\quad \mathrm{x}\in[\text{-}1,1] \tag{3.25}$$

Similarly, as described in Fourier series section, expansion coefficients $\hat{f}_k$ can be determined by using the Galerkin-type technique. The residual function again is vanished in the average sense and the final form of the scalar product can be written by following the same procedure as in Section 3.2.1.

$$\int_{-1}^{1}\left(fT_l w-\sum_{k=0}^{N}\hat{f}_k T_k T_l w\right)dx=0,\ l=0,\ldots,N \tag{3.26}$$

By utilizing Eq. (3.23), $\hat{f}_k$ can be found easily as follows:

$$\hat{f}_k=\frac{2}{\pi b_k}\int_{-1}^{1} fT_k w dx \tag{3.27}$$

### 3.3.3. Discrete Chebyshev series and Collocation Method

In this section, discrete Chebyshev expansion coefficients will be calculated by the aid of the collocation technique, i.e. residual function vanishes at collocation points that are mentioned in Section 3.2.2. Collocation points considered here are the Gauss-Lobatto points defined as:

$$x_i=cos\frac{\pi i}{N},\ i=0,\ldots,N. \tag{3.28}$$

According to the collocation technique let

$$f(x_i)=f_N(x_i)=\sum_{k=0}^{N}\hat{f}_k T_k(x_i),\ i=0,\ldots,N \tag{3.29}$$

Eq. (3.29) can be rephrased by introducing Eq. (3.20) into Eq. (3.29):

$$f\left(x_i\right)=f_N\left(x_i\right)=\sum_{k=0}^{N}\hat{f}_k\,cos\frac{k\pi i}{N},\;\; i=0,\ldots,N \tag{3.30}$$

At this point, the discrete orthogonality relation based on Gauss-Lobatto points should be described. By referring to [27], the following quadrature formula applied to any function $p\left(x\right)$ is used to determine orthogonality relation:

$$\int_{-1}^{1}p\left(x\right)w\left(x\right)dx\cong\frac{\pi}{N}\sum_{i=0}^{N}\frac{p\left(x_i\right)}{\overline{c}_i} \tag{3.31}$$

where

$$\overline{c}_k=\begin{cases}2 & \text{if}\;\; k=0,\\ 1 & \text{if}\;\; 1\le k\le N-1,\\ 2 & \text{if}\;\; k=N.\end{cases} \tag{3.32}$$

By taking Eqs. (3.23) and (3.31) into consideration simultaneously, the discrete orthogonality relation can be found as follows:

$$\sum_{i=0}^{N}\frac{1}{\overline{c}_i}T_k\left(x_i\right)T_l\left(x_i\right)=\frac{\overline{c}_k}{2}N\delta_{k,l} \tag{3.33}$$

where $0\le k,l\le N$.

Now, by the aid of the above equation and Eq. (3.29), expansion coefficients can be obtained. By multiplying each side of Eq. (3.29) by $T_l\left(x_i\right)/\overline{c}_i$, and taking the summation from $i=0$ to $i=N$, and using Eq. (3.33), the following relations are obtained:

$$\hat{f}_k=\frac{2}{\overline{c}_kN}\sum_{i=0}^{N}\frac{1}{\overline{c}_i}f_iT_k\left(x_i\right),\;\; k=0,\ldots,N, \tag{3.34}$$

or

$$\hat{f}_k=\frac{2}{\overline{c}_kN}\sum_{i=0}^{N}\frac{1}{\overline{c}_i}f_i\,cos\frac{k\pi i}{N},\;\; k=0,\ldots,N \tag{3.35}$$

where $f_i=f\left(x_i\right)=f_N\left(x_i\right)$.

Eqs. (3.30) and (3.35) readily show that both the expansion coefficients and the approximated function are written in the form of discrete Fourier series in cosine. For this reason, FFT algorithm is also used in Chebyshev series to provide the connection between the physical space and the spectral space. Finally, the recurrence relation is given about the Chebyshev integration that is used in Chapter 4. If ${a_n}^{(q)}$ denotes the Chebyshev coefficients of the $q$-th derivative of $f\left(x\right)$, then

$$c_{n-1}{a_{n-1}}^{(q)}-{a_{n+1}}^{(q)}=2n\ {a_n}^{(q-1)} \tag{3.36}$$

where $c_0=2$ and $c_n=1$ for $n\geq 1$ [28].

## 3.4. Description of Temporal Discretization Techniques

In this section, discretization of a variable with respect to time will be discussed. For this purpose, two techniques are used in this study, and both of them are two-step schemes, i.e. variables in three successive time levels are used to discretize. The former technique is Semi-implicit Adams-Bashforth / Crank-Nicolson (AB/CN) scheme, the latter one is Semi-implicit Adams-Bashforth /Backward-Differentiation (AB/BDI2) scheme. The general formulations of those techniques are examined in order to give a comprehensible sight to the temporal discretization equations in Chapter 4. The formulations in this section all refer to [27]**.** As a reference point, one dimensional advection-diffusion equation is analyzed and application of both methods to this equation is shown. One dimensional advection-diffusion equation can be written as follows:

$$\frac{\partial g}{\partial t}+a\frac{\partial g}{\partial x}-v\frac{\partial^2 g}{\partial x^2}=f\left(x,t\right) \tag{3.37}$$

where $v$ is the coefficient of diffusion or viscosity term, and $a$ is the advective velocity term. Both of them are constant.

On the other hand, right hand side term $f\left(x,t\right)$ is the forcing term and changes spatially and temporally. $g\left(x,t\right)$ is the solution of the above equation and can be considered as the variables in Eq. (4.35) in Chapter 4. In the following section, general time discretization formulae of two-step schemes, the formulations of the AB/CN and AB/BDI2 schemes applied for Eq. (3.37) will be given.

### 3.4.1. Two-step methods

The general two-step scheme for Eq. (3.37) can be presented as follows:

$$\begin{aligned}&\frac{\left(1+\varepsilon\right)g^{n+1}-2\varepsilon g^{n}-\left(1-\varepsilon\right)g^{n-1}}{2\Delta t}\\&+a\partial_{x}\left[\gamma_{1}g^{n+1}+\gamma_{2}g^{n}+\left(1-\gamma_{1}-\gamma_{2}\right)g^{n-1}\right]\\&-v\partial_{xx}\left[\theta_{1}g^{n+1}+\theta_{2}g^{n}+\left(1-\theta_{1}-\theta_{2}\right)g^{n-1}\right]\\&=\theta_{1}f^{n+1}+\theta_{2}f^{n}+\left(1-\theta_{1}-\theta_{2}\right)f^{n-1}.\end{aligned} \tag{3.38}$$

The parameters $\varepsilon$ , $\gamma_1$ , $\gamma_2$ , $\theta_1$ and $\theta_2$ are arbitrary constants, according to the selected value of them, the type of the method is decided. By using the reference [27], second order accuracy of the above equation can be formulated as follows:

$$\frac{\varepsilon}{2}=2\gamma_{1}+\gamma_{2}-1=2\theta_{1}+\theta_{2}-1. \tag{3.39}$$

Both AB/CN and AB/BDI2 schemes have second order accuracy. Moreover, the above equation can be adapted to three dimensional cases also. In three dimensional case, besides first and second order derivatives with respect to x, $\partial_y,\partial_z$ and $\partial_{yy},\partial_{zz}$ terms are also taken into account.

The general form of the equation for three dimensional cases does not change and coefficients of first order and second order derivatives remain the same, too. In the following two sub-sections the aforementioned schemes that are used in this thesis are introduced.

#### 3.4.1.1. Semi-implicit AB/CN Scheme

This scheme is defined by taking:

$$\varepsilon = 1,\ \gamma_1 = 0,\ \gamma_2 = 3/2,\ \theta_1 = \theta_2 = 1/2\ . \tag{3.40}$$

By using these values and Eq. (3.38) simultaneously, the general form of this scheme is obtained as:

$$\frac{g^{n+1} - g^n}{\Delta t} + \frac{a}{2}\partial_x\left(3g^n - g^{n-1}\right) - \frac{\nu}{2}\partial_{xx}\left(g^{n+1} + g^n\right) = \frac{1}{2}\left(f^{n+1} + f^n\right) \tag{3.41}$$

#### 3.4.1.2. Semi-implicit AB/BDI2 Scheme

Similarly, this scheme is defined by taking:

$$\varepsilon = 2,\ \gamma_1 = 0,\ \gamma_2 = 2,\ \theta_1 = 1,\ \theta_2 = 0 \tag{3.42}$$

Again, by using these values and Eq. (3.38) simultaneously, the general form of this scheme is obtained:

$$\frac{3g^{n+1} - 4g^n + g^{n-1}}{2\Delta t} + a\partial_x\left(2g^n - g^{n-1}\right) - \nu\partial_{xx}g^{n+1} = f^{n+1}\ . \tag{3.43}$$

# CHAPTER 4

# SPECTRAL METHODS SOLUTION OF THE GOVERNING EQUATIONS

In this chapter, the formulation of the fluid motion and the solution method of the problem will be introduced. The governing equations that help us to understand the characteristics of the fluid motion are the Navier-Stokes equations: the continuity, momentum and energy equations. Those three equations are coupled, and for this reason they are solved simultaneously. The numerical method presented in this thesis was first represented by Kim, Moin and Moser [30] and developed by Zhang and Tangborn [31]. The details of the formulation and solution technique presented in this chapter are mostly the same as introduced in Tarı's thesis [32] with some differences, e.g. the inclination angle and some additional terms stemmed from the new temporal discretization technique.

## 4.1. Geometry, Domain and Assumptions

A channel between two inclined, infinitely long parallel walls is considered as the main geometry. The infinite walls are modeled as $L_x$ by $L_z$ walls with periodic boundary conditions at the boundaries in both streamwise and spanwise directions. The distance in the normal direction is $L_y$. In this problem, $L_y = 2$ and changes from $y = -1$ to $y = 1$.

Since there is a temperature difference between the plates, and also inclination angle from horizontal is given to the channel, buoyancy forces in the flow act in both normal and streamwise directions. The Boussinesq approximation is applied, and for this reason variations of all fluid properties other than the density are ignored, and the density variations only change the gravitational force. Moreover, flow is considered as incompressible. The geometry of the problem is given in Figure 1.1.

## 4.2. Formulation of Governing Equations

The Navier-Stokes equation, which will be described below, is written in the rotational form. Those equations for incompressible flow are:

$$\frac{\partial \mathbf{U}}{\partial t} + \omega \times \mathbf{U} = -\nabla p + \nu \nabla^2 \mathbf{U} + \beta \mathbf{g} T \tag{4.1}$$

$$\nabla \cdot \mathbf{U} = 0 \tag{4.2}$$

$$\frac{\partial T}{\partial t} + \mathbf{U} \cdot \nabla T = \alpha \nabla^2 T \tag{4.3}$$

where $\mathbf{U} = (u, \upsilon, w)$ is the velocity field at location $\mathbf{X} = (x, y, z)$ and time $t$, $p$ is pressure, and $\nu$, $\beta$ and $\alpha$ are the kinematic viscosity, the thermal expansion coefficient and the thermal diffusivity for the fluid, respectively. $T$ is the temperature of the fluid, $\mathbf{g} = (gsin\varphi, gcos\varphi)$ is the gravitational acceleration vector, and since there is an inclination from the horizontal, it is written in the vector form as shown above, $\varphi$ is the tilt angle measured from the horizontal axis and $\omega = \nabla \times \mathbf{U}$ is the vorticity.

The boundary conditions for the velocity field are:

$$\mathbf{U}(x,y,z,t)=0 \qquad \text{at} \qquad y=\pm 1 \qquad \textit{(No slip condition)}$$

$$\mathbf{U}(x+mL_x,y,z+nL_z,t)=\mathbf{U}(x,y,z,t) \qquad \textit{(Periodic condition)}$$

$$\frac{\partial u}{\partial x}=0 \qquad \text{at} \qquad y=\pm 1$$

$$\frac{\partial w}{\partial z}=0 \qquad \text{at} \qquad y=\pm 1$$

and, from the continuity equation, it is obtained that

$$\frac{\partial \upsilon}{\partial y}=0 \qquad \text{at} \qquad y=\pm 1$$

Also the boundary conditions for the temperature field are:

$$T(x+mL_x,y,z+nL_z,t)=T(x,y,z,t) \qquad \textit{(Periodic Condition)}$$

$$T(x,y,z,t)=T_1(x,z) \qquad \text{at} \qquad y=1$$

$$T(x,y,z,t)=T_2(x,z) \qquad \text{at} \qquad y=-1$$

In order to determine the non-dimensional form of Eqs. (4.1-3), $\bar{U}$ and $\bar{L}$ are used as the characteristic velocity and length scales of the problem, respectively. The channel height $H$ is usually used as the length scale. In this case, since Re is assumed to be very small due to the quiescent fluid, diffusion time scale as time scale and velocity scale is adjusted by taking $Re=1/Pr$. Temperature is non-dimensionalized by using the maximum temperature difference $\Delta T=T_{max}-T_{min}$. It is also defined that $\theta=T-T_m$, where $T_m$ is the mean temperature of the upper wall. Non-dimensional parameters are described by the superscript "*" and relations between the non-dimensional and the dimensional parameters can be shown as below:

$$\mathbf{U}^* = \frac{\mathbf{U}}{\bar{U}}$$

$$\mathbf{X}^* = \frac{\mathbf{X}}{\bar{X}}$$

$$t^* = \frac{\bar{U}}{\bar{X}} t$$

$$\theta^* = \frac{\theta}{\Delta T}$$

$$p^* = \frac{p}{\rho \bar{U}^2}$$

When these terms are put into the Eqs. (4.1-3), the equations take the form:

$$\frac{\partial \mathbf{U}^*}{\partial t} + \omega^* \times \mathbf{U}^* = -\nabla p^* + \frac{1}{Re} \nabla^2 \mathbf{U}^* + \frac{Ra}{Re^2\, Pr} \theta^* \tag{4.4}$$

$$\nabla \cdot \mathbf{U}^* = 0 \tag{4.5}$$

$$\frac{\partial \theta^*}{\partial t} + \mathbf{U}^* \cdot \nabla \theta^* = \frac{1}{Re\, Pr} \nabla^2 \theta^* \tag{4.6}$$

where

$$Ra = \frac{\bar{L}^3 \beta \mathbf{g} \Delta T}{\alpha \nu}$$

$$Re = \frac{\bar{L}\bar{U}}{\nu}$$

$$Pr = \frac{\nu}{\alpha}$$

In the rest of the chapter asterisks are dropped and every variable can be considered in non-dimensional form from now on. Moreover, “N-S” abbreviation is used to mention the set of governing equations such as Eqs. (4.4-6).

## 4.3. Solution of N-S by Using Spectral Methods

### 4.3.1. Reformulation of the Problem

The non-dimensional form of the governing equations obtained in the previous section can be reformulated in the form:

$$\frac{\partial u}{\partial t} = -\frac{\partial p}{\partial x} + h_1 + \frac{1}{Re}\nabla^2 u + \frac{Ra\, sin\,\varphi}{Re^2\, Pr}\theta \tag{4.7}$$

$$\frac{\partial \upsilon}{\partial t} = -\frac{\partial p}{\partial y} + h_2 + \frac{1}{Re}\nabla^2 \upsilon + \frac{Ra\, cos\,\varphi}{Re^2\, Pr}\theta \tag{4.8}$$

$$\frac{\partial w}{\partial t} = -\frac{\partial p}{\partial z} + h_3 + \frac{1}{Re}\nabla^2 w \tag{4.9}$$

$$\frac{\partial u}{\partial x} + \frac{\partial \upsilon}{\partial y} + \frac{\partial w}{\partial z} = 0 \tag{4.10}$$

$$\frac{\partial \theta}{\partial t} = -(u\frac{\partial \theta}{\partial x} + \upsilon\frac{\partial \theta}{\partial y} + w\frac{\partial \theta}{\partial z}) + \frac{1}{Re\, Pr}\nabla^2 \theta \tag{4.11}$$

The h terms that appear in Eqs. (4.7-11) result from the cross product of vorticity and the velocity vector which is in the left hand side of Equation 4.4. They can be introduced as follows:

$$h_1 = \upsilon\omega_z - w\omega_y \tag{4.12-a}$$

$$h_2 = w\omega_x - u\omega_z \tag{4.12-b}$$

$$h_3 = u\omega_y - \upsilon\omega_x \tag{4.12-c}$$

where $\omega_x, \omega_y, \omega_z$ are vorticity components in $x, y, z$ directions which are defined as:

$$\omega_x = \frac{\partial w}{\partial y} - \frac{\partial \upsilon}{\partial z} \tag{4.13-a}$$

$$\omega_y = \frac{\partial u}{\partial z} - \frac{\partial w}{\partial x} \tag{4.13-b}$$

$$\omega_z = \frac{\partial \upsilon}{\partial x} - \frac{\partial u}{\partial y} \tag{4.13-c}$$

In addition to those convective h terms, both pressure gradient and non-dimensional temperature terms can be brought together in the nonlinear terms as:

$$H_1 = h_1 - \frac{\partial p}{\partial x} + \frac{Ra sin\varphi}{Re^2\, Pr}\theta \tag{4.14-a}$$

$$H_2 = h_2 - \frac{\partial p}{\partial y} + \frac{Ra cos\varphi}{Re^2\, Pr}\theta \tag{4.14-b}$$

$$H_3 = h_3 - \frac{\partial p}{\partial z} \tag{4.14-c}$$

$$\mathbf{H} = (H_1, H_2, H_3) \tag{4.15}$$

Then the governing equation for the fluid velocity can be written as:

$$\frac{\partial \mathbf{U}}{\partial t} = \mathbf{H} + \frac{1}{Re}\nabla^2 \mathbf{U} \tag{4.16}$$

Taking the curl of the equation,

$$\frac{\partial}{\partial t}(\nabla \times \mathbf{U}) = \nabla \times \mathbf{H} + \frac{1}{Re}\nabla^2(\nabla \times \mathbf{U}) \tag{4.17}$$

yields

$$\frac{\partial}{\partial t}(\omega_x \mathbf{i} + \omega_y \mathbf{j} + \omega_z \mathbf{k}) = \nabla \times \mathbf{H} + \frac{1}{Re}\nabla^2(\omega_x \mathbf{i} + \omega_y \mathbf{j} + \omega_z \mathbf{k}) \tag{4.18}$$

where

$$\nabla \times \mathbf{H} = (\frac{\partial H_3}{\partial y} - \frac{\partial H_2}{\partial z})\mathbf{i} + (\frac{\partial H_1}{\partial z} - \frac{\partial H_3}{\partial x})\mathbf{j} + (\frac{\partial H_2}{\partial x} - \frac{\partial H_1}{\partial y})\mathbf{k} \tag{4.19}$$

Second order equation for the normal component of vorticity can be formed as:

$$\frac{\partial}{\partial t}G = h_g + \frac{1}{Re}\nabla^2 G \tag{4.20}$$

where

$$h_g = \frac{\partial H_1}{\partial z} - \frac{\partial H_3}{\partial x} \tag{4.21}$$

and

$$G = \omega_y \tag{4.22}$$

Now, the second derivative of the normal component of velocity in the governing equation is taken.

$$\frac{\partial \upsilon}{\partial t} = H_2 + \frac{1}{Re}\nabla^2 \upsilon \tag{4.23}$$

which yields a fourth order equation with respect to $\upsilon$

$$\frac{\partial}{\partial t}(\nabla^2 \upsilon) = h_\upsilon + \frac{1}{Re}\nabla^4 \upsilon \tag{4.24}$$

where

$$h_\upsilon = \nabla^2 H_2 \tag{4.25}$$

From the N-S equations and continuity the relation below can be determined.

$$\frac{\partial H_1}{\partial x} + \frac{\partial H_3}{\partial z} = -\frac{\partial H_2}{\partial y} \tag{4.26}$$

Therefore, the non-linear term $h_\upsilon$ can be written as

$$h_\upsilon = (\frac{\partial^2}{\partial x^2} + \frac{\partial^2}{\partial z^2})H_2 - \frac{\partial}{\partial y}(\frac{\partial H_1}{\partial x} + \frac{\partial H_3}{\partial z}) \tag{4.27}$$

The fourth order equation can be solved by dividing it into two second order equations by defining:

$$\nabla^2 \upsilon = \phi$$

The following set of equation is obtained:

$$\frac{\partial \phi}{\partial t} = h_\upsilon + \frac{1}{Re}\nabla^2 \phi \tag{4.28-a}$$

$$\nabla^2 \upsilon = \phi \tag{4.28-b}$$

$$\upsilon = 0 \qquad \text{at} \qquad y = \pm 1$$

$$\frac{\partial \upsilon}{\partial y} = 0 \qquad \text{at} \qquad y = \pm 1$$

In this coupled system the four boundary conditions are satisfied as follows. Let

$$\upsilon = \upsilon_p + c_1\upsilon_1 + c_2\upsilon_2$$

where the particular solution $\upsilon_p$ and two homogeneous solutions $\upsilon_1$ and $\upsilon_2$ satisfy the following equations.

$$\frac{\partial \phi_p}{\partial t} - \frac{1}{Re}\nabla^2\phi_p = h_\upsilon \tag{4.29}$$

$$\phi_p = 0 \qquad \text{at} \qquad y = \pm 1$$

$$\nabla^2\upsilon_p = \phi_p \tag{4.30}$$

$$\upsilon_p = 0 \qquad \text{at} \qquad y = \pm 1$$

$$\frac{\partial \phi_1}{\partial t} - \frac{1}{Re}\nabla^2\phi_1 = 0 \tag{4.31}$$

$$\phi_1 = 0 \qquad \text{at} \qquad y = 1$$

$$\phi_1 = 1 \qquad \text{at} \qquad y = -1$$

$$\nabla^2\upsilon_1 = \phi_1 \tag{4.32}$$

$$\upsilon_1 = 0 \qquad \text{at} \qquad y = \pm 1$$

$$\frac{\partial \phi_2}{\partial t} - \frac{1}{Re}\nabla^2\phi_2 = 0 \tag{4.33}$$

$$\phi_2 = 1 \qquad \text{at} \qquad y = 1$$

$$\phi_2 = 0 \qquad \text{at} \qquad y = -1$$

$$\nabla^2 \upsilon_2 = \phi_2 \tag{4.34}$$

$$\upsilon_2 = 0 \qquad \text{at} \qquad y = \pm 1$$

After the above equations are solved, the constants $c_1$ and $c_2$ are chosen to satisfy the boundary condition as below.

$$\frac{\partial \upsilon}{\partial y} = \frac{\partial \upsilon_p}{\partial y} + c_1 \frac{\partial \upsilon_1}{\partial y} + c_2 \frac{\partial \upsilon_2}{\partial y} = 0 \qquad \text{at} \qquad y = \pm 1$$

As a result, by means of the above equations and the boundary conditions, the problem has been reduced to the following set of equations:

$$\begin{gathered} \frac{\partial \phi}{\partial t} = h_\upsilon + \frac{1}{Re} \nabla^2 \phi \\ \nabla^2 \upsilon = \phi \\ \frac{\partial G}{\partial t} = h_g + \frac{1}{Re} \nabla^2 G \\ f + \frac{\partial \upsilon}{\partial y} = 0 \\ \frac{\partial \theta}{\partial t} = h_T + \frac{1}{Re\, Pr} \nabla^2 \theta \end{gathered} \tag{4.35}$$

where

$$f = \frac{\partial u}{\partial x} + \frac{\partial w}{\partial z}$$

$$G = \frac{\partial u}{\partial z} - \frac{\partial w}{\partial x}$$

$$h_g = \frac{\partial H_1}{\partial z} - \frac{\partial H_3}{\partial x} \tag{4.36}$$

$$h_\upsilon = -\frac{\partial}{\partial y}(\frac{\partial H_1}{\partial x} + \frac{\partial H_3}{\partial z}) + (\frac{\partial^2}{\partial x^2} + \frac{\partial^2}{\partial z^2})\mathrm{H}_2$$

$$h_T = -(u\frac{\partial \theta}{\partial x} + \upsilon\frac{\partial \theta}{\partial y} + w\frac{\partial \theta}{\partial z})$$

with corresponding boundary conditions:

$$\upsilon = 0 \quad \text{at} \quad y = \pm 1$$

$$\frac{\partial \upsilon}{\partial y} = 0 \quad \text{at} \quad y = \pm 1$$

$$G = 0 \quad \text{at} \quad y = \pm 1 \tag{4.37}$$

$$\theta = \theta_1 \quad \text{at} \quad y = 1$$

$$\theta = \theta_2 \quad \text{at} \quad y = -1$$

and periodic boundary conditions in $x$ and $z$ directions.

### 4.3.2. Series Expansion

In this section, velocity and temperature terms of non-dimensionalized rewritten set of equations are expanded in Fourier series in the streamwise and spanwise directions, and also the Chebyshev polynomials are used in the normal direction. Detailed information about these techniques is given in Chapter 3, and for this reason the main objective of this section is only to formulate N-S equations in terms of Fourier series and Chebyshev polynomials. Therefore, solutions have the form:

$$\mathbf{U} = \sum_{|j|<N_x} \sum_{|k|<N_z} \sum_{l=0}^{N_y} \hat{\tilde{u}}(j,k,l,t)\, exp[2\pi i(\frac{jx}{N_x} + \frac{kz}{N_z})]T_l(y)$$

$$\theta = \sum_{|j|<N_x} \sum_{|k|<N_z} \sum_{l=0}^{N_y} \hat{\tilde{\theta}}(j,k,l,t)\, exp[2\pi i(\frac{jx}{N_x} + \frac{kz}{N_z})]T_l(y)$$

where $T_l(y) = cos(l \ arccos\, y)$ is the Chebyshev polynomial of degree $l$ and $N_x$, $N_y$ and $N_z$ are the number of intervals in spatial discretization. The symbols $\sim$ and $\wedge$ are used to denote the variables in Fourier and Chebyshev space, respectively.

### 4.3.3. Temporal Discretization

Discretization for time is done by using two methods. Both of them are two-step (i.e. three time level) and semi-implicit methods. Those are Adams-Bashforth/Crank-Nicolson (AB/CN) scheme and Adams-Bashforth/Backward-Differentiation (AB/BDI2) scheme. Details of formulation of these schemes are given in Chapter 3, and in this section application of them in the N-S equations will be given in the ultimate form.

#### 4.3.3.1. Semi-implicit AB/CN Scheme

By using this scheme, the $\theta$ equation in Eq. (4.35) becomes,

$$\frac{\theta^{n+1}-\theta^{n}}{\Delta t}=\frac{3}{2}h_T{}^{n}-\frac{1}{2}h_T{}^{n-1}+\frac{1}{Re\,Pr}\left(\frac{\nabla^2\theta^{n+1}+\nabla^2\theta^{n}}{2}\right) \tag{4.38}$$

which can be also written as:

$$\nabla^2\theta^{n+1}-\frac{2\,Re\,Pr}{\Delta t}\theta^{n+1}=-3\,Re\,Pr\,h_T{}^{n}+Re\,Pr\,h_T{}^{n-1}-\nabla^2\theta^{n}-\frac{2\,Re\,Pr}{\Delta t}\theta^{n}$$

$$\theta=\theta_1 \quad \text{at} \quad y=1$$
$$\theta=\theta_2 \quad \text{at} \quad y=-1$$

Similarly, the $G$ equation takes the form as in below:

$$\frac{G^{n+1}-G^{n}}{\Delta t}=\frac{3}{2}h_g{}^{n}-\frac{1}{2}h_g{}^{n-1}+\frac{1}{Re}\left(\frac{\nabla^2G^{n+1}+\nabla^2G^{n}}{2}\right) \tag{4.39}$$

$$\nabla^2G^{n+1}-\frac{2\,Re}{\Delta t}G^{n+1}=-3\,Re\,h_g{}^{n}+Re\,h_g{}^{n-1}-\nabla^2G^{n}-\frac{2\,Re}{\Delta t}G^{n}$$

$$G=0 \quad \text{at} \quad y=\pm 1$$

and equation of $\upsilon$ becomes

$$\nabla^2\phi_p{}^{n+1}-\frac{2\,Re}{\Delta t}\phi_p{}^{n+1}=-3\,Re\,h_\upsilon{}^{n}+Re\,h_\upsilon{}^{n-1}-\nabla^2\phi_p{}^{n}-\frac{2\,Re}{\Delta t}\phi_p{}^{n} \tag{4.40}$$

$$\phi_p=0 \quad \text{at} \quad y=\pm 1$$

$$\nabla^2\upsilon_p{}^{n+1}=\phi_p{}^{n+1} \tag{4.41}$$

$$\upsilon_p=0 \quad \text{at} \quad y=\pm 1$$

$$\nabla^2 \phi_1^{n+1} - \frac{2\,Re}{\Delta t} \phi_1^{n+1} = 0 \tag{4.42}$$

$$\phi_1 = 0 \quad \text{at} \quad y = 1$$

$$\phi_1 = 1 \quad \text{at} \quad y = -1$$

$$\nabla^2 \upsilon_1^{n+1} = \phi_1^{n+1} \tag{4.43}$$

$$\upsilon_1 = 0 \quad \text{at} \quad y = \pm 1$$

$$\nabla^2 \phi_2^{n+1} - \frac{2\,Re}{\Delta t} \phi_2^{n+1} = 0 \tag{4.44}$$

$$\phi_2 = 1 \quad \text{at} \quad y = 1$$

$$\phi_2 = 0 \quad \text{at} \quad y = -1$$

$$\nabla^2 \upsilon_2^{n+1} = \phi_2^{n+1} \tag{4.45}$$

$$\upsilon_2 = 0 \quad \text{at} \quad y = \pm 1$$

#### 4.3.3.2. Semi-implicit AB/BDI2 Scheme

By using this scheme, the $\theta$ equation in Eq.(4.35) becomes,

$$\frac{3\theta^{n+1} - 4\theta^n + \theta^{n-1}}{2\Delta t} = 2h_T{}^n - h_T{}^{n-1} + \frac{1}{Re\,Pr} \nabla^2 \theta^{n+1} \tag{4.46}$$

which can be also written as:

$$\nabla^2 \theta^{n+1} - \frac{3\,Re\,Pr}{2\Delta t} \theta^{n+1} = -2\,Re\,Pr\,h_T{}^n + Re\,Pr\,h_T{}^{n-1} - \frac{Re\,Pr}{\Delta t}(2\theta^n - \frac{\theta^{n-1}}{2})$$

$$\theta = \theta_1 \quad \text{at} \quad y = 1$$

$$\theta = \theta_2 \quad \text{at} \quad y = -1$$

Similarly, the $G$ equation takes the form as in below:

$$\frac{3G^{n+1}-4G^{n}+G^{n-1}}{2\Delta t}=2h_{g}{}^{n}-h_{g}{}^{n-1}+\frac{1}{Re}\nabla^{2}G^{\mathrm{n+1}} \tag{4.47}$$

$$\nabla^{2}G^{n+1}-\frac{3\,Re}{2\Delta t}G^{n+1}=-2\,Re\,h_{g}{}^{n}+Re\,h_{g}{}^{n-1}-\frac{Re}{\Delta t}(2\mathrm{G}^{n}-\frac{G^{n-1}}{2})$$

$$G=0 \qquad \text{at} \qquad y=\pm 1$$

and equation of $\upsilon$ becomes

$$\nabla^{2}\phi_{p}{}^{n+1}-\frac{3\,Re}{2\Delta t}\phi_{p}{}^{n+1}=-2\,Re\,h_{\upsilon}{}^{n}+Re\,h_{\upsilon}{}^{n-1}-\frac{Re}{\Delta t}(2\phi_{p}{}^{n}-\frac{\phi_{p}{}^{n-1}}{2}) \tag{4.48}$$

$$\phi_{p}=0 \qquad \text{at} \qquad y=\pm 1$$

$$\nabla^{2}\upsilon_{p}{}^{n+1}=\phi_{p}{}^{n+1} \tag{4.49}$$

$$\upsilon_{p}=0 \qquad \text{at} \qquad y=\pm 1$$

$$\nabla^{2}\phi_{1}{}^{n+1}-\frac{3\,Re}{2\Delta t}\phi_{1}{}^{n+1}=0 \tag{4.50}$$

$$\phi_{1}=0 \qquad \text{at} \qquad y=1$$

$$\phi_{1}=1 \qquad \text{at} \qquad y=-1$$

$$\nabla^{2}\upsilon_{1}{}^{n+1}=\phi_{1}{}^{n+1} \tag{4.51}$$

$$\upsilon_{1}=0 \qquad \text{at} \qquad y=\pm 1$$

$$\nabla^{2}\phi_{2}{}^{n+1}-\frac{3\,Re}{2\Delta t}\phi_{2}{}^{n+1}=0 \tag{4.52}$$

$$\phi_{2}=1 \qquad \text{at} \qquad y=1$$

$$\phi_{2}=0 \qquad \text{at} \qquad y=-1$$

$$\nabla^{2}\upsilon_{2}{}^{n+1}=\phi_{2}{}^{n+1} \tag{4.53}$$

$$\upsilon_{2}=0 \qquad \text{at} \qquad y=\pm 1$$

### 4.3.4. Spatial Discretization

The expansions in x and z directions are Fourier series and that in y direction is Chebyshev polynomial expansion. The grid points in x and z directions are defined as

$$x_i = \frac{iL_x}{N_x}, \quad i = 0,1,\ldots,N_x - 1$$
$$z_k = \frac{kL_z}{N_z}, \quad k = 0,1,\ldots,N_z - 1$$

The grid points in y direction are defined as Chebyshev-Gauss-Lobatto points:

$$y_j = cos\frac{\pi j}{N_y}, \quad \mathrm{j} = 0,1,\ldots,N_y$$

The system is solved in Fourier-Chebyshev space. It is denoted that Fourier coefficients of $\theta$ as $\tilde{\theta}$ and the Chebyshev coefficients as $\hat{\theta}$. Also, $D^2$ is used for the second derivative with respect to y. Since two methods for temporal discretization are used as shown in the previous section, equations are written for both methods separately.

#### 4.3.4.1. Semi-implicit AB/CN Scheme

Equation of time discretized $\theta$ in Fourier-Chebyshev space becomes

$$D^2\hat{\tilde{\theta}}^{n+1} - (\alpha_1^{\ 2} + \alpha_2^{\ 2})\hat{\tilde{\theta}}^{n+1} - \frac{2\,Re\,Pr}{\Delta t}\hat{\tilde{\theta}}^{n+1} = RHS_T^{\ n,n-1} \tag{4.54}$$

where

$$RHS_T = -3\,Re\,Pr\,\hat{\tilde{h}}_T^{\ n} + Re\,Pr\,\hat{\tilde{h}}_T^{\ n-1} - D^2\hat{\tilde{\theta}}^n + (\alpha_1^{\ 2} + \alpha_2^{\ 2})\hat{\tilde{\theta}}^n - \frac{2\,Re\,Pr}{\Delta t}\hat{\tilde{\theta}}^n$$

and the boundary conditions are

$$\hat{\tilde{\theta}} = \hat{\tilde{\theta}}_1 \quad \text{at} \quad y = 1$$
$$\hat{\tilde{\theta}} = \hat{\tilde{\theta}}_2 \quad \text{at} \quad y = -1$$

Here $\alpha_1$ and $\alpha_2$ are denoted as wavenumbers in x and z directions, respectively. It is also defined that

$$\kappa^2 = \alpha_1{}^2 + \alpha_2{}^2$$

and Eq. (4.54) is rewritten as

$$D^2\hat{\tilde{\theta}}^{n+1} - (\kappa^2 + \frac{2\,Re\,Pr}{\Delta t})\hat{\tilde{\theta}}^{n+1} = RHS_T{}^{n,n-1} \qquad (4.55)$$

which is a second order differential equation in Fourier-Chebyshev space and has to be solved with respect to each $\alpha_1$ and $\alpha_2$.

By using the same methodology, time discretized $G$ and $\upsilon$ equations can be rewritten as follows:

$$D^2\hat{\tilde{G}}^{n+1} - (\kappa^2 + \frac{2\,Re}{\Delta t})\hat{\tilde{G}}^{n+1} = RHS_g{}^{n,n-1} \qquad (4.56)$$

$$\hat{\tilde{G}} = 0 \qquad \text{at} \qquad y = \pm 1$$

$$RHS_g = -3\,Re\,\hat{\tilde{h}}_g{}^n + Re\,\hat{\tilde{h}}_g{}^{n-1} - D^2\hat{\tilde{G}}^n + (\alpha_1{}^2 + \alpha_2{}^2)\hat{\tilde{G}}^n - \frac{2\,Re}{\Delta t}\hat{\tilde{G}}^n$$

$$D^2\hat{\tilde{\phi}}_p{}^{n+1} - (\kappa^2 + \frac{2\,Re}{\Delta t})\hat{\tilde{\phi}}_{\mathrm{p}}{}^{n+1} = RHS_\upsilon{}^{n,n-1} \qquad (4.57)$$

$$\hat{\tilde{\phi}}_p = 0 \qquad \text{at} \qquad y = \pm 1$$

$$RHS_\upsilon = -3\,Re\,\hat{\tilde{h}}_\upsilon{}^n + Re\,\hat{\tilde{h}}_\upsilon{}^{n-1} - D^2\hat{\tilde{\phi}}_p{}^n + (\alpha_1{}^2 + \alpha_2{}^2)\hat{\tilde{\phi}}_p{}^n - \frac{2\,Re}{\Delta t}\hat{\tilde{\phi}}_p{}^n$$

$$D^2\hat{\tilde{\upsilon}}_p{}^{n+1} - \kappa^2\hat{\tilde{\upsilon}}_p{}^{n+1} = \hat{\tilde{\phi}}_p{}^{n+1} \qquad (4.58)$$

$$\hat{\tilde{\upsilon}}_p = 0 \qquad \text{at} \qquad y = \pm 1$$

$$D^2\hat{\tilde{\phi}}_1^{\,n+1} - (\kappa^2 + \frac{2\,Re}{\Delta t})\hat{\tilde{\phi}}_1^{\,n+1} = 0 \tag{4.59}$$

$$\hat{\tilde{\phi}}_1 = 0 \quad \text{at} \quad y = 1$$

$$\hat{\tilde{\phi}}_1 = 1 \quad \text{at} \quad y = -1$$

$$D^2\hat{\tilde{\upsilon}}_1^{\,n+1} - \kappa^2\hat{\tilde{\upsilon}}_1^{\,n+1} = \hat{\tilde{\phi}}_1^{\,n+1} \tag{4.60}$$

$$\hat{\tilde{\upsilon}}_1^{\,n+1} = 0 \quad \text{at} \quad y = \pm 1$$

$$D^2\hat{\tilde{\phi}}_2^{\,n+1} - (\kappa^2 + \frac{2\,Re}{\Delta t})\hat{\tilde{\phi}}_2^{\,n+1} = 0 \tag{4.61}$$

$$\hat{\tilde{\phi}}_2 = 1 \quad \text{at} \quad y = 1$$

$$\hat{\tilde{\phi}}_2 = 0 \quad \text{at} \quad y = -1$$

$$D^2\hat{\tilde{\upsilon}}_2^{\,n+1} - \kappa^2\hat{\tilde{\upsilon}}_2^{\,n+1} = \hat{\tilde{\phi}}_2^{\,n+1} \tag{4.62}$$

$$\hat{\tilde{\upsilon}}_2^{\,n+1} = 0 \quad \text{at} \quad y = \pm 1$$

#### 4.3.4.2. Semi-implicit AB/BDI2 Scheme

By using same procedure as in the previous section, all equations of time discretized with AB/BDI2 scheme can be rewritten as follows:

$$D^2\hat{\tilde{\theta}}^{n+1} - (\kappa^2 + \frac{3\,Re\,Pr}{2\Delta t})\hat{\tilde{\theta}}^{n+1} = RHS_T^{\;n,n-1} \tag{4.63}$$

where

$$RHS_T = -2\,Re\,Pr\,\hat{\tilde{h}}_T^{\,n} + Re\,Pr\,\hat{\tilde{h}}_T^{\,n-1} - \frac{Re\,Pr}{\Delta t}(2\hat{\tilde{\theta}}^n - \frac{\hat{\tilde{\theta}}^{n-1}}{2})$$

$$\hat{\hat{\theta}} = \hat{\hat{\theta}}_1 \qquad \text{at} \qquad y = 1$$

$$\hat{\hat{\theta}} = \hat{\hat{\theta}}_2 \qquad \text{at} \qquad y = -1$$

$$D^2\hat{\hat{G}}^{n+1} - (\kappa^2 + \frac{3\,Re}{2\Delta t})\hat{\hat{G}}^{n+1} = RHS_g{}^{n,n-1} \tag{4.64}$$

$$\hat{\hat{G}} = 0 \qquad \text{at} \qquad y = \pm 1$$

$$RHS_g = -2\,Re\,\hat{\hat{h}}_g{}^{n} + Re\,\hat{\hat{h}}_g{}^{n-1} - \frac{Re}{\Delta t}(2\hat{\hat{G}}^{n} - \frac{\hat{\hat{G}}^{n-1}}{2})$$

$$D^2\hat{\hat{\phi}}_p{}^{n+1} - (\kappa^2 + \frac{3\,Re}{2\Delta t})\hat{\hat{\phi}}_{\mathrm{p}}{}^{n+1} = RHS_\upsilon{}^{n,n-1} \tag{4.65}$$

$$\hat{\hat{\phi}}_p = 0 \qquad \text{at} \qquad y = \pm 1$$

$$RHS_\upsilon = -2\,Re\,\hat{\hat{h}}_\upsilon{}^{n} + Re\,\hat{\hat{h}}_\upsilon{}^{n-1} - \frac{Re}{\Delta t}(2\hat{\hat{\phi}}_p{}^{n} - \frac{\hat{\hat{\phi}}_p{}^{n-1}}{2})$$

$$D^2\hat{\hat{\upsilon}}_p{}^{n+1} - \kappa^2\hat{\hat{\upsilon}}_p{}^{n+1} = \hat{\hat{\phi}}_p{}^{n+1} \tag{4.66}$$

$$\hat{\hat{\upsilon}}_p{}^{n+1} = 0 \qquad \text{at} \qquad y = \pm 1$$

$$D^2\hat{\hat{\phi}}_1{}^{n+1} - (\kappa^2 + \frac{3\,Re}{2\Delta t})\hat{\hat{\phi}}_1{}^{n+1} = 0 \tag{4.67}$$

$$\hat{\hat{\phi}}_1 = 0 \qquad \text{at} \qquad y = 1$$

$$\hat{\hat{\phi}}_1 = 1 \qquad \text{at} \qquad y = -1$$

$$D^2 \hat{\tilde{\upsilon}}_1^{\,n+1} - \kappa^2 \hat{\tilde{\upsilon}}_1^{\,n+1} = \hat{\tilde{\phi}}_1^{\,n+1} \tag{4.68}$$

$$\hat{\tilde{\upsilon}}_1^{\,n+1} = 0 \qquad \text{at} \qquad y = \pm 1$$

$$D^2 \hat{\tilde{\phi}}_2^{\,n+1} - (\kappa^2 + \frac{3\,Re}{2\Delta t})\hat{\tilde{\phi}}_2^{\,n+1} = 0 \tag{4.69}$$

$$\hat{\tilde{\phi}}_2 = 1 \qquad \text{at} \qquad y = 1$$

$$\hat{\tilde{\phi}}_2 = 0 \qquad \text{at} \qquad y = -1$$

$$D^2 \hat{\tilde{\upsilon}}_2^{\,n+1} - \kappa^2 \hat{\tilde{\upsilon}}_2^{\,n+1} = \hat{\tilde{\phi}}_2^{\,n+1} \tag{4.70}$$

$$\hat{\tilde{\upsilon}}_2^{\,n+1} = 0 \qquad \text{at} \qquad y = \pm 1$$

Real FFT (Fast Fourier Transform) is used to transform Fourier-Chebyshev space into physical space. The transforms related to Chebyshev space can also use FFT because of the Gauss-Lobatto points chosen in y direction, which make the discrete Chebyshev expansion become a simple cosine series.

Since all the functions are real and a cosine transform for Chebyshev transform is desired, complex FFT would increase the time cost of this study. For this reason, real FFT is used. The complex coefficients of a function in Fourier space are split into two real sets of data and calculated separately.

### 4.3.5. Spectral Integration of N-S

In the aforementioned sections, second order differential equations in Fourier-Chebyshev space are finally derived. In this section, those equations will be written in general form, and how the integration of them by using spectral method was made will be explained. They can be thought as a second order differential with two boundary conditions in y direction as follows:

$$\begin{aligned} &\tau'' - \delta\tau = f(y) \text{ where } y \in [-1,1] \\ &\tau = \tau_1 \text{ at } y = -1 \\ &\tau = \tau_2 \text{ at } y = 1 \end{aligned} \tag{4.71}$$

By the aid of the Chebyshev-Tau method, solution such as in the below is anticipated.

$$\tau_{N_y}(y) = \sum_{j=0}^{N_y} a_j T_j(y)$$

with corresponding boundary conditions

$$\sum_{j=0}^{N_y} (-1)^j a_j = \tau_1 \tag{4.72}$$

$$\sum_{j=0}^{N_y} a_j = \tau_2 \tag{4.73}$$

where $T_j(y)$ is the Chebyshev polynomial of degree $j$. This system is usually solved directly for $\tau$ by constructing a spectral differentiation matrix, using the recurrence relations of Chebyshev differentiation.

Integral equation is constructed in order to solve $\tau''$ instead of solving $\tau$ itself. This approach was investigated by Greengard [33] and proven to be more accurate than the spectral differentiation method as the number of points increases.

Let

$$\tau'' = \sigma(y)$$

$\sigma(y)$ and $f(y)$ can be written in series form of Chebyshev polynomials, thus it is obtained as follows:

$$\sigma(y) = \sum_{j=0}^{N_y} b_j T_j(y)$$

$$f(y) = \sum_{j=0}^{N_y} f_j T_j(y)$$

By introducing these terms into Eq. (4.71),

$$\sigma(y) - \left[ \delta \int_{-1}^{y} \int_{-1}^{t} \sigma(\tau) d\tau dt + \delta C_1 y + \delta C_0 \right] = f(\mathrm{y}) \qquad (4.74)$$

where

$$\sum_{j=2}^{N_y} a_j T_j(y) = \int_{-1}^{y} \int_{-1}^{t} \sigma(\tau) d\tau dt$$

$$a_0 T_0(y) = C_0$$

$$a_1 T_1(y) = C_1 y$$

In these relations $\left\{a_j\right\}$ is defined as the coefficients of series expansions of $\tau$ ,$\left\{b_j\right\}$ as the coefficients representing $\tau''$, $\left\{d_j\right\}$ as the coefficients defining $\tau'$ and $\left\{c_j\right\}$ are the constants defined as $c_0 = 2$ ,$c_j = 1$ for $j > 0$, $c_j = 0$ for $j > N_y$. By using the relation (3.36), following equations can be written.

The recurrence relation of the Chebyshev first integration is

$$d_j = \frac{1}{2j}\left(c_{j-1}b_{j-1} - c_{j+1}b_{j+1}\right) \tag{4.75}$$

Using the same relation, the second integration becomes

$$a_j = \frac{1}{2j}\left(c_{j-1}d_{j-1} - c_{j+1}d_{j+1}\right) \tag{4.76}$$

By substituting Eq. (4.75) into Eq. (4.76), the following relation between $a_j$ and $b_j$ can be obtained:

$$a_j = \frac{1}{2j}\left[\frac{c_{j-1}}{2(j-1)}\left(c_{j-2}b_{j-2} - c_j b_j\right) - \frac{c_{j+1}}{2(j+1)}\left(c_j b_j - c_{j+2}b_{j+2}\right)\right] \tag{4.77}$$

When the above relation is introduced into Eq. (4.74), it yields

$$b_j - \frac{\delta}{2j}\left[\frac{c_{j-1}c_{j-2}}{2(j-1)}b_{j-2} - \frac{c_j}{2}\left(\frac{c_{j-1}}{j-1} + \frac{c_{j+1}}{j+1}\right)b_j + \frac{c_{j+1}c_{j+2}}{2(j+1)}b_{j+2}\right] = f_j \tag{4.78}$$

which can be rewritten as

$$-\delta\frac{c_{j-1}c_{j-2}}{4j(j-1)}b_{j-2} + \left[1 + \frac{\delta c_j}{4j}\left(\frac{c_{j-1}}{j-1} + \frac{c_{j+1}}{j+1}\right)\right]b_j - \delta\frac{c_{j+1}c_{j+2}}{4j(j+1)}b_{j+2} = f_j$$

$$j = 2,3,\ldots,N_y$$

Finally, coefficients are assigned to some variables and general form of the matrix for the equations is obtained.

$$p_j = -\delta\frac{c_{j-1}c_{j-2}}{4j(j-1)} \tag{4.79}$$

$$q_j = 1 + \frac{\delta c_j}{4j}\left(\frac{c_{j-1}}{j-1} + \frac{c_{j+1}}{j+1}\right) \tag{4.80}$$

$$r_j = -\delta\frac{c_{j+1}c_{j+2}}{4j(j+1)} \tag{4.81}$$

$$p_j b_{j-2} + q_j b_j + r_j b_{j+2} = f_j,\ j = 2,3,\ldots,N_y \tag{4.82}$$

Boundary conditions defined by Eqs. (4.72) and (4.73) can be rewritten by using the relations in Eq. (4.74) as follows:

$$\sum_{j=2}^{N_y}(-1)^j a_j - C_1 + C_0 = \tau_1 \quad \text{at } y=-1 \tag{4.83}$$

$$\sum_{j=2}^{N_y} a_j + C_1 + C_0 = \tau_2 \quad \text{at } y=1 \tag{4.84}$$

which can be reformed as

$$C_0 + \sum_{j=2}^{N_y} a_j = \frac{\tau_1+\tau_2}{2} \qquad \text{(Even)}$$

$$C_1 + \sum_{j=2}^{N_y-1} a_j = \frac{\tau_2-\tau_1}{2} \qquad \text{(Odd)}$$

By using the Eq. (4.77), $a_j$ in the boundary conditions above is replaced with $b_j$, and it yields

$$C_0 + \sum_{j=2}^{N_y}\frac{1}{2j}\left[\frac{c_{j-1}}{2(j-1)}\left(c_{j-2}b_{j-2}-c_jb_j\right)-\frac{c_{j+1}}{2(j+1)}\left(c_jb_j-c_{j+2}b_{j+2}\right)\right]=\frac{\tau_1+\tau_2}{2}$$

$$C_1 + \sum_{j=2}^{N_y-1}\frac{1}{2j}\left[\frac{c_{j-1}}{2(j-1)}\left(c_{j-2}b_{j-2}-c_jb_j\right)-\frac{c_{j+1}}{2(j+1)}\left(c_jb_j-c_{j+2}b_{j+2}\right)\right]=\frac{\tau_2-\tau_1}{2}$$

These two additional equations from boundary conditions form the top rows in the matrices and $\{t_j\}$ is used for the coefficients of $\{b_j\}$. The problem is split into two matrix systems: even and odd.

The even system is:

$$\begin{bmatrix} 1 & t_0 & t_2 & t_4 & \cdots & \cdots & t_{N_y} \\ p_0 & q_0 & r_0 & 0 & \cdots & \cdots & 0 \\ 0 & p_2 & q_2 & r_2 & 0 & \cdots & 0 \\ \vdots & 0 & \ddots & \ddots & \ddots & 0 & \vdots \\ \vdots & \vdots & 0 & \ddots & \ddots & \ddots & \vdots \\ \vdots & \vdots & \vdots & 0 & p_{N_y-2} & q_{N_y-2} & r_{N_y-2} \\ 0 & \cdots & \cdots & \cdots & 0 & p_{N_y} & q_{N_y} \end{bmatrix} \begin{bmatrix} C_0 \\ b_0 \\ b_2 \\ \vdots \\ b_j \\ \vdots \\ b_{N_y} \end{bmatrix} = \begin{bmatrix} (\tau_1+\tau_2)/2 \\ f_0 \\ f_2 \\ \vdots \\ \vdots \\ f_j \\ \vdots \\ f_{N_y} \end{bmatrix} \tag{4.85}$$

$$j = 0,2,4,\ldots,N_y$$

The odd system is:

$$\begin{bmatrix} 1 & t_1 & t_3 & t_5 & \cdots & \cdots & t_{N_y-1} \\ p_1 & q_1 & r_1 & 0 & \cdots & \cdots & 0 \\ 0 & p_3 & q_3 & r_3 & 0 & \cdots & 0 \\ \vdots & 0 & \ddots & \ddots & \ddots & 0 & \vdots \\ \vdots & \vdots & 0 & \ddots & \ddots & \ddots & \vdots \\ \vdots & \vdots & \vdots & 0 & p_{N_y-3} & q_{N_y-3} & r_{N_y-3} \\ 0 & \cdots & \cdots & \cdots & 0 & p_{N_y-1} & q_{N_y-1} \end{bmatrix} \begin{bmatrix} C_1 \\ b_1 \\ b_3 \\ \vdots \\ b_j \\ \vdots \\ b_{N_y-1} \end{bmatrix} = \begin{bmatrix} (\tau_2-\tau_1)/2 \\ f_1 \\ f_3 \\ \vdots \\ \vdots \\ f_j \\ \vdots \\ f_{N_y-1} \end{bmatrix} \tag{4.86}$$

$$j = 1,3,5,\ldots,N_y-1$$

where $t_j$ can be determined by the help of the odd and even boundary condition equation derived at the previous page. Besides that, terms $p_j$, $q_j$, and $r_j$ can be obtained in Eqs. (4.79) to (4.81). It can readily be seen that $p_j$, $q_j$, and $r_j$ were not defined for the cases of $j$ = 0 and $j$ = 1. Method of finding them is to compare the above matrix forms (4.85) and (4.86) with Equation (4.74).

Expressions that are derived from Eq. (4.74) are as follows:

$$b_0 - \delta C_0 = f_0$$
$$b_1 - \delta C_1 = f_1 \qquad (4.87)$$

By comparing Eq. (4.87) with the equations stemmed from the ones in matrices $p_0, q_0, r_0$ and $p_1, q_1, r_1$ can be found as in the below.

$$p_0 = -\delta, \quad q_0 = 1, \quad r_0 = 0$$

$$p_1 = -\delta, \quad q_1 = 1, \quad r_1 = 0$$

To sum up this procedure, system formed by the spectral integration method has $N_y + 3$ equations and $N_y + 3$ unknowns which consists of $N_y + 1$ $\{b_j\}$ coefficients and 2 integration constants $C_0$ and $C_1$. The system is split into odd and even matrices, and they are tridiagonal except for the top row derived from the boundary conditions. Thomas method is used to solve this matrix system and it is solved for $\{b_j\}$, which are the coefficients of $\tau''$ and two integration constants. Finally, the Chebyshev integration is performed twice to get $\{a_j\}$, which are the coefficients of $\tau$.

### 4.3.6. Computational Procedure

In this section, algorithm of the N-S solver will be examined. At the beginning of each time step, the following sets of data can be taken from the previous time step:

$$\tilde{u},\ \tilde{\upsilon},\ \tilde{w},\ \tilde{\omega}_x,\ \tilde{\omega}_y,\ \tilde{\omega}_z,\ \tilde{\theta},\ \frac{\partial\tilde{\theta}}{\partial x},\ \frac{\partial\tilde{\theta}}{\partial y},\ \frac{\partial\tilde{\theta}}{\partial z}$$

which are in Fourier space. They are transformed back to physical space by using inverse FFT. Then the non-linear terms can be calculated.

$$H_1 = \upsilon\omega_z - w\omega_y - \frac{\partial p}{\partial x} + \frac{RaSin\varphi}{Re^2\ Pr}\theta \tag{4.88}$$

$$H_2 = w\omega_x - u\omega_z - \frac{\partial p}{\partial y} + \frac{RaCos\varphi}{Re^2\ Pr}\theta \tag{4.89}$$

$$H_3 = u\omega_y - \upsilon\omega_x - \frac{\partial p}{\partial z} \tag{4.90}$$

$$h_T = -(u\frac{\partial\theta}{\partial x} + \upsilon\frac{\partial\theta}{\partial y} + w\frac{\partial\theta}{\partial z}) \tag{4.91}$$

which are then transformed to Fourier space by FFT. For each value of $\kappa^2 = \alpha_1{}^2 + \alpha_2{}^2$ and $\kappa \neq 0$,

$$\tilde{h}_g = i\alpha_2\tilde{H}_1 - i\alpha_1\tilde{H}_3 \tag{4.92}$$

and since

$$\tilde{h}_\upsilon = -\frac{\partial}{\partial y}\left(\frac{\partial\tilde{H}_1}{\partial x} + \frac{\partial\tilde{H}_3}{\partial z}\right) + \left(\frac{\partial^2}{\partial x^2} + \frac{\partial^2}{\partial y^2}\right)\tilde{H}_2 \tag{4.93}$$

part of $\tilde{h}_\upsilon$ can be rewritten as follows:

$$\tilde{h}_\upsilon = -\frac{\partial}{\partial y}\left(i\alpha_1\tilde{H}_1 + i\alpha_2\tilde{H}_3\right) - \left(\alpha_1{}^2 + \alpha_2{}^2\right)\tilde{H}_2 \tag{4.94}$$

The above data should be transformed to Fourier-Chebyshev space, and assembled to construct the RHS for each equation. Since RHS of each equation changes due to which method is used for temporal discretization, both cases will be examined separately.

$G$ -equation (AB/CN Scheme):

$$RHS_g = -3\,Re\,\hat{\tilde{h}}_g{}^{n} + Re\,\hat{\tilde{h}}_g{}^{n-1} - D^2\hat{\tilde{G}}^n + (\alpha_1{}^2 + \alpha_2{}^2)\hat{\tilde{G}}^n - \frac{2\,Re}{\Delta t}\hat{\tilde{G}}^n$$

where $\hat{\tilde{h}}_g{}^{n-1}$, $D^2\hat{\tilde{G}}^n$, $\hat{\tilde{G}}^n$ are stored from the previous time step.

$G$ -equation (AB/BDI2 Scheme):

$$RHS_g = -2\,Re\,\hat{\tilde{h}}_g{}^{n} + Re\,\hat{\tilde{h}}_g{}^{n-1} - \frac{Re}{\Delta t}(2\hat{\tilde{G}}^n - \frac{\hat{\tilde{G}}^{n-1}}{2})$$

where $\hat{\tilde{h}}_g{}^{n-1}$, $\hat{\tilde{G}}^n$, and $\hat{\tilde{G}}^{n-1}$ are provided from the previous time step.

$\upsilon$ -equation (AB/CN Scheme):

$$RHS_\upsilon = -3\,Re\,\hat{\tilde{h}}_\upsilon{}^{n} + Re\,\hat{\tilde{h}}_\upsilon{}^{n-1} - D^2\hat{\tilde{\phi}}_p{}^n + (\alpha_1{}^2 + \alpha_2{}^2)\hat{\tilde{\phi}}_p{}^n - \frac{2\,Re}{\Delta t}\hat{\tilde{\phi}}_p{}^n$$

After taking the Chebyshev derivative of the first part of $h_\upsilon$ with respect to y, other terms are added to assemble $h_\upsilon$. In the above relation, $\hat{\tilde{h}}_\upsilon{}^{n-1}$, $D^2\hat{\tilde{\phi}}_p{}^n$, and $\hat{\tilde{\phi}}_p{}^n$ are stored from the previous time step.

$\upsilon$ -equation (AB/BDI2 Scheme):

$$RHS_\upsilon = -2\,Re\,\hat{\tilde{h}}_\upsilon{}^{n} + Re\,\hat{\tilde{h}}_\upsilon{}^{n-1} - \frac{Re}{\Delta t}(2\hat{\tilde{\phi}}_p{}^n - \frac{\hat{\tilde{\phi}}_p{}^{n-1}}{2})$$

Same steps as in the AB/CN scheme are made before calculating $RHS_\upsilon$, and in the above relation $\hat{\tilde{h}}_\upsilon{}^{n-1}$, $\hat{\tilde{\phi}}_p{}^n$, and $\hat{\tilde{\phi}}_p{}^{n-1}$ are taken from the previous time step.

$\theta$-equation (AB/CN Scheme):

$$RHS_T = -3\,Re\,Pr\,\hat{\tilde{h}}_T{}^{n} + Re\,Pr\,\hat{\tilde{h}}_T{}^{n-1} - D^2\hat{\tilde{\theta}}^n + (\alpha_1{}^2 + \alpha_2{}^2)\hat{\tilde{\theta}}^n - \frac{2\,Re\,Pr}{\Delta t}\hat{\tilde{\theta}}^n$$

where $\hat{\tilde{h}}_T{}^{n-1}$, $D^2\hat{\tilde{\theta}}^n$, and $\hat{\tilde{\theta}}^n$ are stored from the previous time step.

$\theta$-equation (AB/BDI2 Scheme):

$$RHS_T = -2\,Re\,Pr\,\hat{\tilde{h}}_T{}^{n} + Re\,Pr\,\hat{\tilde{h}}_T{}^{n-1} - \frac{Re\,Pr}{\Delta t}(2\hat{\tilde{\theta}}^n - \frac{\hat{\tilde{\theta}}^{n-1}}{2})$$

where $\hat{\tilde{h}}_T{}^{n-1}$, $\hat{\tilde{\theta}}^n$ and $\hat{\tilde{\theta}}^{n-1}$ are stored from the previous time step.

Next step is to send these variables into vertical solver in order to solve the system in Fourier-Chebyshev space. Methodology of vertical solver is spectral integration that is described in the previous section. The vertical solver gives the solutions of $\hat{\tilde{\upsilon}}, \hat{\tilde{G}}, \hat{\tilde{G}}', \hat{\tilde{f}}, \hat{\tilde{\phi}}, \hat{\tilde{\theta}}, \hat{\tilde{\theta}}'$. Prime denotes derivative with respect to y. These are converted back to Fourier space and are used to determine other desired variables such as:

$$\tilde{u},\ \tilde{w},\ \tilde{\omega}_x,\ \tilde{\omega}_z,\ \frac{\partial\tilde{\theta}}{\partial x},\ \frac{\partial\tilde{\theta}}{\partial z}$$

It is known that from continuity equation, we can write the following equation:

$$i\alpha_1\tilde{u} + i\alpha_2\tilde{w} = -\tilde{\upsilon}' \qquad (4.95)$$

and from the definition of $G$ the following equation can be also obtained:

$$i\alpha_2\tilde{u} - i\alpha_1\tilde{w} = \tilde{G} \qquad (4.96)$$

By solving Eqs. (4.95) and (4.96) simultaneously,

$$\begin{aligned} \tilde{u} &= \frac{i}{\kappa^2}\left(\alpha_1\tilde{\upsilon}' - \alpha_2\tilde{G}\right) \\ \tilde{w} &= \frac{i}{\kappa^2}\left(\alpha_2\tilde{\upsilon}' + \alpha_1\tilde{G}\right) \end{aligned} \qquad (4.97)$$

Also using the relations for $w_x$, $w_z$,and $\tilde{G}$, $\phi$, the following relations are found:

$$\begin{aligned}\tilde{w}_x &= \frac{i}{\kappa^2}\left(\alpha_1\tilde{G}' + \alpha_2\tilde{\phi}\right) \\ \tilde{w}_z &= \frac{i}{\kappa^2}\left(\alpha_2\tilde{G}' - \alpha_1\tilde{\phi}\right)\end{aligned} \tag{4.98}$$

For the temperature equation, we can get

$$\begin{aligned}\frac{\partial\tilde{\theta}}{\partial x} &= \alpha_1\tilde{\theta} \\ \frac{\partial\tilde{\theta}}{\partial z} &= \alpha_2\tilde{\theta}\end{aligned} \tag{4.99}$$

It should be also noticed the separation of real and imaginary parts of coefficients in Fourier space. All the data in the form of Fourier coefficients have to be split into two sets of real data and the calculations have to be carried out corresponding to these two sets of data. For example, when $\tilde{h}_g$ is calculated, following equation is used.

$$\tilde{h}_g = i\alpha_2\tilde{H}_1 - i\alpha_1\tilde{H}_3$$

but it should be separated into real and imaginary parts in order to get the following two equations.

$$\tilde{h}_{gr} = -\alpha_2\tilde{H}_{1im} + \alpha_1\tilde{H}_{3im} \tag{4.100}$$

$$\tilde{h}_{gim} = i\left(\alpha_2\tilde{H}_{1r} - \alpha_1\tilde{H}_{3r}\right) \tag{4.101}$$

These two sets of data are then converted to Chebyshev space separately, and the vertical solver is called twice to give the solutions for real and imaginary parts.

For $\kappa$=0, everything is real, even in Fourier space. Same procedure is applied for this case also. Equations are solved directly and it is known that

$$\tilde{G} = i\alpha_2\tilde{u} - i\alpha_1\tilde{w} = 0 \text{ and } \tilde{\upsilon} = 0$$

which is from continuity and the boundary conditions at walls for $\upsilon$.

# CHAPTER 5

# RESULTS AND DISCUSSION

## 5.1. Introduction

In this study, laminar natural convection flow and heat transfer between two inclined parallel plates are analyzed numerically by using a pseudospectral technique. After following the computational procedure as is discussed in Section 4.3.6, non-dimensional velocity and temperature fields inside the channel and three non-dimensional velocity components at a specified location are obtained. By utilizing these data, streamlines and velocity versus time graphs of the data are plotted using MATLAB. Additionally, Nu calculations are also performed. To get a more detailed view, local Nu values at collocation points in x and z directions are calculated. In most of the calculations, 65 collocation points in y direction, and 32 collocation points in x and z directions are used. Therefore when three dimensional runs are performed, 32 x 65 x 32 data for each of the velocity and temperature fields are obtained by the program. Additional subroutines in C code are written to post-process large amount of data obtained, and also to calculate the local and average Nu values.

In Chapter 4, it is expressed in detail that AB/CN and AB/BDI2 techniques are used for time discretization. Plots of the time change of velocity at a preselected point contribute to make the comparison of the results for the same cases with different temporal discretizations. After the comparison, the remainder of the runs throughout the study are performed with AB/BDI2 discretization technique. Moreover grid independence of the computational study is examined by doubling collocation points in all directions, i.e. 64 points in x and z directions, 128 points in y direction. Then, the common cases for both grid combinations are chosen and the comparison is made. For the sake of completeness, two dimensional results of the study are also presented. The main motivation was to see whether the critical inclination angle can be calculated by performing 2-D runs or not. Since at the specified Ra, the program is run for several inclination angles, in order to get our results faster two dimensional cases are preferred. Unfortunately, the 2-D runs did not give satisfactory results. Nevertheless, these analyses show that natural convection between two inclined parallel plates should be considered as three dimensional in order to get more accurate results. In the following section, the local and average Nu calculations will be examined in detail, after that all the results will be presented and evaluated.

## 5.2. Calculation of Nusselt Number

As mentioned in the previous section, after analyzing the flow and obtaining the temperature and velocity fields, in order to evaluate the results and compare them with the literature, the average Nu has to be found. In this section, the method of calculation of Nu will be introduced in detail.

This study is performed by solving an unsteady Navier-Stokes and energy equations. However, calculation of Nu will be done in steady regime of the solution. For this reason, the time interval that the solution reaches to steady state should be determined. At steady state, the energy balance on the lower plate is:

$$-k\left.\frac{\partial T}{\partial y}\right|_{\text{lower plate}} = h\left(T_w - T_\infty\right) \tag{5.1}$$

where $k$ is the thermal conductivity of the fluid, $h$ is the local heat transfer coefficient of the fluid, $T_w$ is the local wall temperature of the lower plate, $T_\infty$ is the mean temperature of the fluid. The temperature gradient term on the left hand side is local, and it is calculated for every x and z locations. When the both sides of the Eqn. (5.1) are multiplied by $L_y/k$ , it becomes:

$$Nu = \frac{-L_y \left.\frac{\partial T}{\partial y}\right|_{\text{lower plate}}}{T_w - T_\infty}, \text{ where } Nu = \frac{hL_y}{k} \tag{5.2}$$

Nu is defined as local Nusselt number and it is also calculated for every x and z location. To get the average Nu, the mean value of the local terms in every x and z locations is calculated. Before that, Eqn. (5.2) has to be non-dimensionalized, since all the results of the program are non-dimensional, e.g. temperature and velocity values.

Let

$$\left.\frac{\partial T}{\partial y}\right|_{\text{lower plate}} = \frac{\Delta T}{L_y}\left.\frac{\partial \theta^*}{\partial y^*}\right|_{\text{lower plate}} \tag{5.3}$$

and

$$\begin{aligned} T_w &= \Delta T \theta_w^* + T_m \\ T_\infty &= \Delta T \theta_\infty^* + T_m \end{aligned} \tag{5.4}$$

When Eqns. (5.3) and (5.4) are put into Eqn. (5.2) the non-dimensional form of the Nu is obtained as follows:

$$Nu = \frac{-\left.\dfrac{\partial \theta^*}{\partial y^*}\right|_{\text{lower plate}}}{\left(\theta_w^* - \theta_\infty^*\right)} \tag{5.5}$$

The temperature gradient term in Eqn. (5.5) can be approximated as,

$$\left.\frac{\partial \theta^*}{\partial y^*}\right|_{y=-1} \cong \left.\frac{\Delta \theta^*}{\Delta y^*}\right|_{y=-1} \tag{5.6}$$

where $\Delta y^*$ is the distance between the lowermost collocation points. $\theta_\infty{}^*$ is calculated by taking the mean of each $\theta^*$ value of the fluid in y direction.

For two dimensional cases, by implementing Eqns. (5.5) and (5.6), 32 or 64 local Nu values in x direction, depending on how many collocation points are used, are calculated. Average Nu values for each time step are found by taking the average of 32 or 64 Nu values in x direction.

On the other hand, when z direction is also taken into account, again by using Eqns. (5.5) and (5.6), 32 or 64 local Nu values at all x and z locations are calculated. Average Nu values are found at each time step, by taking mean of $32 \times 32$ or $64 \times 64$ Nu values depending on the number of collocation points used.

In the three dimensional case, when calculating 32 or 64 Nu values in x direction, averages of Nu values in z direction at the specified x locations are taken; similarly when calculating 32 or 64 Nu values in z direction, averages of Nu values in x direction at the specified z locations are taken.

In the following sections, interpretation of the results will be made by the aid of the figures. In addition to average Nu figures, local Nu with respect to time will also be shown. In order to compare the results with the literature studies properly, average Nu is plotted with respect to the $Ra\cos\varphi$ where $\varphi$ is the inclination angle.

## 5.3. The Convergence Criteria

In this study, the convergence is defined in two general ways. The results are expected either to reach a steady value or to become time periodic. If one or the other is obtained, it is considered that the convergence is achieved. In order to understand the convergence of the results, plots of dimensionless velocity versus dimensionless time are presented. In these graphs, it is understood that at different Ra values and inclination angles, the convergence characteristics of the results vary. For example, when $Ra\cos\varphi$ is equal to 1708, dimensionless velocity values reach to a constant value within the specified time interval, however when $Ra\cos\varphi$ is increased to 10000, for any tilt angle, the results do not converge to a steady value, instead the time periodicity of the values are obtained, i.e. during oscillations, maximum and minimum values of the dimensionless velocities do not change after some t* value.

Additionally, when average Nu graphs are considered, the same convergence criteria are applied. If the average Nu value converges to a constant value after some t* value, it is taken as the desired average Nu value for the specified $Ra\cos\varphi$ and $\varphi$ values. On the other hand, again when $Ra\cos\varphi$ and $\varphi$ are increased to higher values, average Nu values fluctuate continuously within the specified time interval. If the situation is like that, the time average of Nu values is taken in order to obtain the desired average Nu value. Maximum and minimum values of average Nu values at different $Ra\cos\varphi$ and $\varphi$ values are tabulated in Table 5.1. By using these values, it can be decided that whether the time averaging of Nu values can be performed or not.

In Table 5.1, Racosφ values at which convergence with constant values can not be achieved are tabulated. If the difference between the maximum and minimum average Nu values is small, then time average of these Nu values can be performed. However, if this difference is considerably large, the time average of the results have considerable errors. The average Nu values obtained from Eqns. 5.8-9 are also given in Table 5.1. As it can easily be seen from Table 5.1, for Racosφ = 50000 at φ = 30°, for Racosφ = 20000 and 50000 at φ = 45° and for Racosφ = 10000 and 50000 at $\varphi = 60^\circ$, the discrepancies between the maximum and minimum average Nu values are larger than the other cases. On the other hand, the maximum average Nu values of the previously mentioned cases are closer to the values in the literature. In order to decide time end of the program, again the same convergence criteria is used. If the convergence is achieved within the predetermined time, it is considered that the time end is appropriate.

**Table 5.1.** The Maximum and Minimum Average Nu Values with the Average Nu Values obtained by Eqns. 5.8-9 when t* = 2-10

| **φ(deg)** | **Racosφ** | **Max. Av. Nu** | **Min. Av. Nu** | **Av. Nu ( Eqn. 5.8 )** | **Av. Nu ( Eqn. 5.9 )** |
|---|---|---|---|---|---|
| 15 | 20000 | 2.772 | 2.318 | 2.793 | 2.825 |
| | 50000 | 3.872 | 3.179 | 3.424 | 3.438 |
| 30 | 20000 | 2.802 | 2.324 | 2.745 | 2.825 |
| | 50000 | 3.675 | 2.130 | 3.404 | 3.438 |
| 45 | 10000 | 2.661 | 2.051 | 2.191 | 2.391 |
| | 20000 | 2.868 | 1.104 | 2.715 | 2.825 |
| | 50000 | 3.464 | 1.664 | 3.391 | 3.438 |
| 60 | 10000 | 2.301 | 0.951 | 2.203 | 2.391 |
| | 50000 | 3.967 | 1.745 | 3.394 | 3.438 |

## 5.4. Comparison of AB/CN and AB/BDI2 Schemes

The original time discretization scheme in our Navier Stokes solver is AB/CN, however Peyret [27] suggests by saying,

> "For Fourier approximation, the AB/BDI2 scheme is unconditionally stable for $\nu/|a| \geq 1$, while the stability of AB/CN scheme requires a condition on the time step. AB/CN scheme was found to be unstable when applied to the Navier-Stokes equations approximated with Chebyshev tau method, so that the AB/BDI2 scheme was preferred by Vanel et al."

In the above quotation, $\nu$ is the kinematic viscosity, $a$ is the advective velocity defined for the advection-diffusion equation introduced in Section 3.4. Since $a$ is very low in this study because of the quiescent fluid, $\nu/|a|$ is expected to be sufficiently large, and moreover Chebyshev tau method is also used in the spectral integration. According to the quoted statement, AB/BDI2 scheme is chosen for temporal discretization. In order to justify this choice, one sample case is considered and the variation of dimensionless streamwise velocities with respect to time at [32][16][16] for the both schemes are compared. In this case, $Ra = 20000, Pr = 0.7$, approximate value for air, $dt = 1\times10^{-4}$ and inclination angle of $15^\circ$. The results are shown in Figures 5.1-2.

In Figures 5.1 and 5.2, the dimensionless axial velocity with respect to time is plotted for the schemes of AB/BDI2 and AB/CN, respectively. The former one shows that after the usual initial setting of the solution at $t^* \cong 20$, there is a sharp decrease and they do not tend to increase to higher values again. Additionally, oscillations of velocity after this point decrease considerably. In the latter figure, a sharp decrease occurs again at $t^* \cong 20$. On the other hand, the values of the dimensionless velocity increase after some point and start to oscillate more. Due to the smaller oscillations, AB/BDI2 method is considered to be more stable for this study.

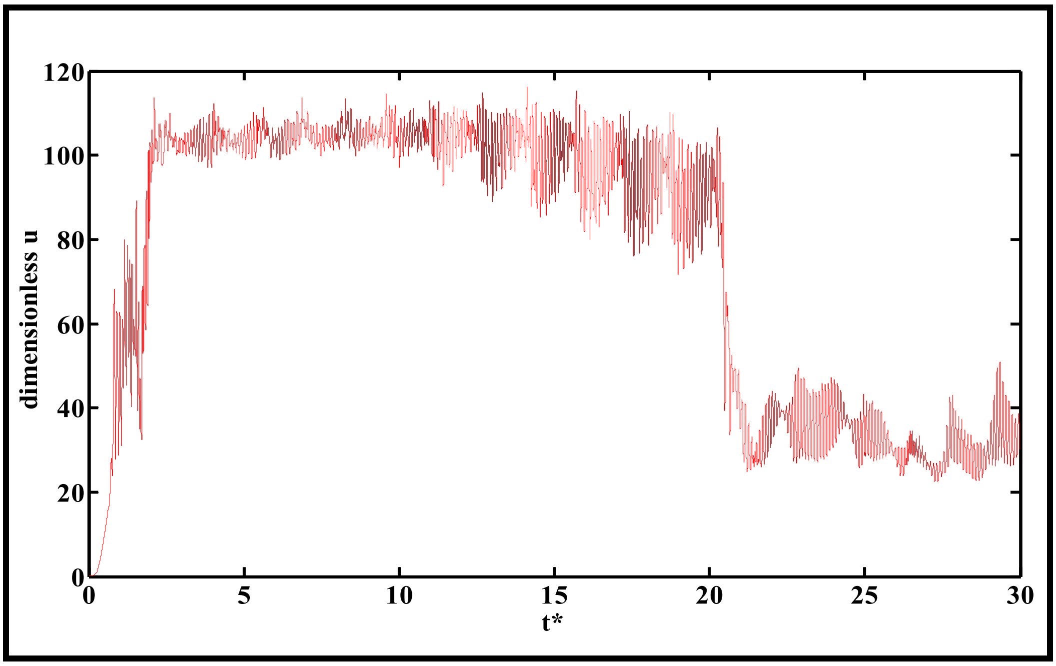

**Figure 5.1.** Dimensionless u versus $t^*$ when $Ra = 20000$ and $\varphi = 15^\circ$ with AB/BDI2 Scheme at [32][16][16]

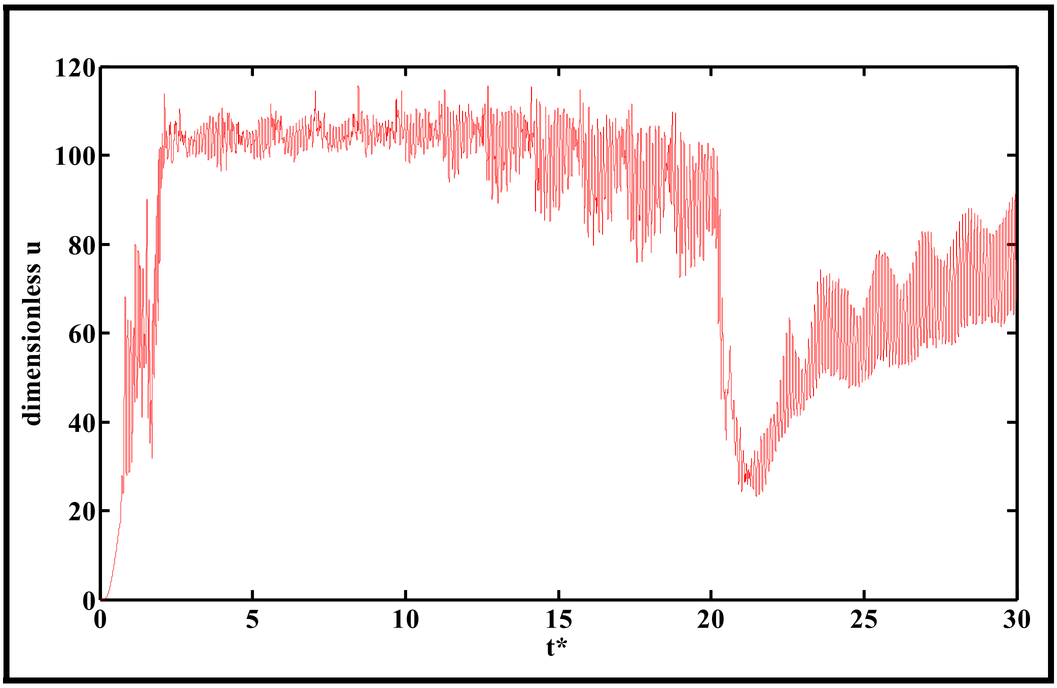

**Figure 5.2.** Dimensionless u versus $t^*$ when $Ra = 20000$ and $\varphi = 15^\circ$ with AB/CN Scheme at [32][16][16]

In order to show the stability of AB/BDI2 scheme, one of the test cases is also run with AB/CN scheme. Figure 5.3 shows the variation of non-dimensional streamwise velocity with respect to dimensionless time when $Ra\cos\varphi = 10000$ at $\varphi = 15^\circ$ with AB/CN Scheme. When Figure 5.3 is compared with Figure 5.25 where AB/BDI2 scheme is used, the steady state oscillations are in a larger margin in the former one. For this reason, it can be said that the difference between the maximum and minimum velocity values in AB/BDI2 scheme is smaller within the time interval where the constant periodicity is reached. Besides that higher velocity values occurred in AB/CN scheme. Due to that, the steady state values are also higher than the ones in AB/BDI2 scheme.

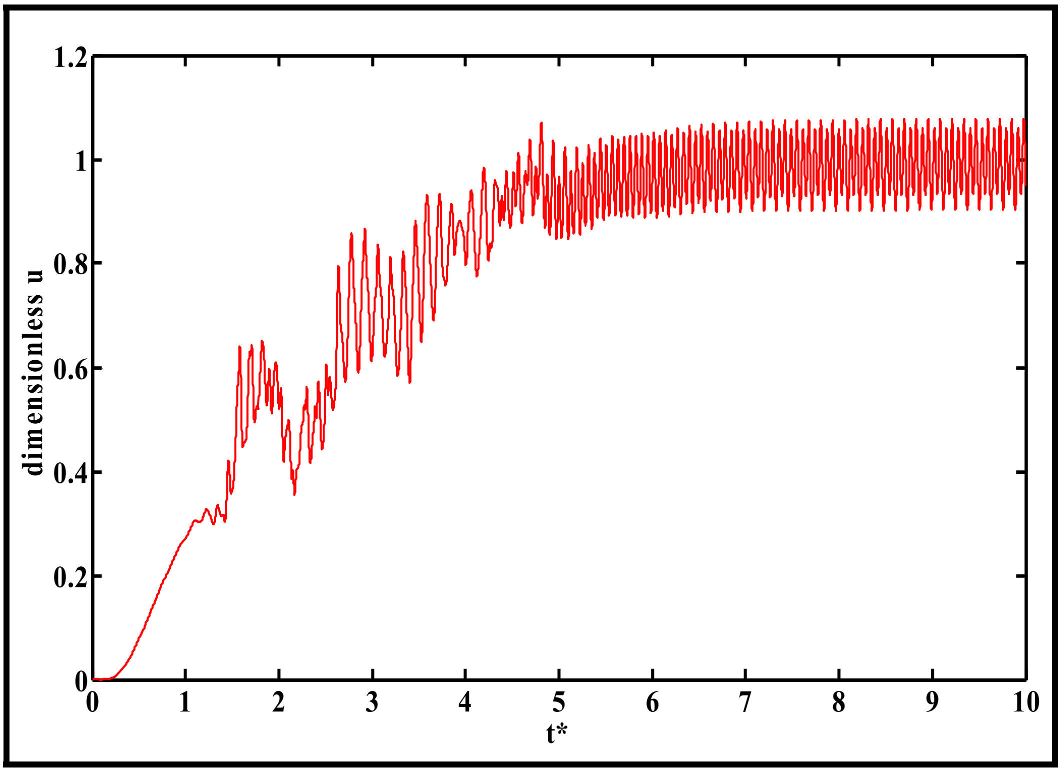

**Figure 5.3.** Dimensionless u versus $t^*$ when $Ra\cos\varphi = 10000$ and $\varphi = 15^\circ$ with AB/CN Scheme at [2][2][2]

## 5.5. The Results of 3-D Runs for Air

In this section, the results of this study will be compared with the experimental results of Hollands et al [4]. They have analyzed inclined air layers in a channel with high aspect ratio which corresponds to a similar geometry of our study since we have infinite plates. They have also used constant wall temperature boundary condition. Hollands et al. [4] started their study by taking the horizontal case as a reference point and by introducing $cos\,\varphi$ into the $Ra$ term of horizontal channel. For this purpose, $Ra\,cos\,\varphi$ was taken in the range $1708 \le Ra\,cos\,\varphi \le 5\times10^4$, and inclination angle from horizontal, $\varphi$ was taken in the range $15^\circ \le \varphi \le 60^\circ$. As a result, they obtained two empirical correlations between Nu and $Ra\,cos\,\varphi$:

$$Nu = 1 + 1.44\left[1-\frac{1708}{Ra\,cos\,\varphi}\right]^*\left(1-\frac{(sin1.8\varphi)^{1.6}\,1708}{Ra\,cos\,\varphi}\right)+\left[\left(\frac{Ra\,cos\,\varphi}{5830}\right)^{1/3}-1\right]^* \qquad (5.7)$$

$$Nu = 1 + 1.44\left[1-\frac{1708}{Ra\,cos\,\varphi}\right]^*+\left[\left(\frac{Ra\,cos\,\varphi}{5830}\right)^{1/3}-1\right]^* \qquad (5.8)$$

where $[\;]^*$ is defined as:

$$[X]^* = (|X| + X)/2 \qquad (5.9)$$

Similarly, in our study, the range of $Ra\,cos\,\varphi$ is taken as the same. But since the computational time of getting data for 3-D case is too long, only three $Ra\,cos\,\varphi$ values within the specified range are taken into account. These are 1708, $10^4$ and $5\times10^4$. However, $\varphi$ is taken as the same $\varphi$ values used in the experimental one. Those are $15^\circ, 30^\circ, 45^\circ$ and $60^\circ$. Apart from the Hollands' study, local Nu values in streamwise and spanwise directions are also calculated. The comparison is made between the average Nusselt numbers and they are shown graphically after presenting the local results. Furthermore, dimensionless velocity profiles, streamlines and some additional figures about the fluid flow will be shown also for the sake of versatility.

Figure 5.4 shows the variation of the average Nu value with respect to time for the case of $Ra\,cos\,\varphi = 1708$ at $\varphi = 15^\circ$ . In the literature, it is proven by the experimental studies that critical $Ra\,cos\,\varphi$ for passing to the convective regime from conductive regime is 1708. Below this value, flow regime is purely conductive i.e. Nu = 1 except at the extreme ends of the plates where the fluid turns and there becomes some convective heat transfer. But since the plates are infinitely long in streamwise directions, these end effects are readily neglected. By using the Eqns. (5.8) and (5.9), the average Nu value should be found unity for this case, and Figure 5.4 indicates that after the system reaches to the steady state, the expected Nu value is obtained. The initial fluctuations in Figure 5.4 show the regime where the solution is not steady yet. Figure 5.5 also clearly shows that there is no convective motion at $Ra\,cos\,\varphi = 1708$.

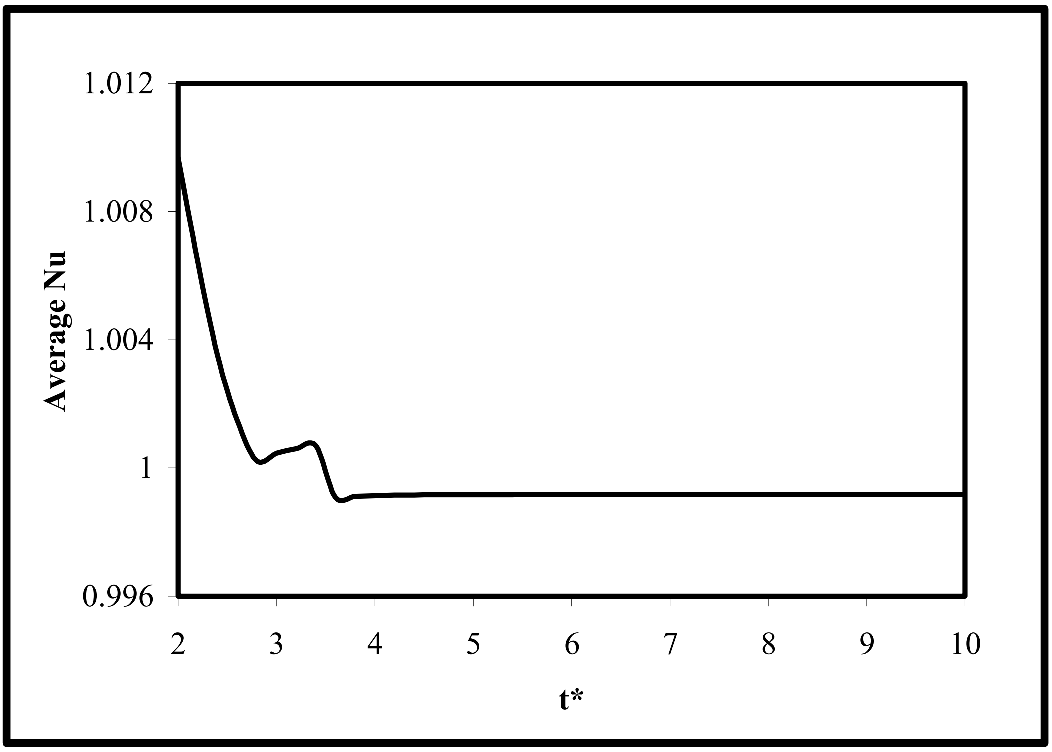

**Figure 5.4**. Average Nu value versus $t^*$ where $Ra\,cos\,\varphi = 1708$ and $\varphi = 15^\circ$

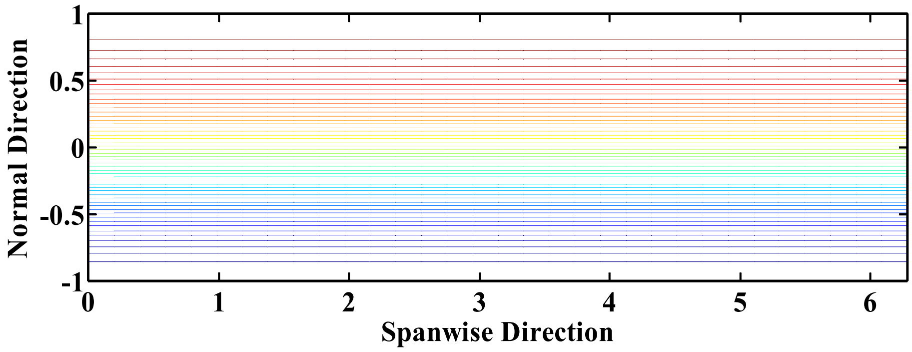

**Figure 5.5.** Streamlines in y-z plane when $Ra\cos\varphi = 1708$ and $\varphi = 15^{\circ}$ at $t^{*} = 6$

Figure 5.6 demonstrates the variation of the local Nu in the streamwise direction for the case of $Ra\,cos\,\varphi = 10000$ with $\varphi = 15^{\circ}$ at different times. In order to show the oscillations before the steady state, variations at $t^{*}$ = 2 and 4 are also given. Actually, the data are obtained between $t^{*}$ = 2 and $t^{*}$ = 10. But to present the data more properly, only three time steps are chosen, and since $t^{*}$ = 6 is the point where the Nu value does not change anymore, thus there is no need to show the values after that point. The horizontal axis of the graph is changing from 0 to $2\pi$ . It can be easily realized that when $Ra\,cos\,\varphi$ is increased above 1708, Nu values start to differ from unity and for this case Nu converges to an approximate value of 2.2.

Figure 5.7 illustrates the variation of local Nu along the spanwise direction when $Ra \cos\varphi = 10000$ and $\varphi = 15^\circ$ in different time steps. After making different wavy motions in different time steps of $t^* = 2$ and $t^* = 4$, the final form of the Nu values is reached approximately at $t^* = 6$. The horizontal axis of the graph is again changing from 0 to $2\pi$. Since the spanwise direction is expanded in Fourier series, Fourier collocation points are used as done in x direction, too. The local Nu values in z direction vary between 1 and 3. Around z = 3, Nu reaches to a minimum and rises to its minimum value around z = 5.5. As can be seen from Figure 5.8, the minimum and the maximum points correspond to downwash and upwash zones of partially formed convection cells.

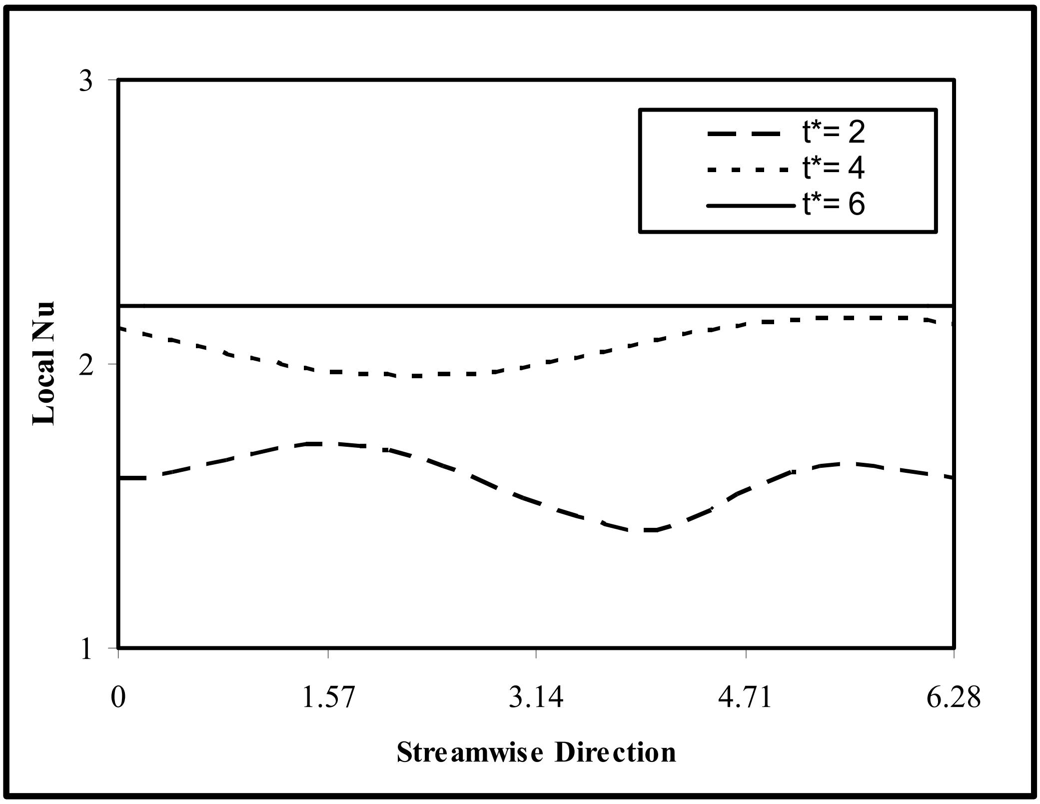

**Figure 5.6**. Local Nu value in streamwise direction where $Ra \cos\varphi = 10000$ and $\varphi = 15^\circ$

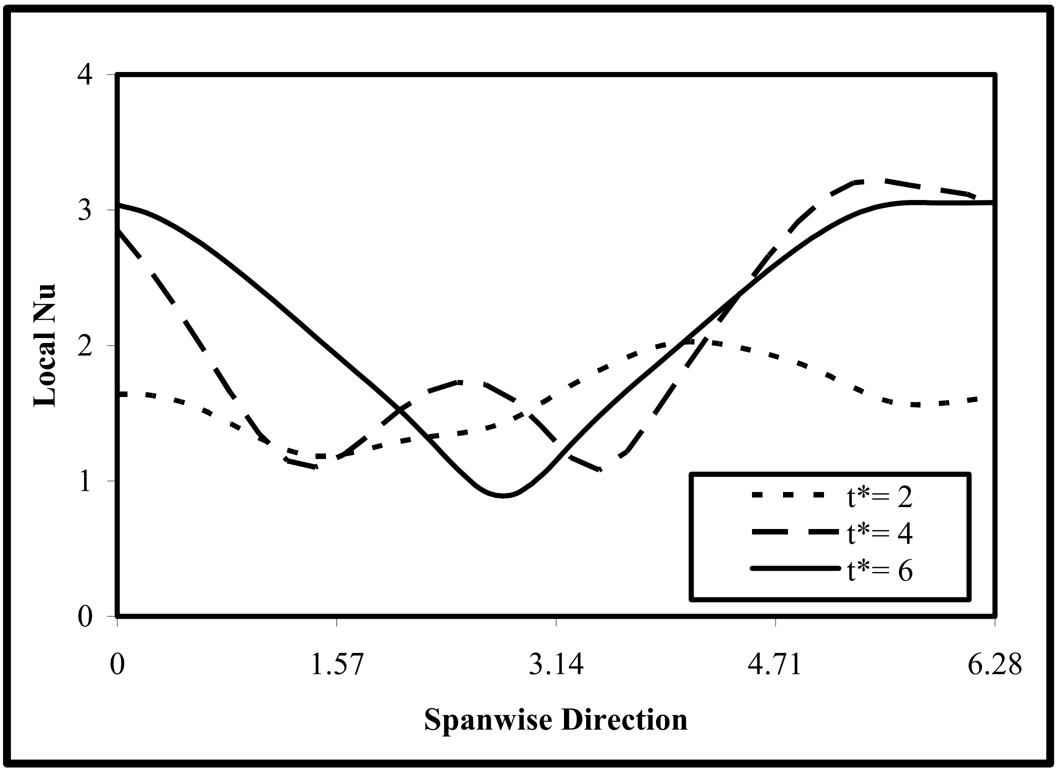

**Figure 5.7.** Local Nu value in spanwise direction where $Ra\cos\varphi = 10000$ and $\varphi = 15^\circ$

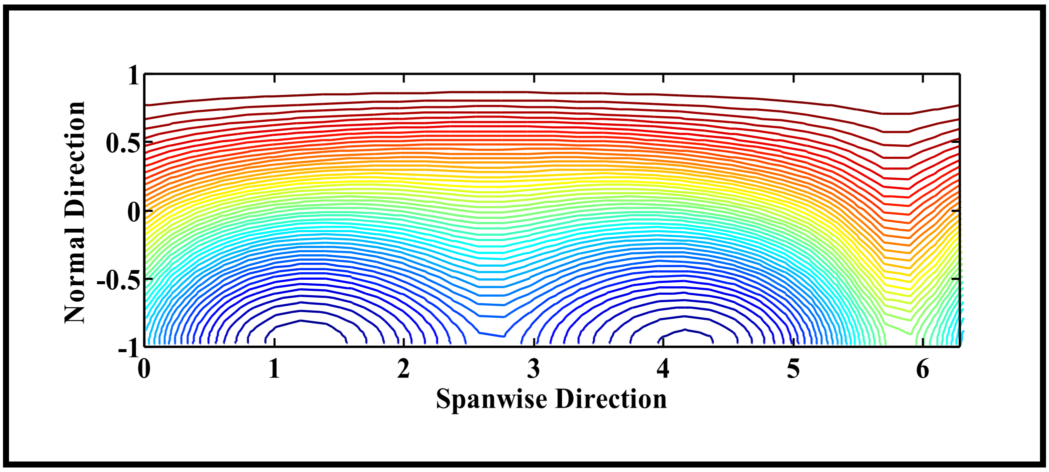

**Figure 5.8.** Streamlines in y-z plane when $Ra\cos\varphi = 10000$ and $\varphi = 15^\circ$ at $t^* = 6$

The changes in average Nu value with respect to time where $Ra\cos\varphi = 10000$ and $\varphi = 15^\circ$ are shown in Figure 5.9. As explained before, both local values of Nu reach steady state at $t^*$ = 6, similarly and consistently average values converge to a constant value near $t^*$ = 6. Until the steady state point, there are some oscillations in the average values. These can be explained by the effects of local Nu values in the average terms. In addition, it can be argued that apart from $Ra\cos\varphi = 1708$, the convection regime is dominant and Nu values differ from unity. Lastly, as in Figure 5.6, average Nu value approaches to the value of approximately 2.2.

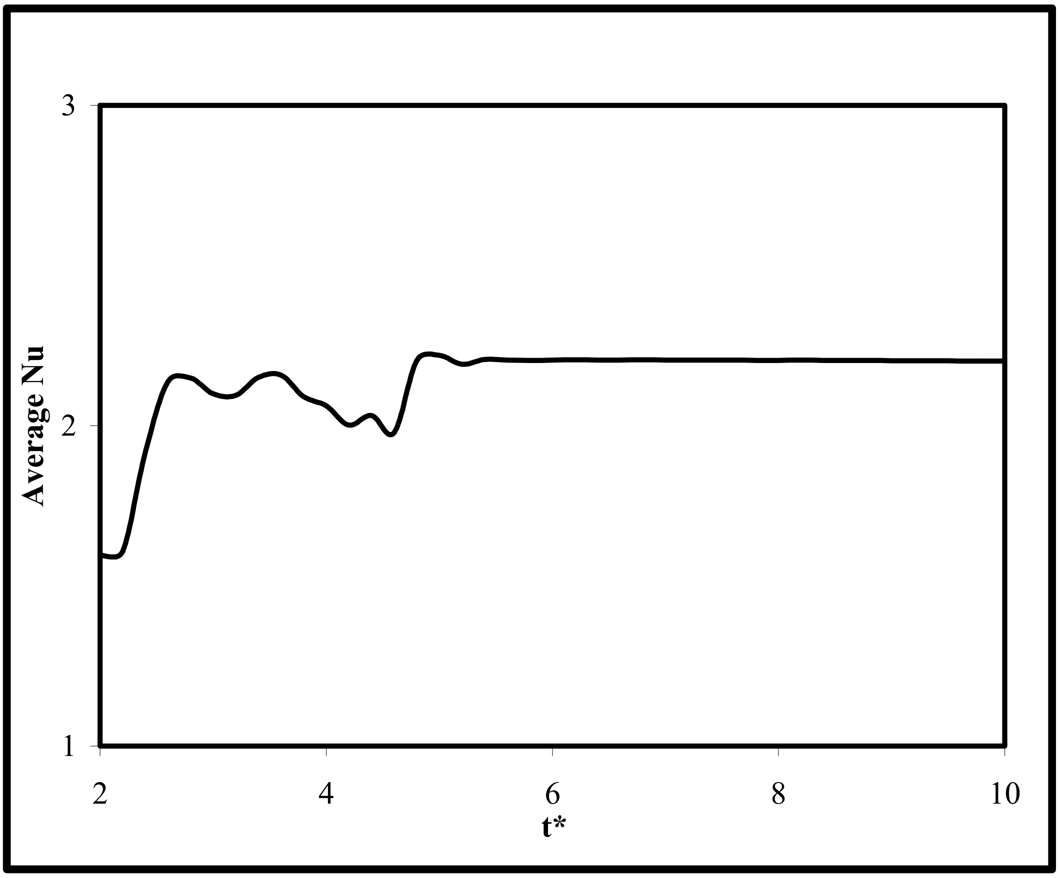

**Figure 5.9**. Average Nu value versus $t^*$ where $Ra\cos\varphi = 10000$ and $\varphi = 15^\circ$

Figure 5.10 shows the variation of the local Nu in x direction when $Ra\, cos\, \varphi = 50000$ and tilt angle from the horizontal is $15^\circ$. Again, the horizontal axis of the graph varies between 0 and $2\pi$, moreover Nu values are also plotted for three different time steps. However, in the later figures, it will be shown that for this value of $Ra\, cos\, \varphi$ at $\varphi = 15^\circ$, the results do not converge, i.e. local Nu values at $t^*$ = 10 are not in the final form. The oscillations continue around different values at each time step. In order to overcome this problem, the time increment of the code should be decreased.

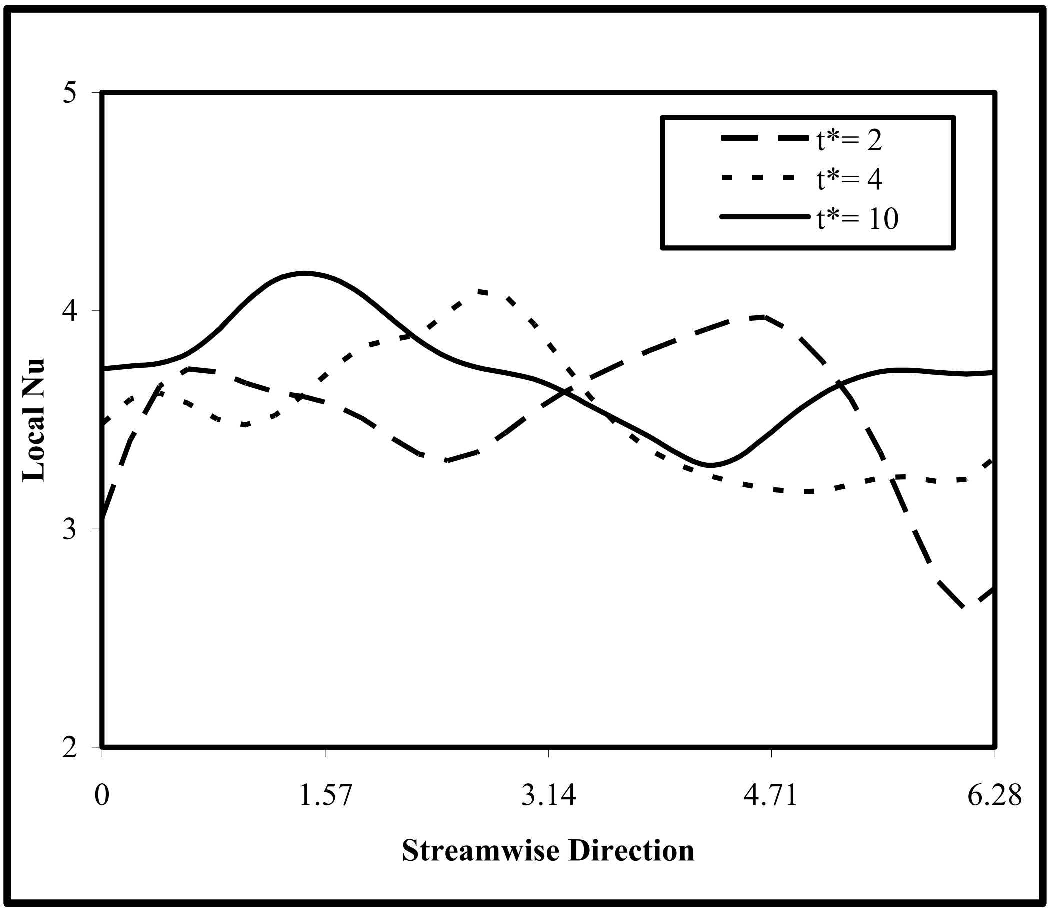

**Figure 5.10.** Local Nu value in streamwise direction where $Ra\, cos\, \varphi = 50000$ and $\varphi = 15^\circ$

The variation of local Nu in spanwise direction for the case of $Ra\cos\varphi = 50000$ and $\varphi = 15^{\circ}$ is plotted in Figure 5.11. Three time steps are used to illustrate the local Nu values and since values do not converge as in the previous case, the last time step is shown also. It can again be stated that because of the magnitude of inclination, the oscillations do not differ considerably from each other. It can be remarked that the tendency of the graph is a periodic motion which is shifted at each time step. Again, it can be stated that because of the convection rolls in the spanwise direction as shown in Figure 5.12, inflection points for Nu values in the z direction can be seen. Moreover, since there are multiple pairs of convection rolls seen in Figure 5.12, more than one inflection points are observed in Figure 5.11.

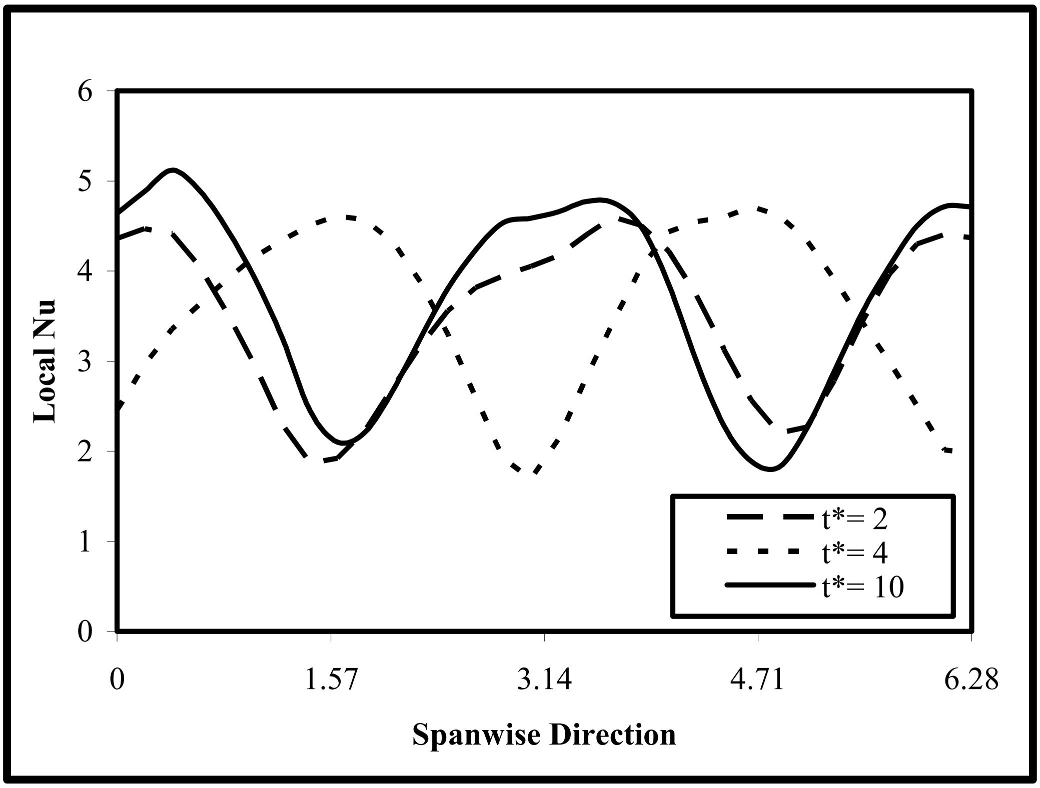

**Figure 5.11**. Local Nu value in spanwise direction where $Ra\cos\varphi = 50000$ and $\varphi = 15^{\circ}$

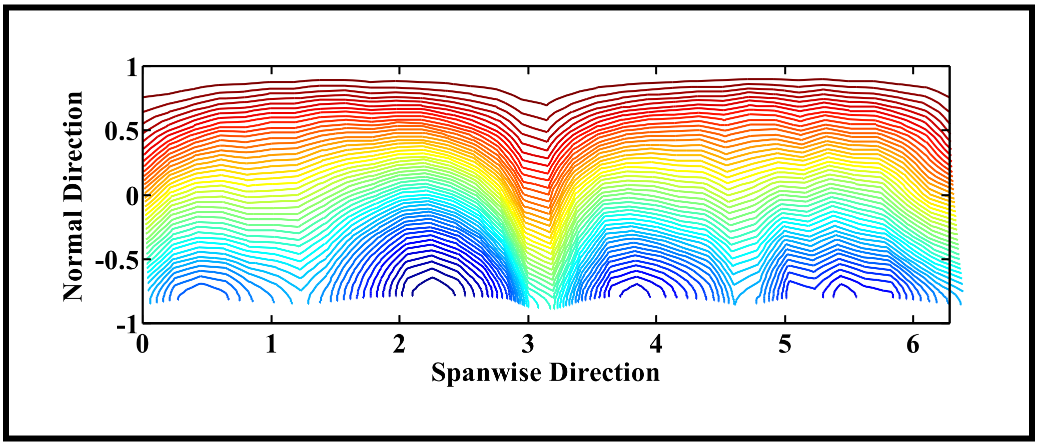

**Figure 5.12.** Streamlines in y-z plane when $Ra\cos\varphi = 50000$ and $\varphi = 15^\circ$ at $t^* = 10$

Figure 5.13 shows the time change of average Nu where $Ra\cos\varphi = 50000$ at $\varphi = 15^\circ$. Since the local Nusselt numbers do not converge, average Nu does not reach also. The trend of the Figure 5.13 is like in a periodic behavior that the mean value of the average values is used for comparison with the average Nu of the experimental study [4]. For this reason, an error occurs in these calculations, but in order to get more accurate results it can again be advised that time increment should be decreased to a level for convergence however time cost increases in a great amount. Figure 5.14 indicates the behavior of the average Nu with respect to time where $Ra\cos\varphi = 1708$ at $\varphi = 30^\circ$**.** Nu values are equal to the values of the case at $\varphi = 15^\circ$. Since $Ra\cos\varphi = 1708$ is the critical value for the transition from pure conduction to convective regime, convergence of Nu to unity verifies the validity of the results. Results between $t^*$ = 2 and $t^*$ = 10 are shown in the above figure. It will be shown by using the figures that demonstrate the variation of dimensionless velocities due to the time that velocity of the air starts to converge to some constant value or to reach steady state case in a periodic manner, i.e. repeating oscillations between these time values. For this reason, all the graphs related to Nu are plotted between $t^*$ = 2 and $t^*$ = 10.

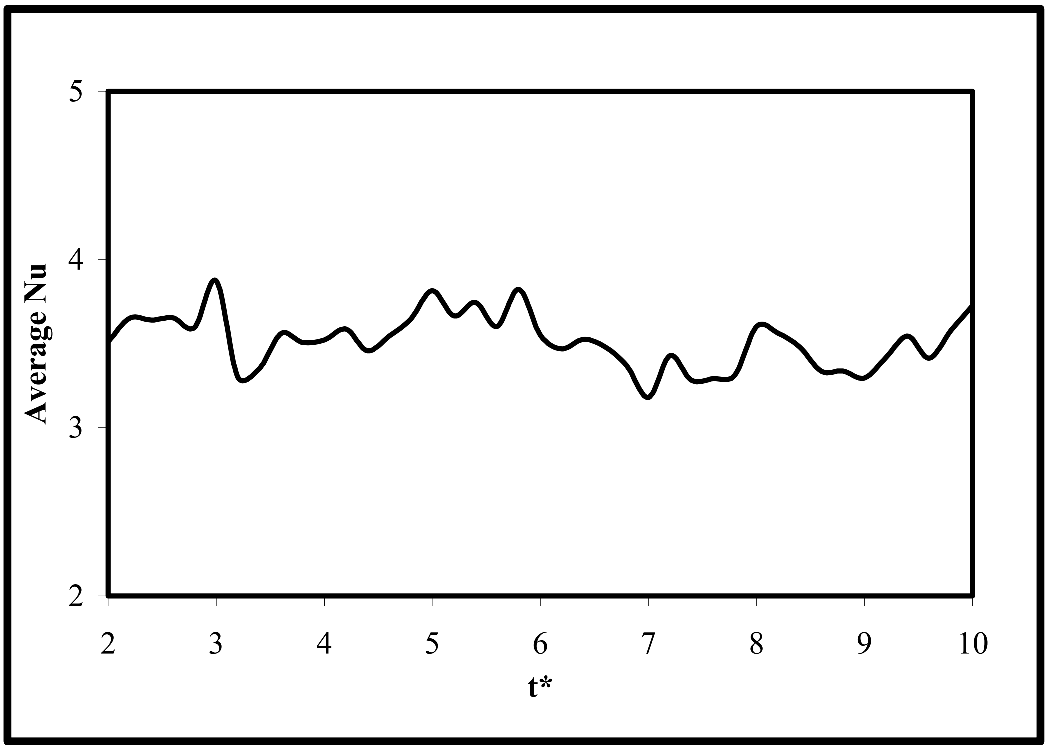

**Figure 5.13.** Average Nu value versus $t^*$ where $Ra\,cos\,\varphi = 50000$ and $\varphi = 15^\circ$

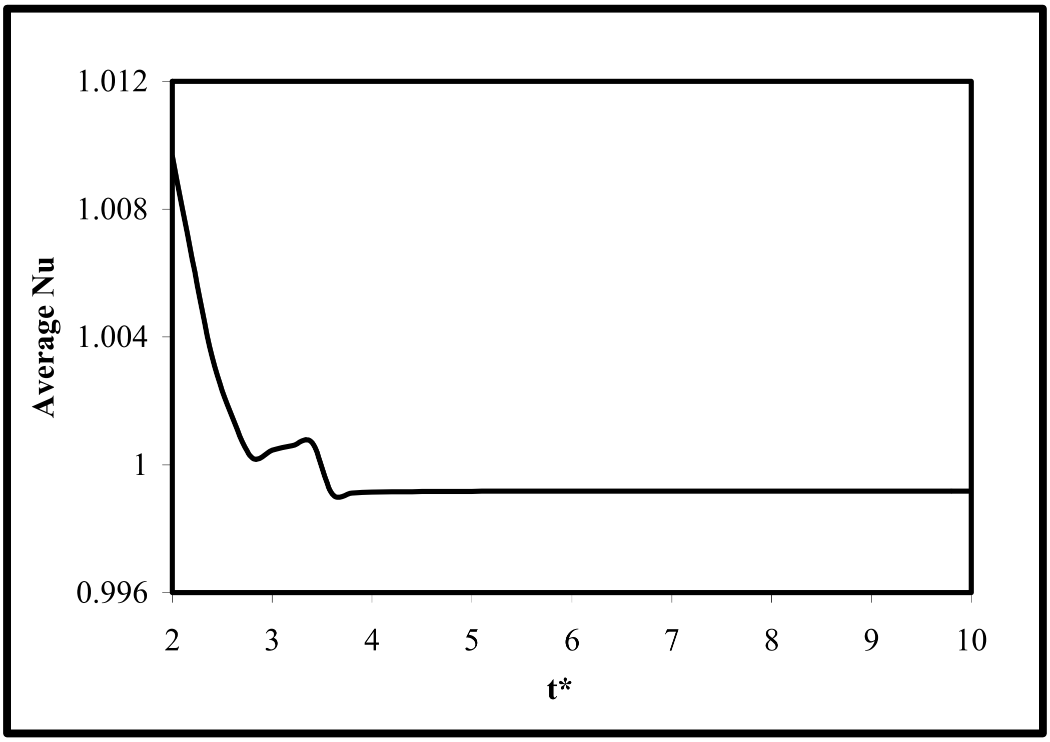

**Figure 5.14.** Average Nu value versus $t^*$ where $Ra\,cos\,\varphi = 1708$ and $\varphi = 30^\circ$

Figure 5.15 demonstrates the variation of local Nu values in the streamwise direction where $Ra\cos\varphi = 10000$ at $\varphi = 30^\circ$. The steady state time shifted from $t^* = 6$ to $t^* = 7$ compared to the same case at $\varphi = 15^\circ$, and also apart from the case at $\varphi = 15^\circ$, local Nusselt numbers do not converge to a constant value, at steady state, instead a periodic oscillation occurs as shown in Figure 5.15 at $t^* = 7$. When Figure 5.6 and Figure 5.15 are compared, it can easily be seen that when the angle of inclination is increased to $30^\circ$, the steady state value of local Nu value in streamwise direction also increases.

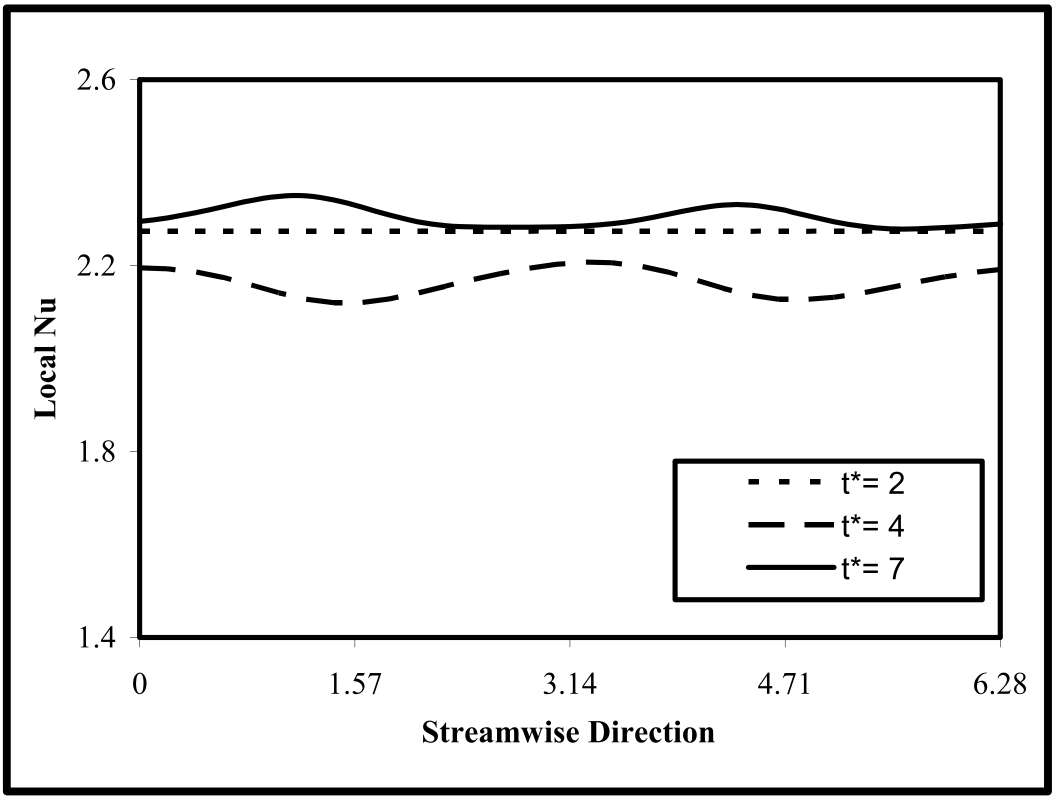

**Figure 5.15**. Local Nu value in streamwise direction where $Ra\cos\varphi = 10000$ and $\varphi = 30^\circ$

Figure 5.16 shows the behavior of local Nu values in the spanwise direction when $Ra\cos\varphi = 10000$ at $\varphi = 30^\circ$. One can easily understand from Figure 5.16 that when time reaches to 6, the steady state is reached. When the same case at $\varphi = 15^\circ$ is analyzed, only one minimum point corresponding to a single pair of convection loop is observed as shown in Figure 5.8 and results change between a larger margin, i.e. between the values of approximately 1 and 3. On the other hand, when the tilt angle is increased to $30^\circ$, two extreme points corresponding to multiple pairs of convection loops as shown in Figure 5.17 are observed within the same time interval in the steady state. Additionally, changes in the results occur in a narrower region. Thus, more periodicity is obtained when the tilt angle is increased.

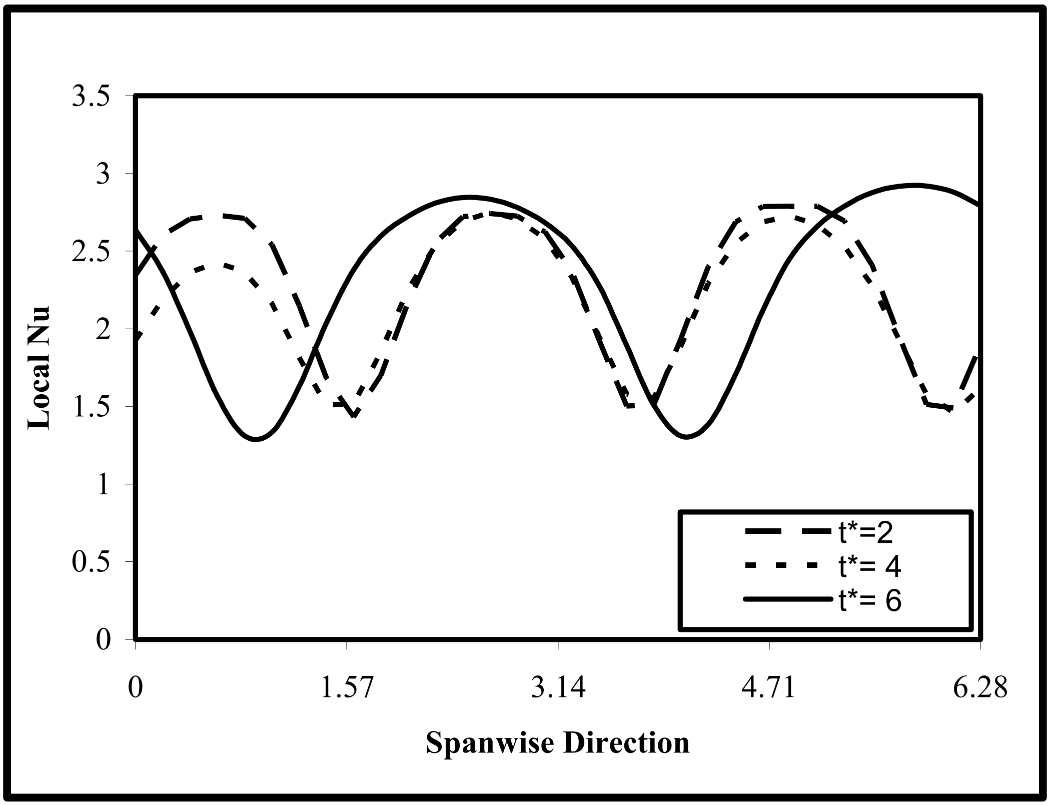

**Figure 5.16**. Local Nu value in spanwise direction where $Ra\cos\varphi = 10000$ and $\varphi = 30^\circ$

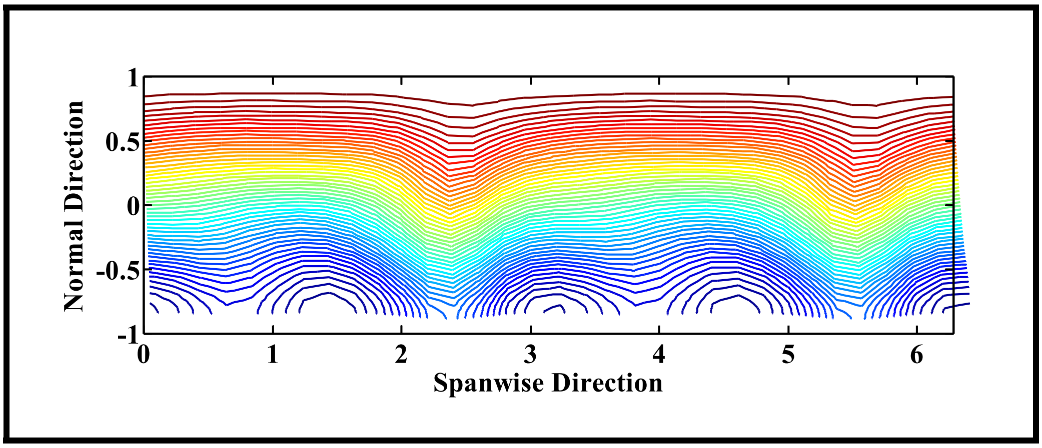

**Figure 5.17.** Streamlines in y-z plane when $Ra\cos\varphi = 10000$ and $\varphi = 30^\circ$ at $t^* = 7$

After analyzing local Nu values, the variation of average Nu with respect to time where $Ra\cos\varphi = 10000$ at $\varphi = 30^\circ$ is shown in Figure 5.18. The results make oscillations between $t^*$ = 2 and $t^*$ = 6 and then reach to a constant value, which is approximately 2.3. This value is slightly larger than the value found when $Ra\cos\varphi = 10000$ at $\varphi = 15^\circ$ that is approximately 2.2. More oscillations before the steady state are observed in Figure 5.18. This can be stemmed from the more periodicity observed especially for the local Nu values in the spanwise direction. This is practically the result of the increase in the angle. Figure 5.19 shows the variation of the average value of Nu with respect to time when $Ra\cos\varphi = 50000$ at $\varphi = 30^\circ$. As mentioned before for the case of $\varphi = 15^\circ$, when $Ra\cos\varphi$ term is increased to 50000, it is too hard to obtain convergence. The same problem exists for the case of $\varphi = 30^\circ$, also. In Figure 5.19, more oscillations in a larger region than the ones in Figure 5.13 are observed, and the local values of this case also change between different values at each time step in a larger region. These results have more oscillations on the average values. In addition to that, the same convergence problem occurred at $\varphi = 45^\circ$ and $\varphi = 60^\circ$. Only the average Nu results for these cases will be introduced with the figures that are constructed for comparison with the literature.

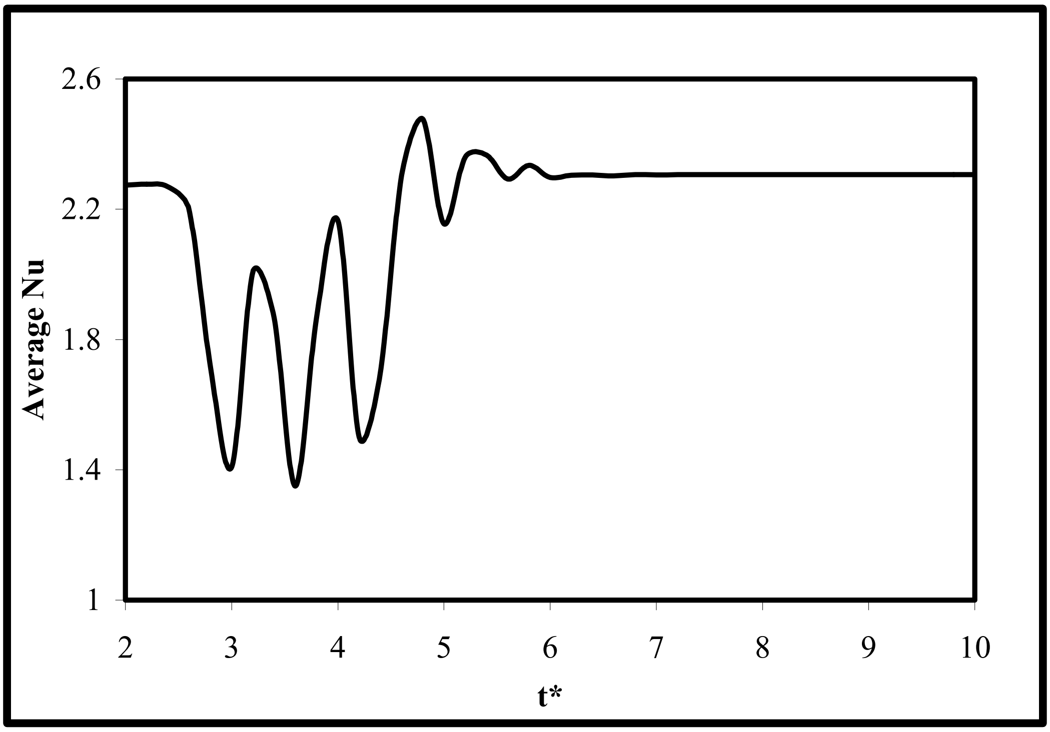

**Figure 5.18**. Average Nu value versus $t^*$ where $Ra\cos\varphi = 10000$ and $\varphi = 30^\circ$

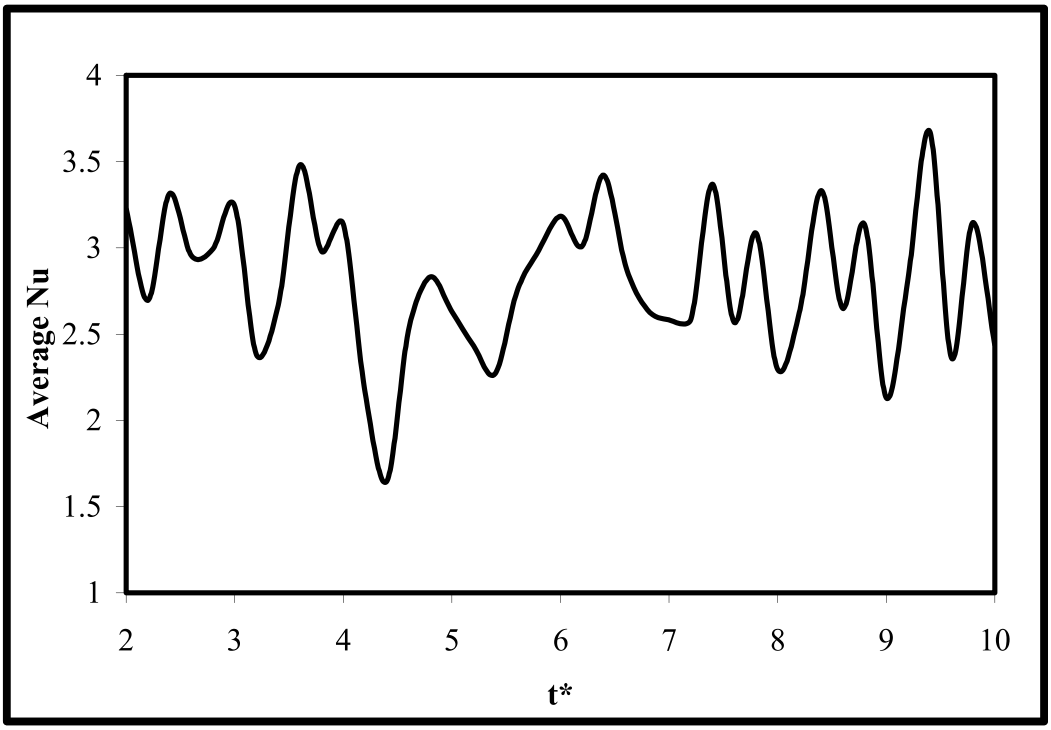

**Figure 5.19.** Average Nu value versus $t^*$ where $Ra\cos\varphi = 50000$ and $\varphi = 30^\circ$

Figures 5.20-21 show the reasons of the more oscillations occurred when $Ra\cos\varphi = 50000$ and $\varphi = 30^\circ$. In Figure 5.20, it can readily be seen that the number of convection loop pairs increases in spanwise direction and the more remarkable observation is in streamwise direction. In Figure 5.21, it is shown that there are longitudinal wavy motions in x direction. This also disturbs the Nu values and makes them oscillate more.

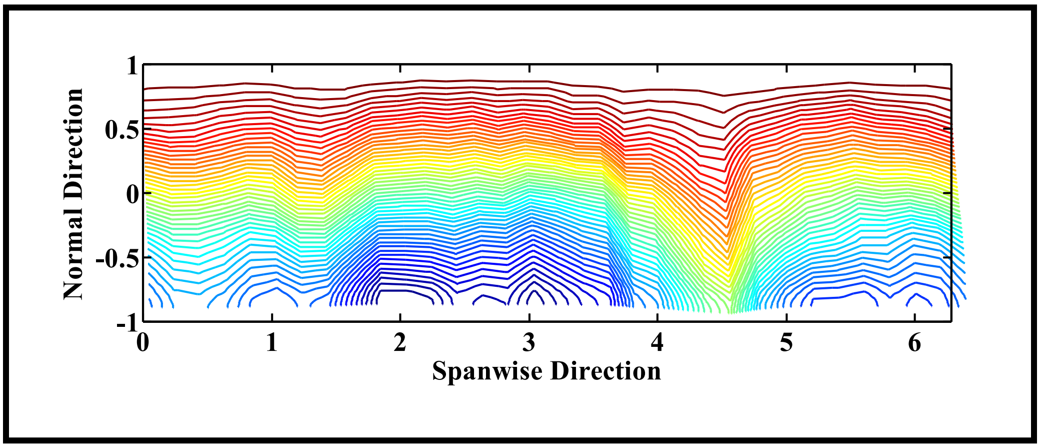

**Figure 5.20.** Streamlines in y-z plane when $Ra\cos\varphi = 50000$ and $\varphi = 30^\circ$ at $t^* = 10$

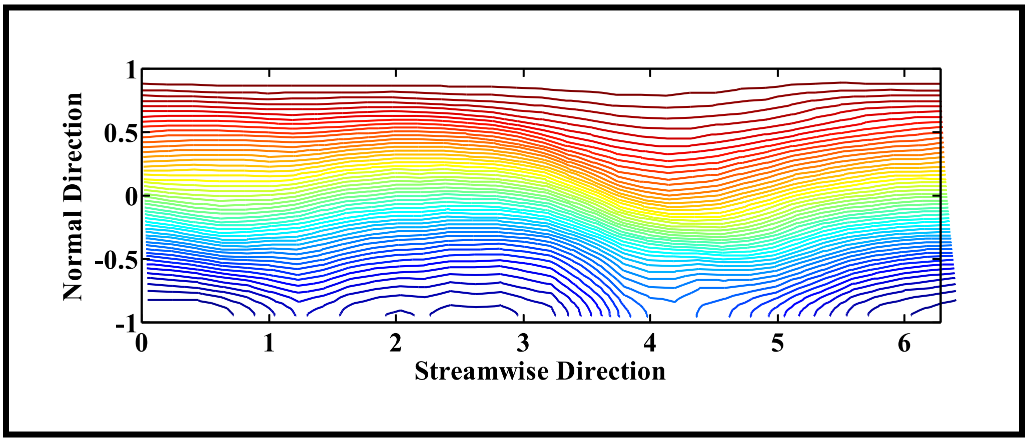

**Figure 5.21.** Streamlines in x-y plane when $Ra\cos\varphi = 50000$ and $\varphi = 30^\circ$ at $t^* = 10$

Figures 5.22-24 show the variation of the dimensionless velocities with respect to time when $Ra\cos\varphi = 1708$ and $\varphi = 15^\circ$. Those figures clearly demonstrate the phenomenon that when $Ra\cos\varphi = 1708$, fluid is in the conductive regime and heat transfer between the inclined plates can only be considered as conduction, since magnitude of the velocities are too low and values of dimensionless $\upsilon$ and $w$ converge to zero. Figures 5.22-24 can also help someone to understand whether the flow reaches to steady state before the determined time or not. The streamwise velocity differs from the other velocities in such a manner that it increases with decreasing gradient then damped to the steady state value but the other ones reach to constant value by damping with some oscillations.

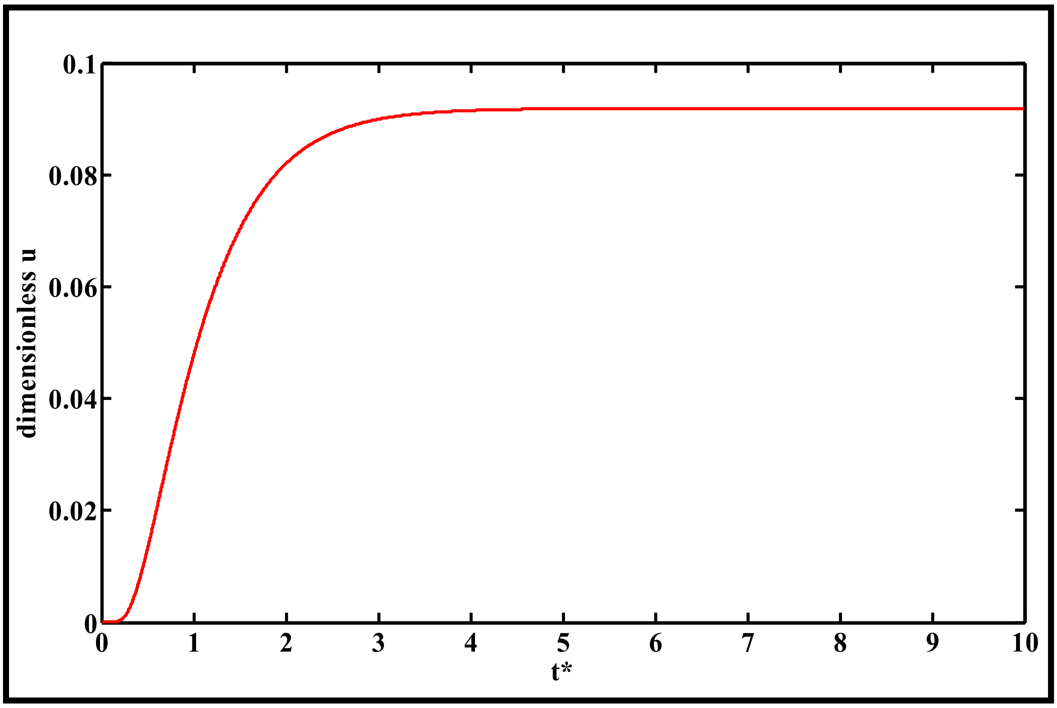

**Figure 5.22.** Dimensionless $u$ versus $t^*$ where $Ra\cos\varphi = 1708$ and $\varphi = 15^\circ$ at [2][2][2]

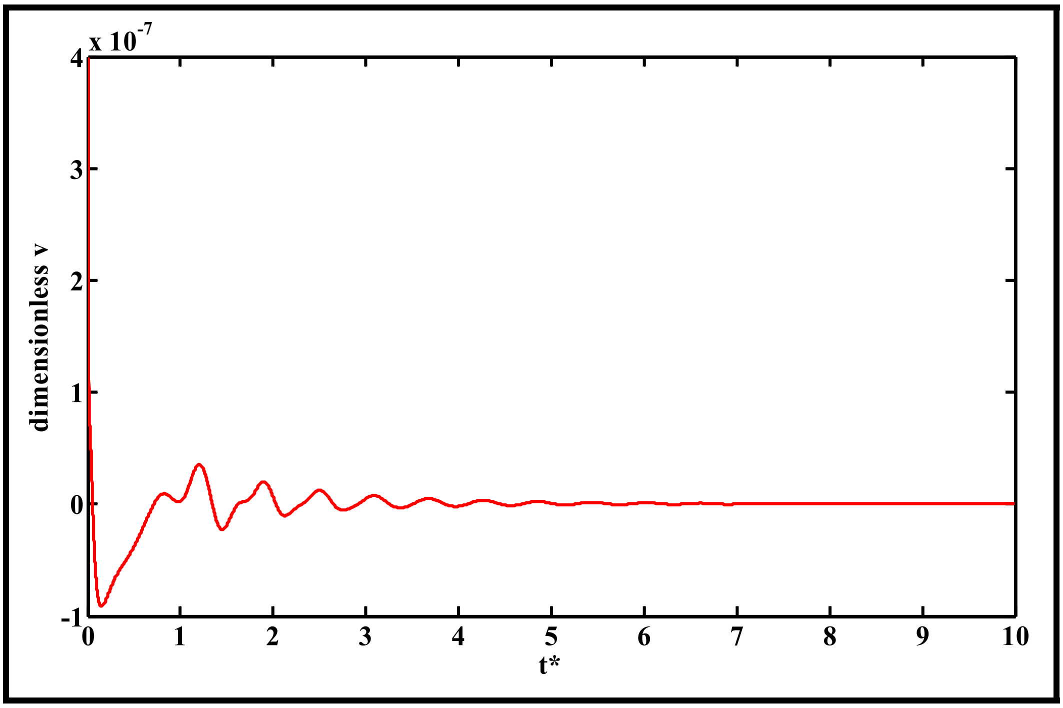

**Figure 5.23**. Dimensionless υ versus $t^*$ where $Ra\cos\varphi = 1708$ and $\varphi = 15^\circ$ at [2][2][2]

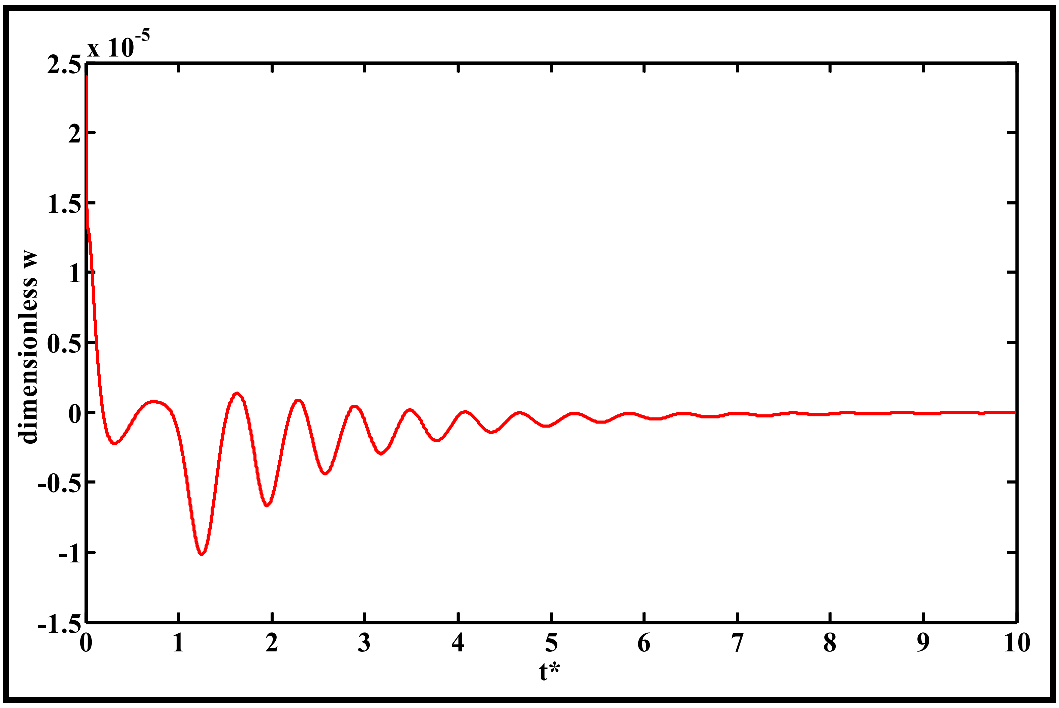

**Figure 5.24**. Dimensionless $w$ versus $t^*$ where $Ra\cos\varphi = 1708$ and $\varphi = 15^\circ$ at [2][2][2]

Figures 5.25-27 demonstrate the variation of the dimensionless velocities with respect to time where $Ra\cos\varphi = 10000$ and $\varphi = 15^\circ$. Apart from the previous $Ra\cos\varphi$, the oscillations become considerable because of the convective motion between the plates. When those figures are examined, it can be easily said that all the velocities increase but the normal velocity is considerably small when compared with the other ones. The steady state characteristics of these figures also differ from the Figures 5.22-24. Approximately after $t^*$ = 5, oscillations start to decrease, and velocities do not reach to constant value instead oscillations become steady. For this reason, local and average Nu values are calculated in this interval.

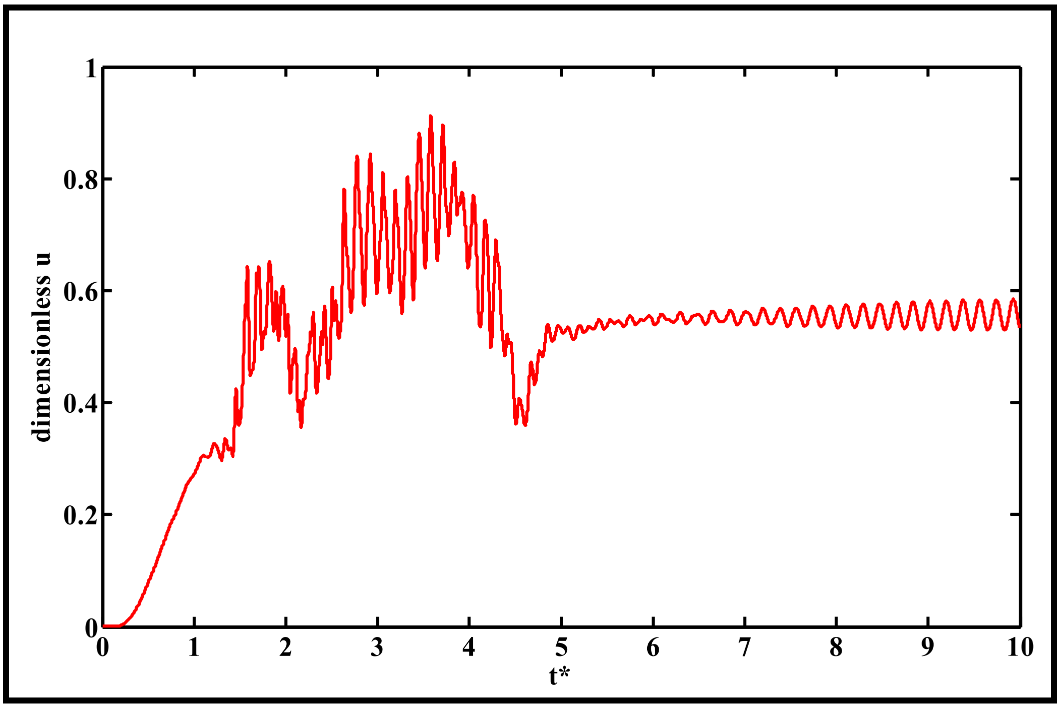

**Figure 5.25**. Dimensionless $u$ versus $t^*$ where $Ra\cos\varphi = 10000$ and $\varphi = 15^\circ$ at [2][2][2]

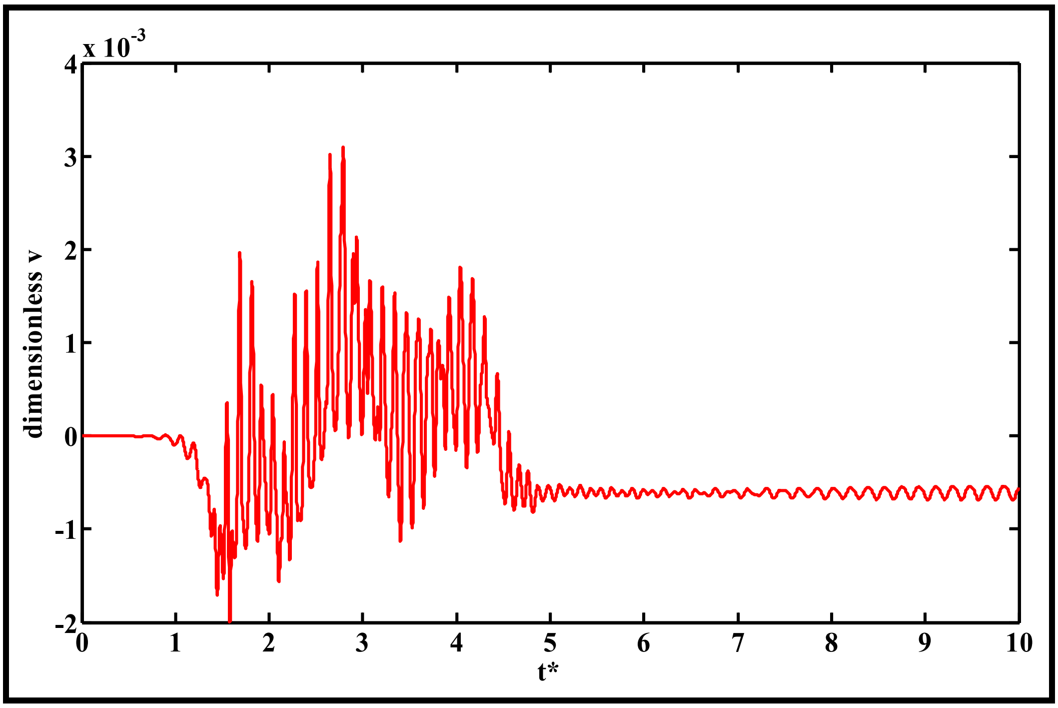

**Figure 5.26**. Dimensionless υ versus $t^*$ where $Ra\cos\varphi = 10000$ and $\varphi = 15^\circ$ at [2][2][2]

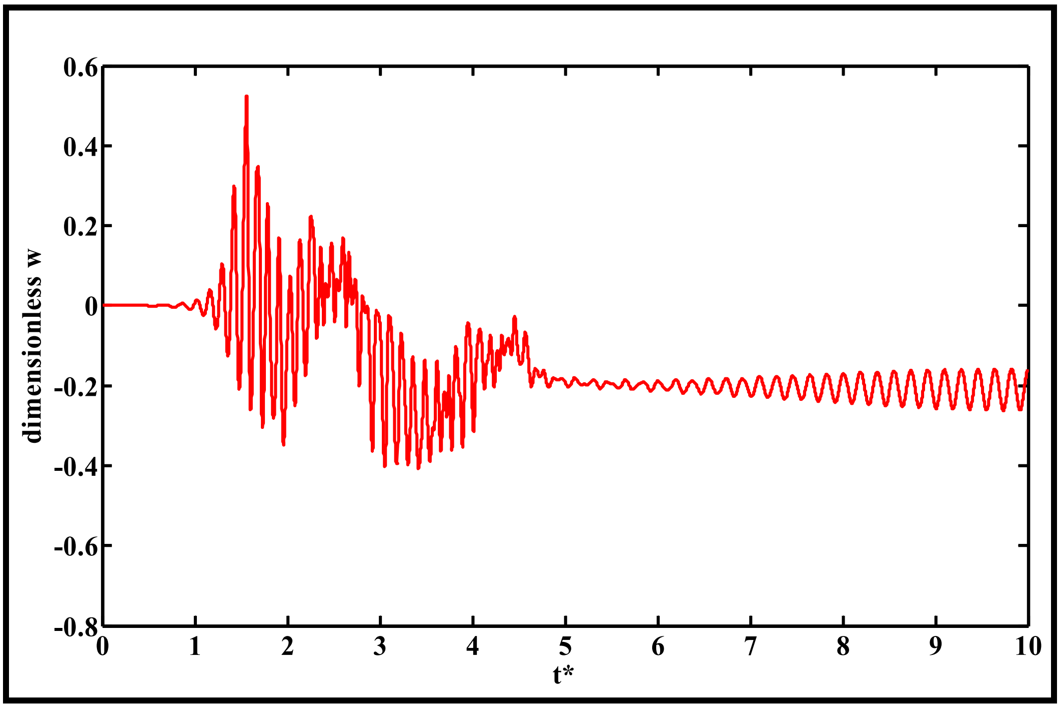

**Figure 5.27**. Dimensionless $w$ versus $t^*$ where $Ra\cos\varphi = 10000$ and $\varphi = 15^\circ$ at [2][2][2]

Figures 5.25-27 show that when the convective heat transfer is taken into consideration, velocities should not be anticipated to reach a constant value, oscillations are the ones that are expected to be steady between the determined time intervals. When the magnitude of the $Ra \cos\varphi$ is increased, the oscillations remarkably increase, and considerable increase in $Ra \cos\varphi$ shifts the time interval where the wavy motions become steady. Figures 5.28-30 directly explain this phenomenon. The inclination angle is kept constant, and $Ra \cos\varphi$ is increased from 10000 to 50000. Results show that steady state is not reached for this case, but since the tilt angle is small, the average Nu values change in a smaller margin as shown in Figure 5.13.

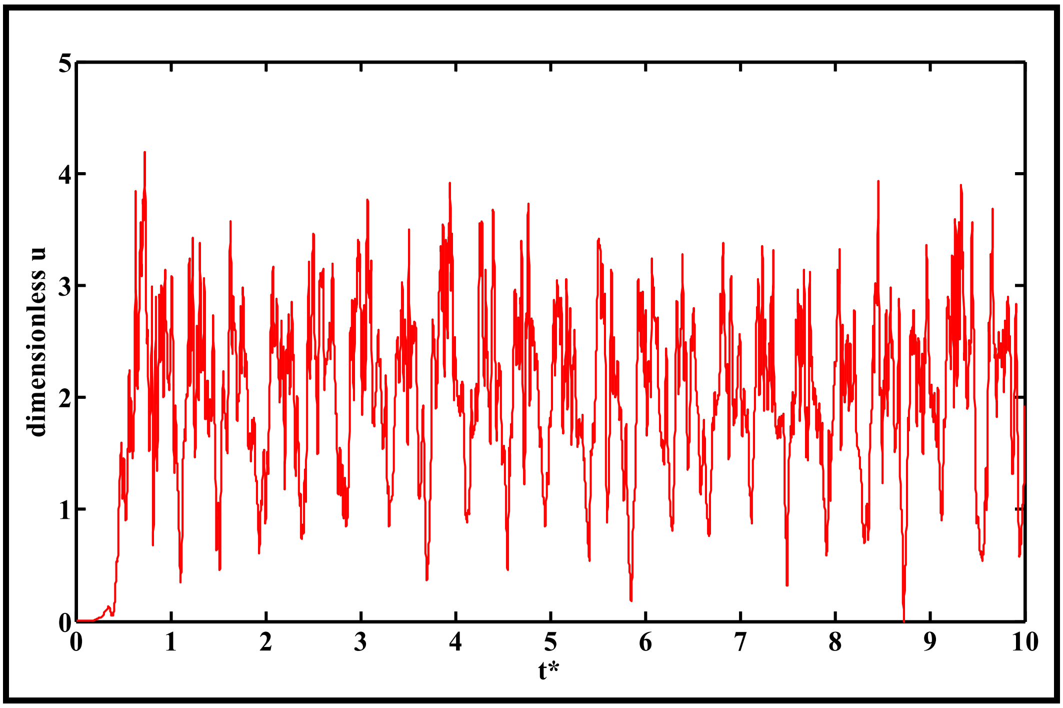

**Figure 5.28**. Dimensionless $u$ versus $t^*$ where $Ra \cos\varphi = 50000$ and $\varphi = 15^\circ$ at [2][2][2]

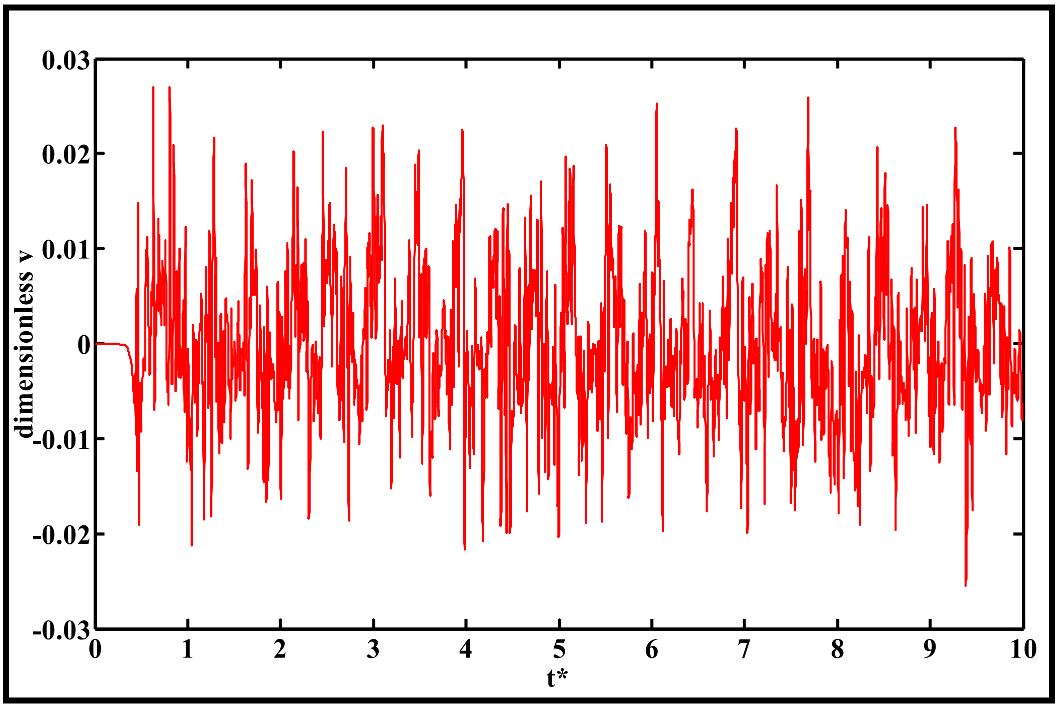

**Figure 5.29**. Dimensionless υ versus $t^*$ where $Ra\cos\varphi = 50000$ and $\varphi = 15^\circ$ at [2][2][2]

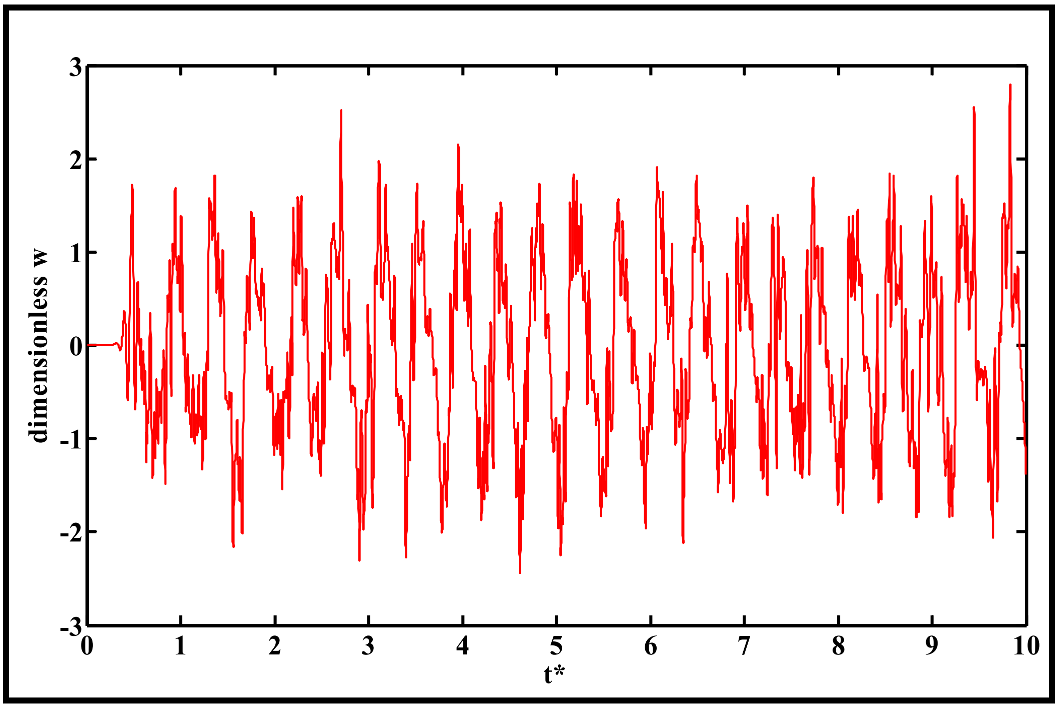

**Figure 5.30**. Dimensionless $w$ versus $t^*$ where $Ra\cos\varphi = 50000$ and $\varphi = 15^\circ$ at [2][2][2]

Apart from the inclination angle, when $Ra\cos\varphi$ is taken equal to or smaller than 1708, only conduction can be observed. For this reason, a greater change in velocity profile is not expected when $\varphi$ is changed. However, Figures 5.31-33 demonstrate a slight change related to the increase in the tilt angle. For example, the magnitude of the streamwise velocity increases, but the trend does not change. Again, spanwise and normal velocities are negligible; however a remarkable observation can be made about them. This is the rapidness of the $\upsilon$ and $w$ values reaching to steady state and meanwhile they make less oscillations than they made when $\varphi = 15^\circ$.

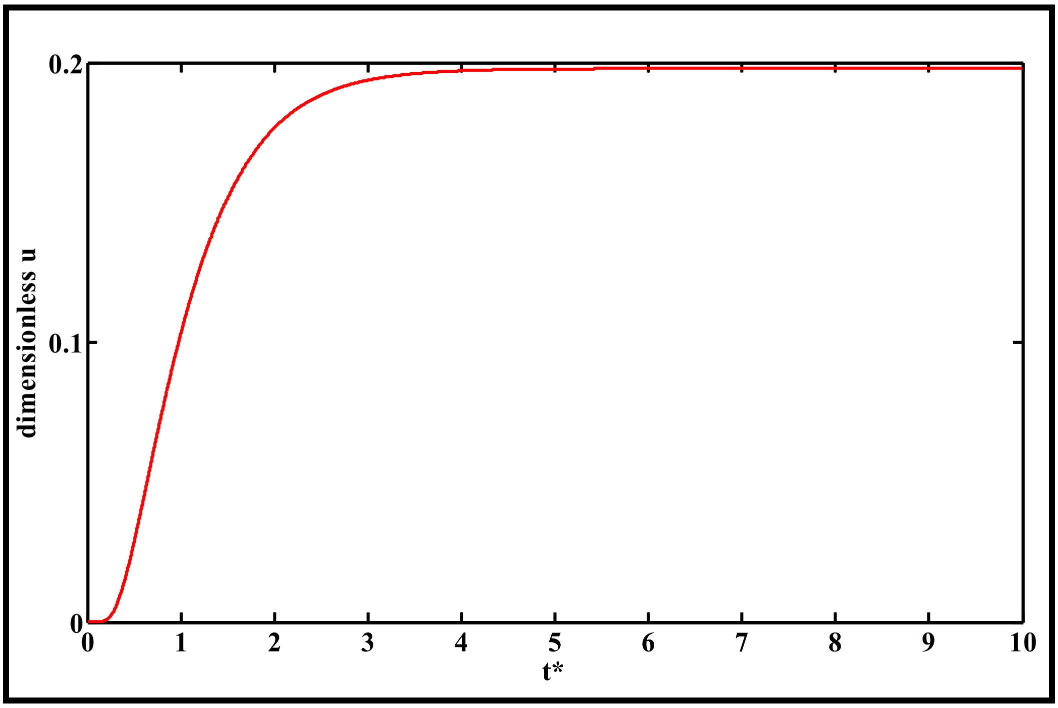

**Figure 5.31**. Dimensionless $u$ versus $t^*$ where $Ra\cos\varphi = 1708$ and $\varphi = 30^\circ$ at [2][2][2]

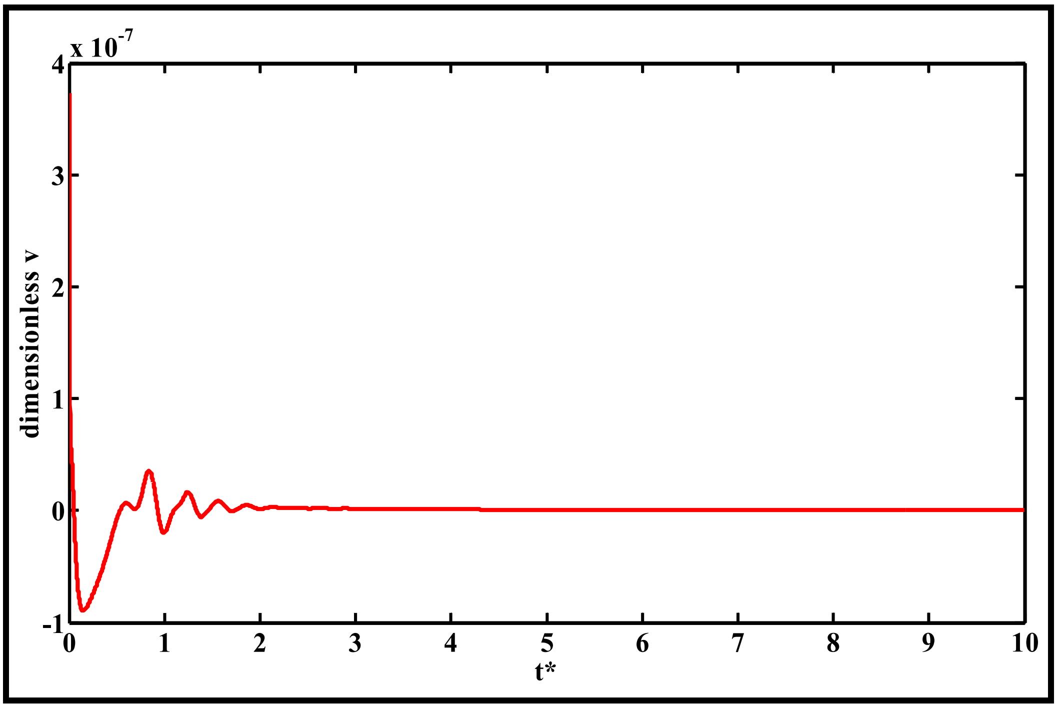

**Figure 5.32**. Dimensionless υ versus $t^*$ where $Ra\cos\varphi = 1708$ and $\varphi = 30^\circ$ at [2][2][2]

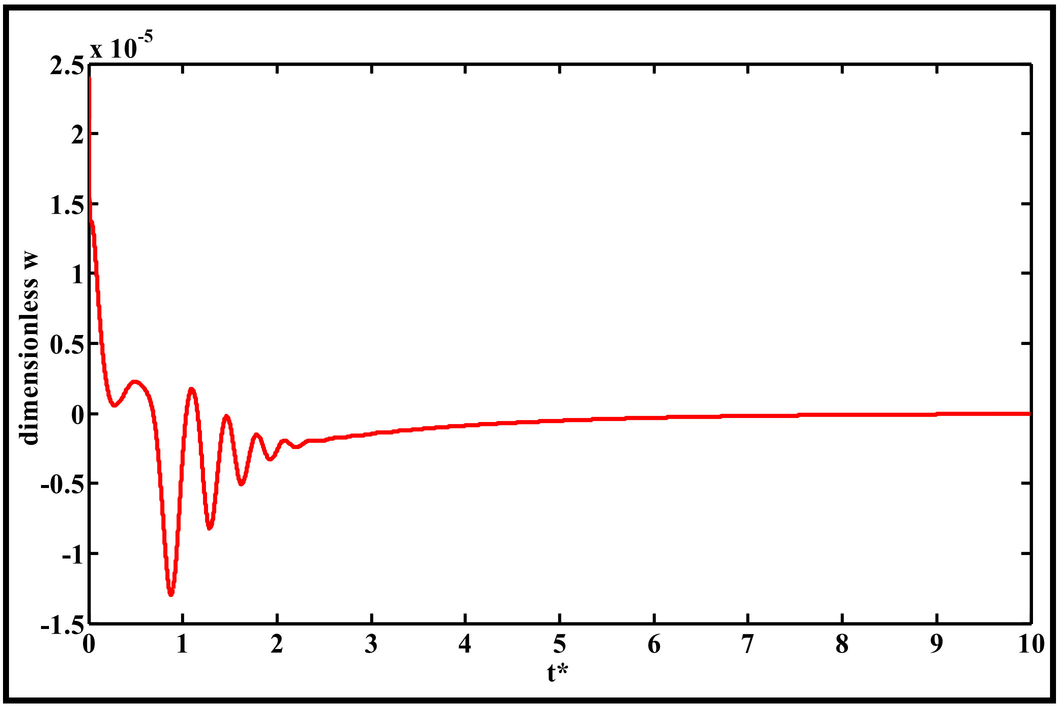

**Figure 5.33**. Dimensionless $w$ versus $t^*$ where $Ra\cos\varphi = 1708$ and $\varphi = 30^\circ$ at [2][2][2]

Figures 5.34-36 show the variation of the dimensionless velocities inside the channel when $Ra\cos\varphi = 10000$ and $\varphi = 30^{\circ}$ **.** It can easily be noticed that oscillations become steady, but the results of especially the $\upsilon$ and $w$ oscillate between larger margins. These oscillations are the indications of oscillating convective loop structures. This is the main effect of increasing the angle of inclination. On the other hand, approximately, $t^*$ = 6 is the onset of the time periodicity of oscillations for both of the tilt angles $15^{\circ}$ and $30^{\circ}$ . Another difference from the case of $\varphi = 15^{\circ}$ is the change in the magnitude of the velocities. When the tilt angle increases, they increase also. All changes before $t^*$ = 6, first increasing and then decreasing trend of the graph can be explained by the numerical method that is being used. Thus, they try to converge. This is the main reason why Nu values oscillate in a similar way before they converge.

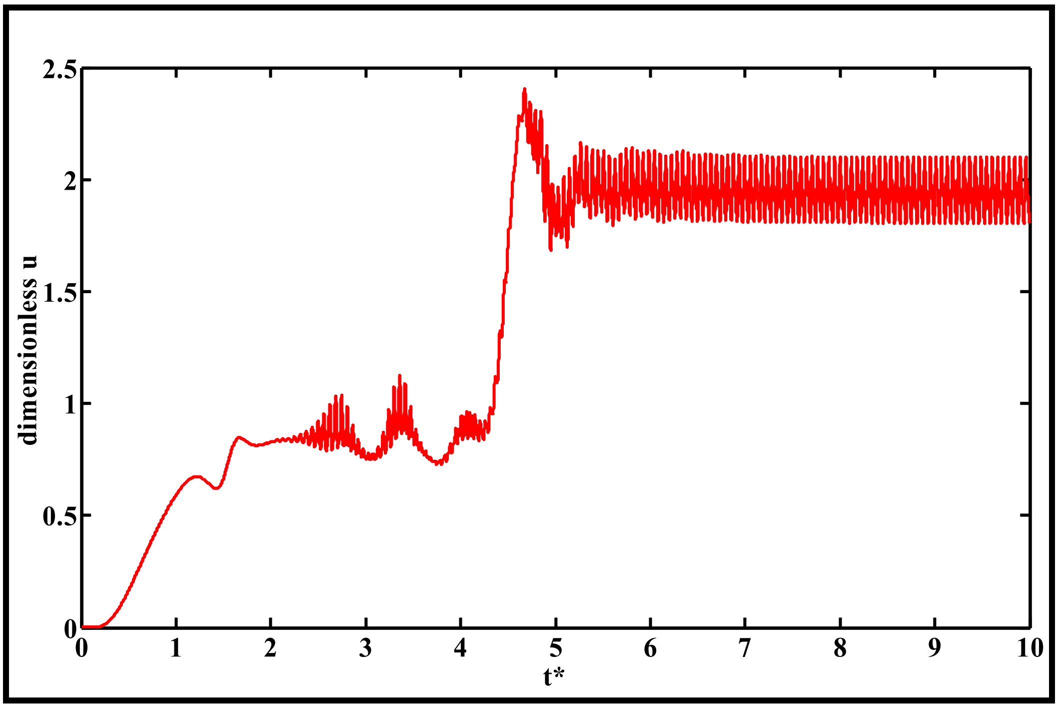

**Figure 5.34**. Dimensionless $u$ versus $t^*$ where $Ra\cos\varphi = 10000$ and $\varphi = 30^{\circ}$ at [2][2][2]

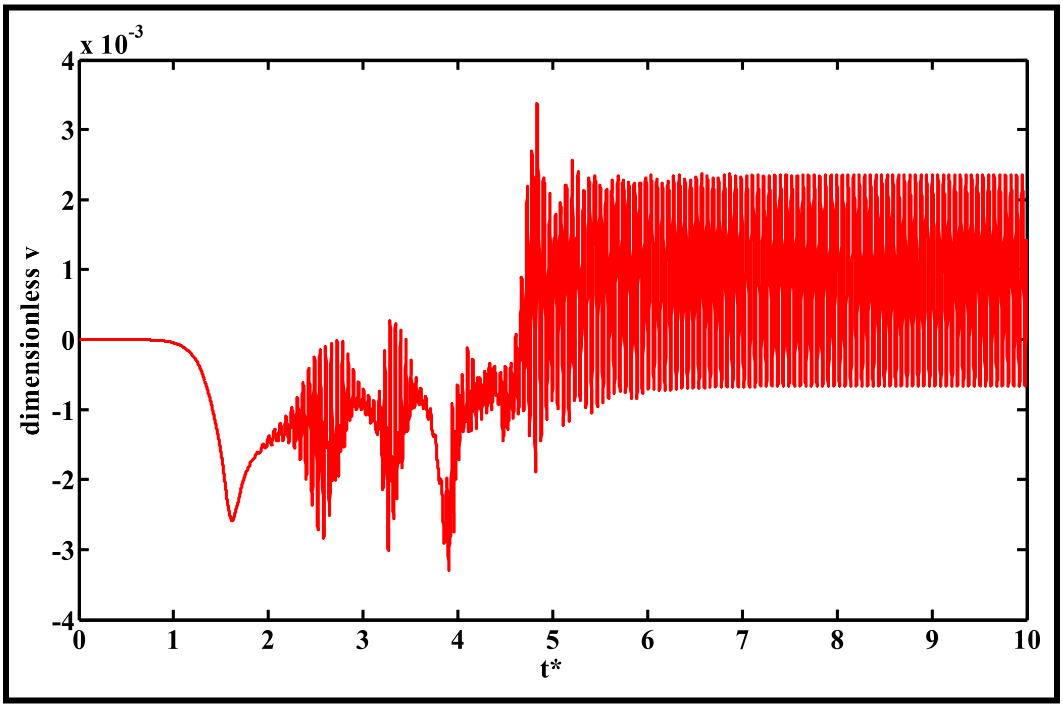

**Figure 5.35**. Dimensionless υ versus $t^*$ where $Ra\cos\varphi = 10000$ and $\varphi = 30^\circ$ at [2][2][2]

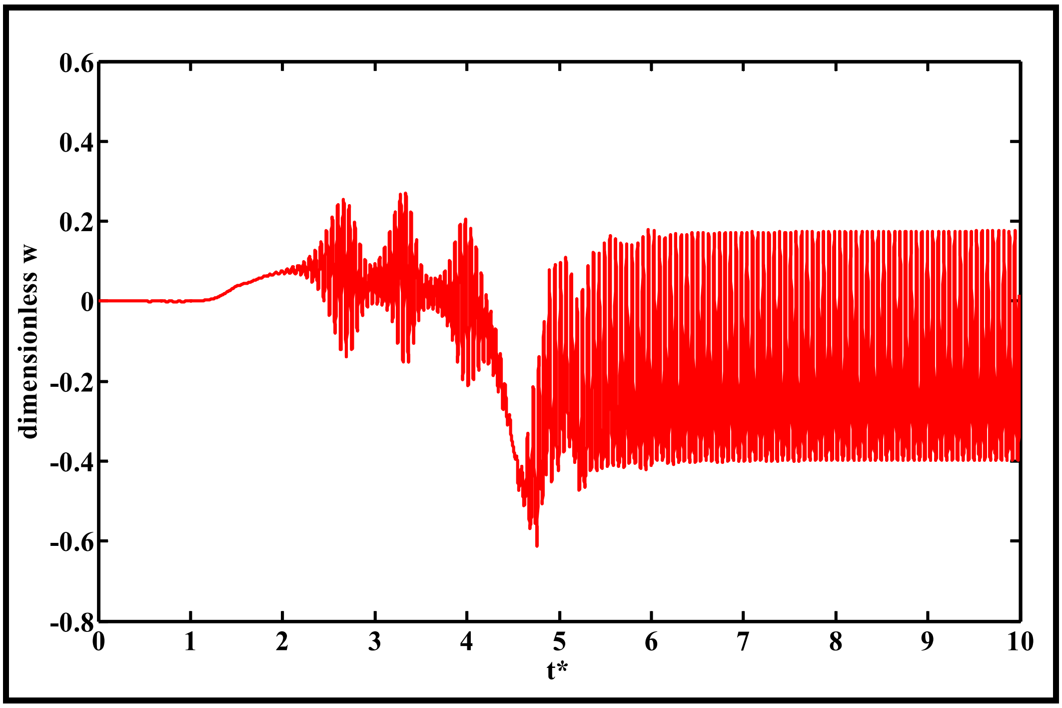

**Figure 5.36**. Dimensionless $w$ versus $t^*$ where $Ra\cos\varphi = 10000$ and $\varphi = 30^\circ$ at [2][2][2]

Figures 5.37-39 show the variation of the non-dimensional velocities when $Ra\cos\varphi = 50000$ and $\varphi = 30^\circ$. It can easily be concluded that when $Ra\cos\varphi$ reaches to 50000, whatever the angle of inclination, time interval between $t^*$ = 2 and $t^*$ = 10 is not adequate for the flow to reach convergence and the oscillations become more often. Another observation is that the orders of magnitude of velocity oscillations increase considerably. This problem is the main drawback that is encountered in this study and in order to reach convergence for these higher values of $Ra\cos\varphi$, the time increment should be reduced; at the same time, time end should be enlarged. The same problem is also confronted when $\varphi = 45^\circ$ and $\varphi = 60^\circ$. For this reason, the results of these angles are not examined in detail like they are done for $\varphi = 15^\circ$ and $\varphi = 30^\circ$. Moreover, the value of $Ra\cos\varphi$ for the onset of those greater and more frequent oscillations shifts to 10000 when $\varphi = 45^\circ$ and $\varphi = 60^\circ$.

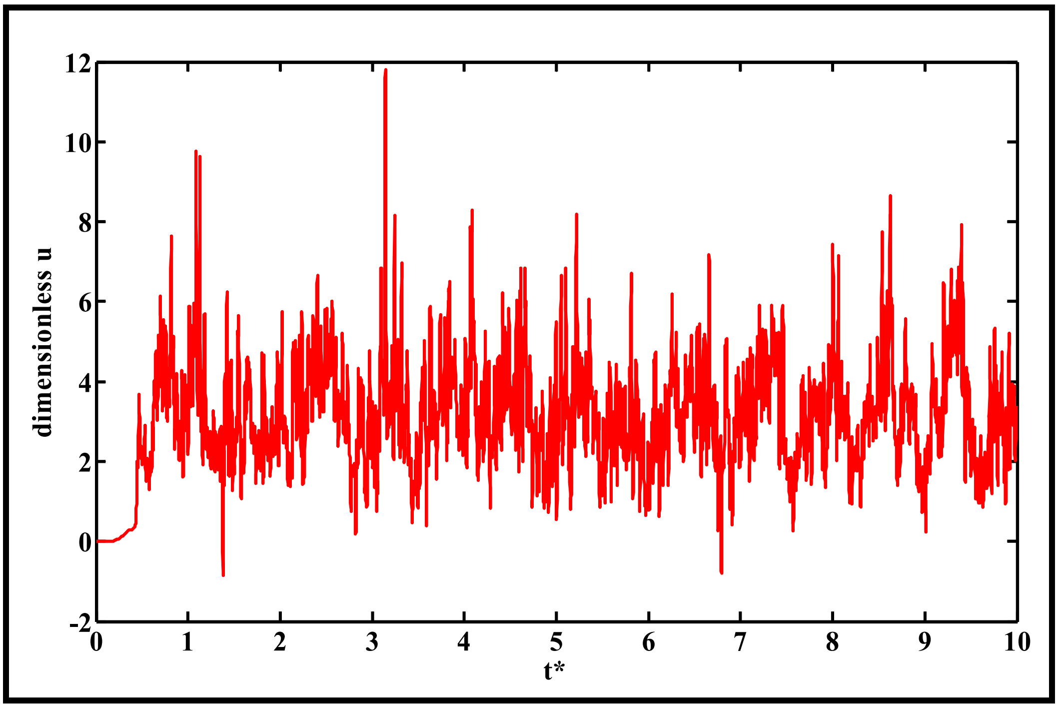

**Figure 5.37**. Dimensionless $u$ versus $t^*$ where $Ra\cos\varphi = 50000$ and $\varphi = 30^\circ$ at [2][2][2]

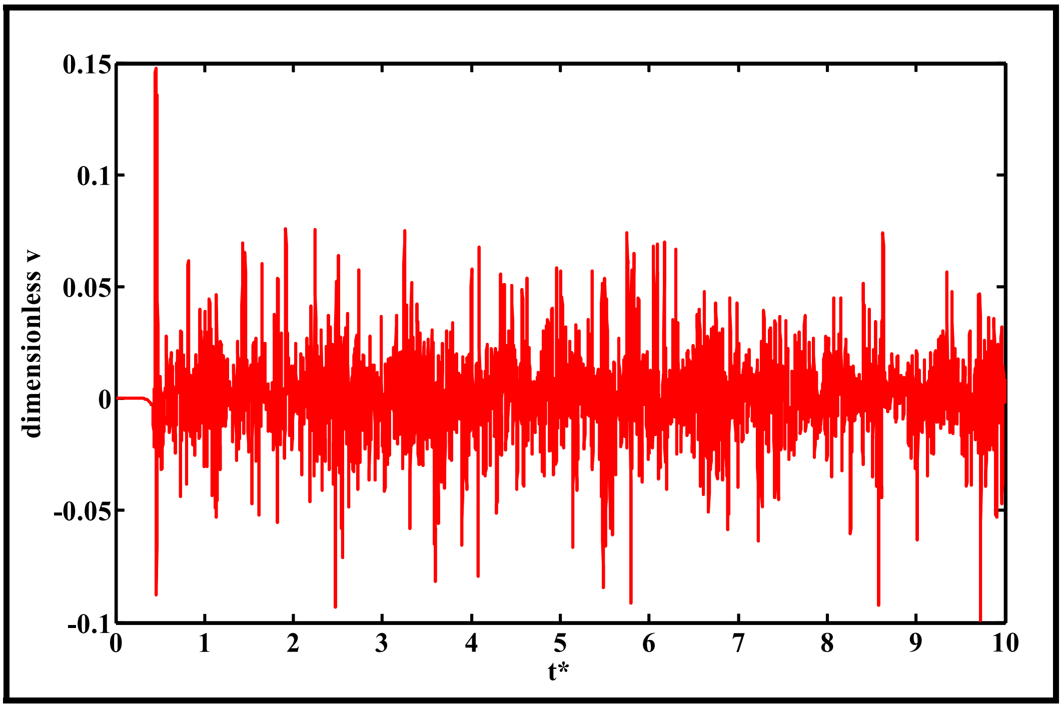

**Figure 5.38**. Dimensionless υ versus $t^*$ where $Ra\cos\varphi = 50000$ and $\varphi = 30^\circ$ at [2][2][2]

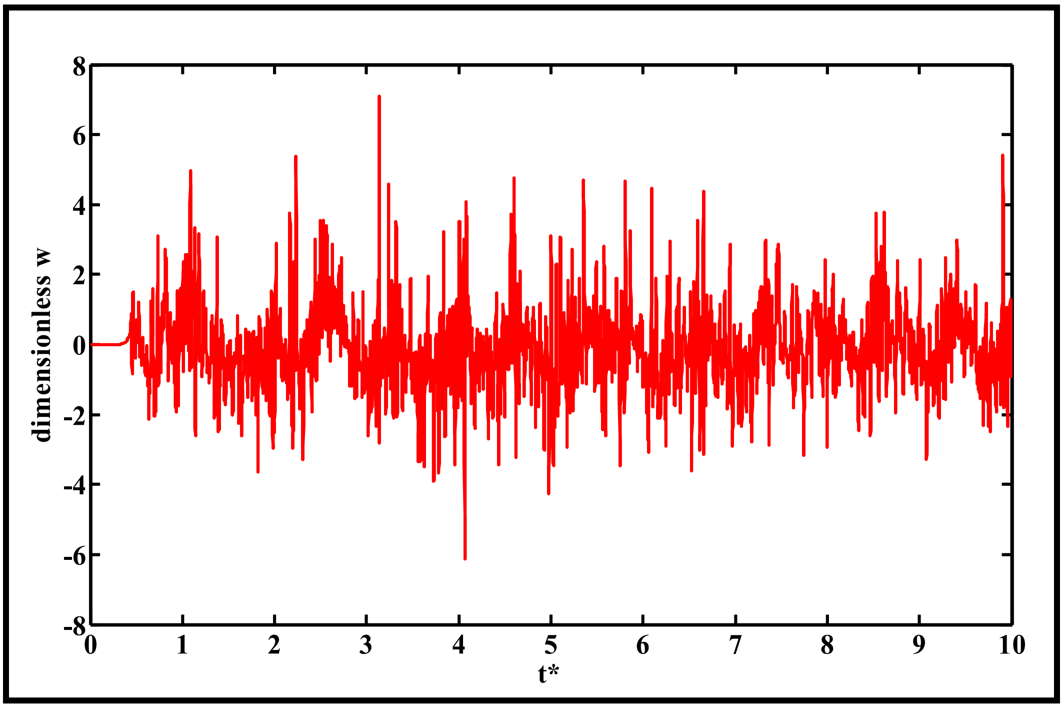

**Figure 5.39**. Dimensionless $w$ versus $t^*$ where $Ra\cos\varphi = 50000$ and $\varphi = 30^\circ$ at [2][2][2]

Figure 5.40 shows the variation of average Nu with respect to $Ra\cos\varphi$ when $\varphi = 15^\circ$. The results are compared with Hollands' et. al [4] experimental study. As it is mentioned before, in the experimental study two correlations are used. The results are plotted with the results of these correlations. The values of $Ra\cos\varphi$, which are $1708, 10000, 20000$ and $50000$, are compared with the literature work. Because, the computational time is too long for each case, the extend of the results are somewhat restricted. It can be readily noticed that values of the present study are very close to the values of both correlations at the specified $Ra\cos\varphi$. The maximum deviation of the results is approximately eight percent from the results of Eqn. 5.9 at $Ra\cos\varphi = 20000$.

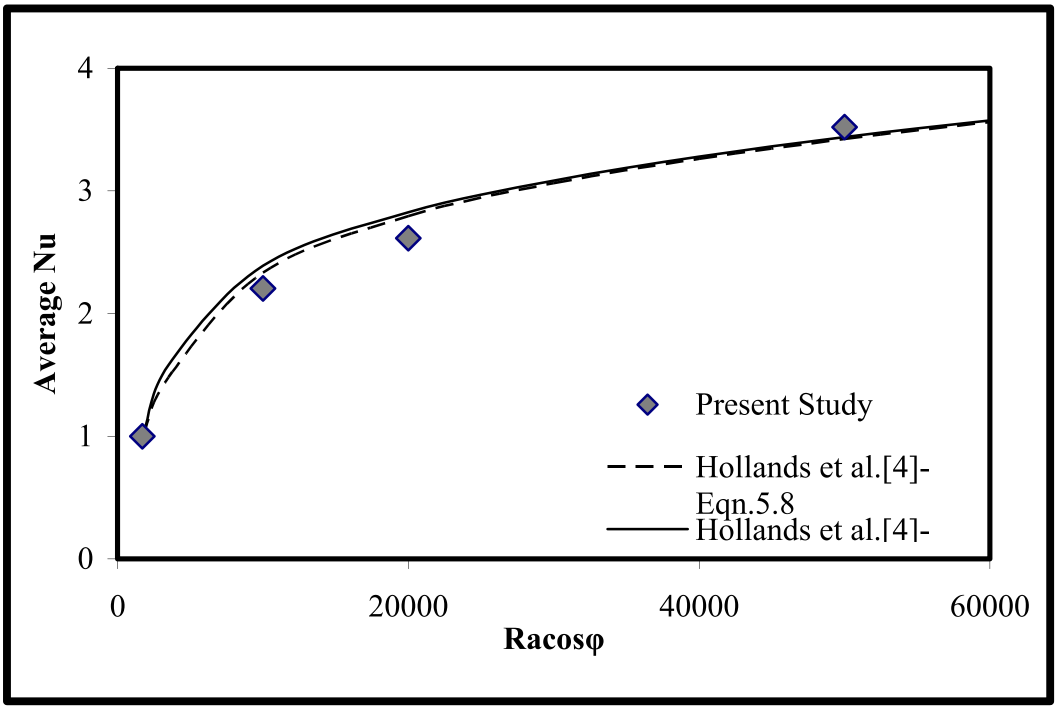

**Figure 5.40**. Average Nu versus $Ra\cos\varphi$ where $\varphi = 15^\circ$

Figure 5.41 illustrates the variation of average Nu with respect to $Ra\,cos\,\varphi$ when $\varphi = 30^{\circ}$. The present study value is smaller than both of the correlations' values at $Ra\,cos\,\varphi = 10000$ at $\varphi = 15^{\circ}$, however in this case result of this study is between the results of two correlations. On the other hand, the relative percentage error for $Ra\,cos\,\varphi = 20000$ at $\varphi = 30^{\circ}$ is greater than the relative percentage error for the same $Ra\,cos\,\varphi$ at $\varphi = 15^{\circ}$. Additionally, since the convergence is not obtained at $Ra\,cos\,\varphi = 50000$ for the present study, the deviations from the two correlations are considerable about 18 percent. On Figure 5.40, for $\varphi = 15^{\circ}$, the result at $Ra\,cos\,\varphi = 50000$ is not a converged value but since the inclination angle is low, deviation is not very large.

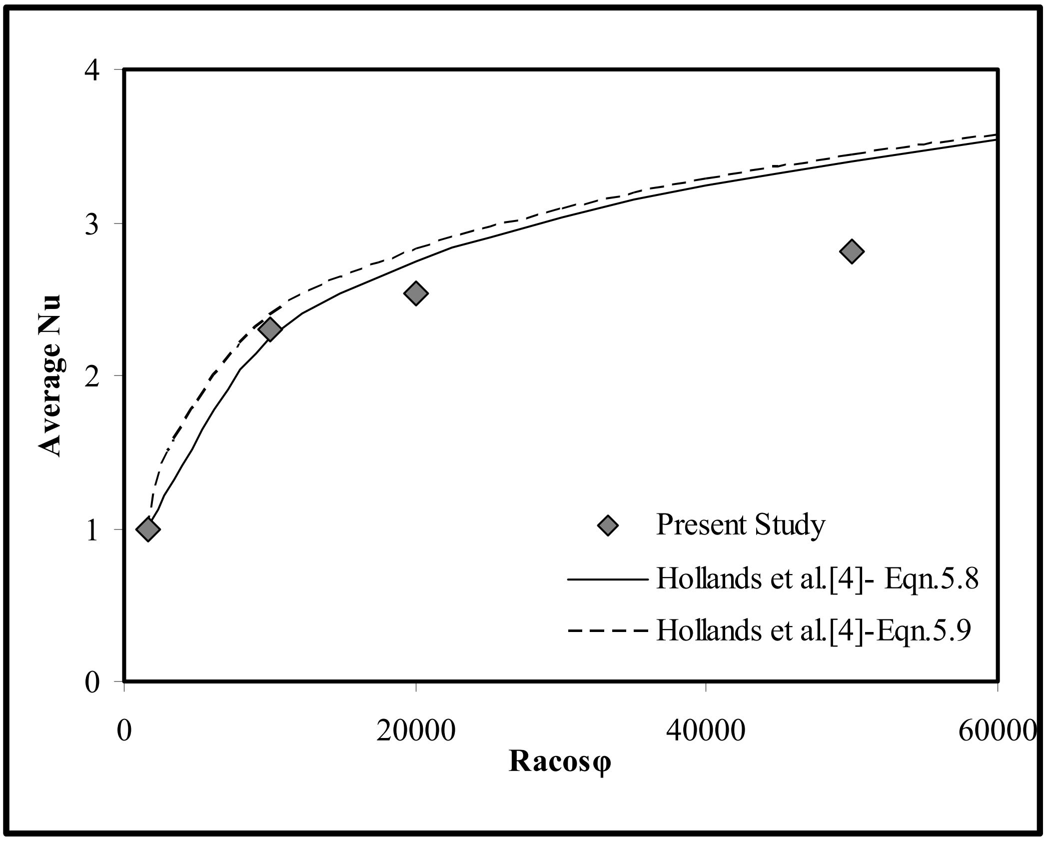

**Figure 5.41**. Average Nu versus $Ra\,cos\,\varphi$ where $\varphi = 30^{\circ}$

Figure 5.42 shows the variation of average Nu with respect to $Ra\,cos\,\varphi$ when $\varphi = 45^\circ$. As it can also easily be seen from the figure that when $Ra\,cos\,\varphi$ reaches to 20000, and 50000, the values of average Nu deviates considerably from the values of Eqns. 5.8-9. The main reason for that is that the results of the program do not converge within the specified time interval. For the cases of $\varphi = 30^\circ$, $\varphi = 45^\circ$ and $\varphi = 60^\circ$, when $Ra\,cos\,\varphi = 50000$ time increment is decreased within the specified interval, the expected improvement in Nu is not achieved. When $Ra\,cos\,\varphi = 50000$, Nu deviates about 32 and 33 percent from the Eqns. 5.8 and 5.9, respectively.

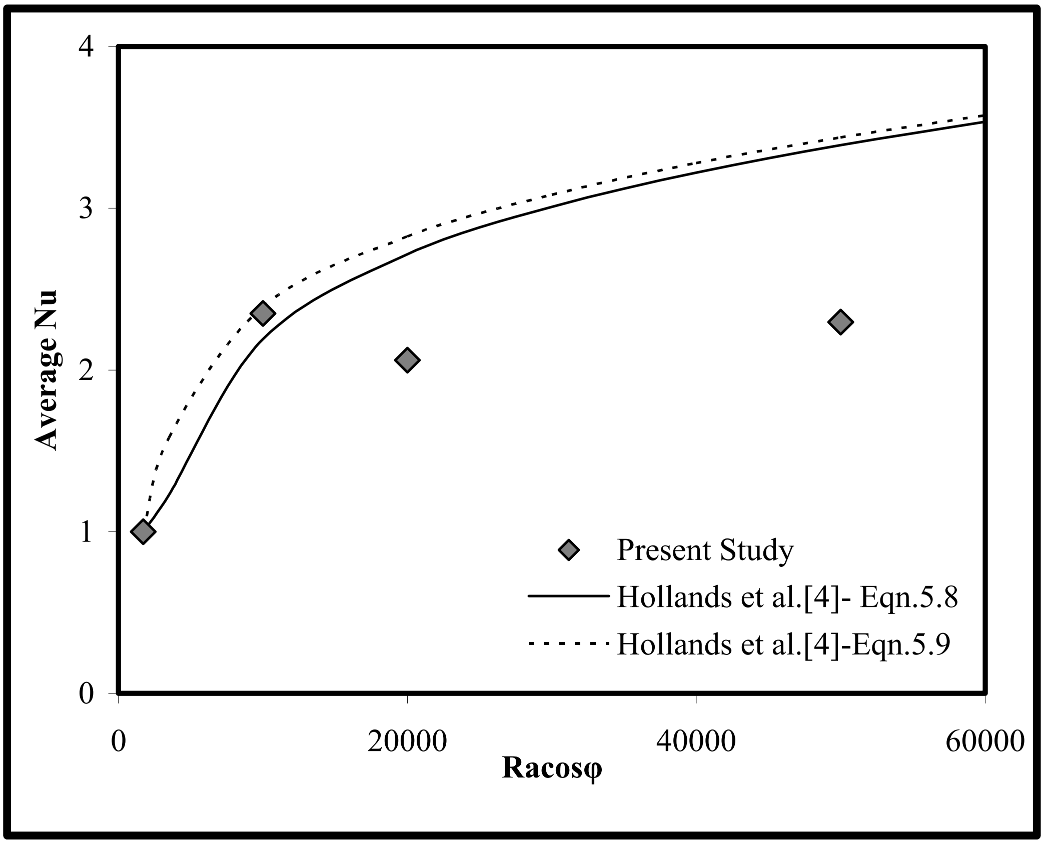

**Figure 5.42.** Average Nu versus $Ra\,cos\,\varphi$ where $\varphi = 45^\circ$

Figure 5.43 illustrates the trend of the average Nu with respect to $Ra\,cos\,\varphi$ when $\varphi = 60^\circ$. Apart from the inclinations of $\varphi = 15^\circ$, $\varphi = 30^\circ$, and $\varphi = 45^\circ$, additionally $Ra\,cos\,\varphi = 3500$ is analyzed at $\varphi = 60^\circ$. The average Nu value for $Ra\,cos\,\varphi = 3500$ is closer to the value of Eqn. 5.9. When Figure 5.43 is compared with the Figure 5.42, it can easily be realized that the value of Nu at $Ra\,cos\,\varphi = 50000$ does not deviate in a decreasing trend after the value at $Ra\,cos\,\varphi = 10000$. Moreover it follows the same trend as it does in Eqns. 5.8-9. However, convergence is not achieved again for the values of $Ra\,cos\,\varphi = 10000$ and $Ra\,cos\,\varphi = 50000$ between $t^* = 2$ and $t^* = 10$. For this reason, the relative error between the correlations and the present study is between 22-28 percent.

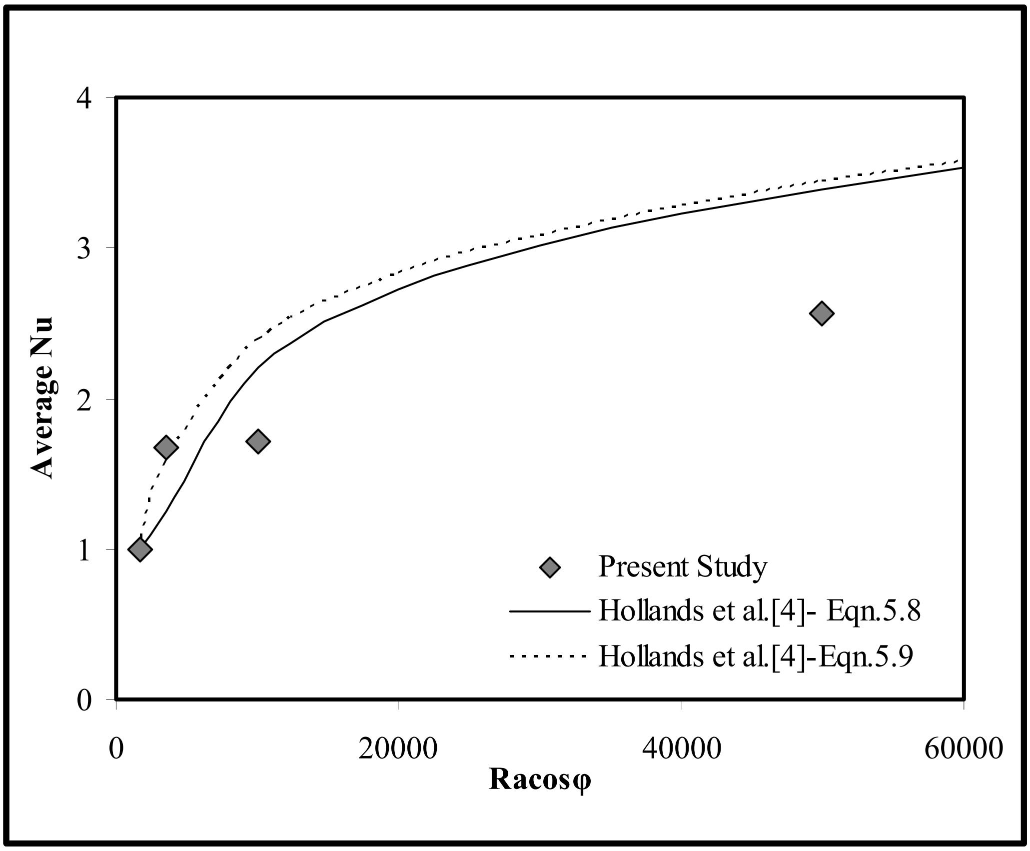

**Figure 5.43.** Average Nu versus $Ra\,cos\,\varphi$ where $\varphi = 60^\circ$

Table 5.1 presents the numerical values of Nu and the relative percentage errors in a tabular way. All the Nusselt numbers tabulated here are average values and percentage errors are calculated with respect to the values of Eqns. 5.8-9. It can again easily be seen from Table 5.1 that error values increase considerably for $Ra\,cos\,\varphi = 50000$ at $\varphi = 30^\circ - 60^\circ$ ; on the other hand for $\varphi = 60^\circ$ , Nu values deviate in a large amount also at $Ra\,cos\,\varphi = 10000$ .

**Table 5.2.** Average Nu Values of Present Study with Eqns. 5.8-9 and Relative Percentage Error Values of Present Study with respect to Eqns. 5.8-9

| φ(deg) | Racosφ | Present Study | Eqn. 5.8 | Eqn. 5.9 | Error (%) Eqn. 5.8 | Error (%) Eqn. 5.9 |
|---|---|---|---|---|---|---|
| 15 | 1708 | 0.999 | 1.000 | 1.000 | 0 | 0 |
| | 10000 | 2.205 | 2.333 | 2.391 | 6 | 8 |
| | 20000 | 2.616 | 2.793 | 2.825 | 6 | 7 |
| | 50000 | 3.520 | 3.424 | 3.438 | 3 | 2 |
| 30 | 1708 | 0.999 | 1.000 | 1.000 | 0 | 0 |
| | 10000 | 2.306 | 2.246 | 2.391 | 3 | 4 |
| | 20000 | 2.532 | 2.745 | 2.825 | 8 | 10 |
| | 50000 | 2.811 | 3.404 | 3.438 | 17 | 18 |
| 45 | 1708 | 0.999 | 1.000 | 1.000 | 0 | 0 |
| | 10000 | 2.349 | 2.191 | 2.391 | 7 | 2 |
| | 20000 | 2.061 | 2.715 | 2.825 | 24 | 27 |
| | 50000 | 2.296 | 3.391 | 3.438 | 32 | 33 |
| 60 | 1708 | 0.999 | 1.000 | 1.000 | 0 | 0 |
| | 3500 | 1.678 | 1.249 | 1.581 | 34 | 6 |
| | 10000 | 1.711 | 2.203 | 2.391 | 22 | 28 |
| | 50000 | 2.567 | 3.394 | 3.438 | 24 | 25 |

## 5.6. Analysis of a Sample Case with a Finer Grid (64 x 128 x 64)

In the previous section, local Nusselt numbers at x and z directions and the average values of them at four different inclination angles for four $Ra\cos\varphi$ values are illustrated. Besides them, non-dimensional streamwise, normal and spanwise velocities for $\varphi = 15^\circ - 30^\circ$ are also shown. While doing this, 32 x 64 x 32 grid arrangement is used. In this section, a finer grid is used to understand whether the results are grid dependent or not. For this purpose, 64 x 128 x 64 grid arrangement and the case of $Ra\cos\varphi = 10000$ at $\varphi = 15^\circ$ are preferred in order to reach the steady state and get the results more rapidly. Since the number of collocation points are doubled in all three directions, to get the results takes six times longer than the coarser grid arrangement case. Also the same case is investigated using a coarser $16 \times 32 \times 16$ grid arrangement. The average Nu values for three grid arrangements for the specified case are tabulated in Table 5.3.

**Table 5.3.** Average Nu Values for three grid arrangements

| Grid Arrangements | Average Nu Values |
|---|---|
| $16 \times 32 \times 16$ | 2.201 |
| $32 \times 64 \times 32$ | 2.205 |
| $64 \times 128 \times 64$ | 2.392 |

Figures 5.44-46 show the variations of local Nu in streamwise and spanwise directions, and the average Nu values with respect to non-dimensional time when $Ra\cos\varphi = 10000$ and $\varphi = 15^\circ$ with $64 \times 128 \times 64$ grid arrangement. In Figure 5.44, after $t^* = 7$ steady state is reached and apart from the coarser grid arrangement, the results reach a periodic steady state motion. In that motion, Nu values make a periodic fluctuation by starting from the expected value and then going down to a minimum finally increasing to the starting value. In Figure 5.45, steady state point is when $t^* = 6$ . Likewise in $32 \times 64 \times 32$ grid arrangement, results converge to a steady wave-like motion.

The differences between the both grid arrangements are the amplitudes of the fluctuations and the steady state values. Figure 5.46 illustrates the variation of the average Nu values with respect to dimensionless time. Contrary to the coarser grid arrangement results, the results start to oscillate from a higher value and reach a higher steady state value. Even though the initial behavior of the graph is in a narrower region, a constant value is reached after about same $t^*$ value. Average Nu values in present study when $Ra\cos\varphi = 10000$ at $\varphi = 15^\circ$ for $32 \times 64 \times 32$ and $64 \times 128 \times 64$ arrangements are 2.205 and 2.392, respectively. After observing this difference between the average Nu values of two grid arrangement, it is decided to run the program with grid arrangement of $16 \times 32 \times 16$. Results are very similar with the ones of $32 \times 64 \times 32$ grid arrangement as shown in Table 5.2. In addition to that, relative percentage errors decrease with finer grids but since errors occurred in coarser grids are in an acceptable range, $32 \times 64 \times 32$ is chosen for the calculations.

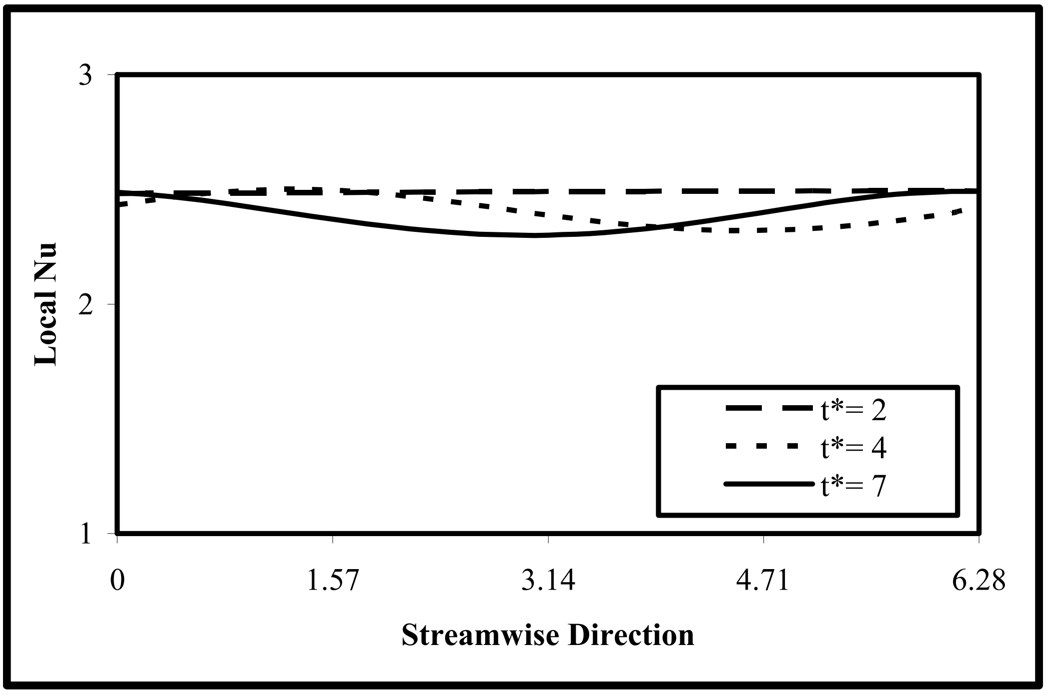

**Figure 5.44.** Local Nu value in streamwise direction where $Ra\cos\varphi = 10000$ and $\varphi = 15^\circ$ with $64 \times 128 \times 64$ grid arrangement

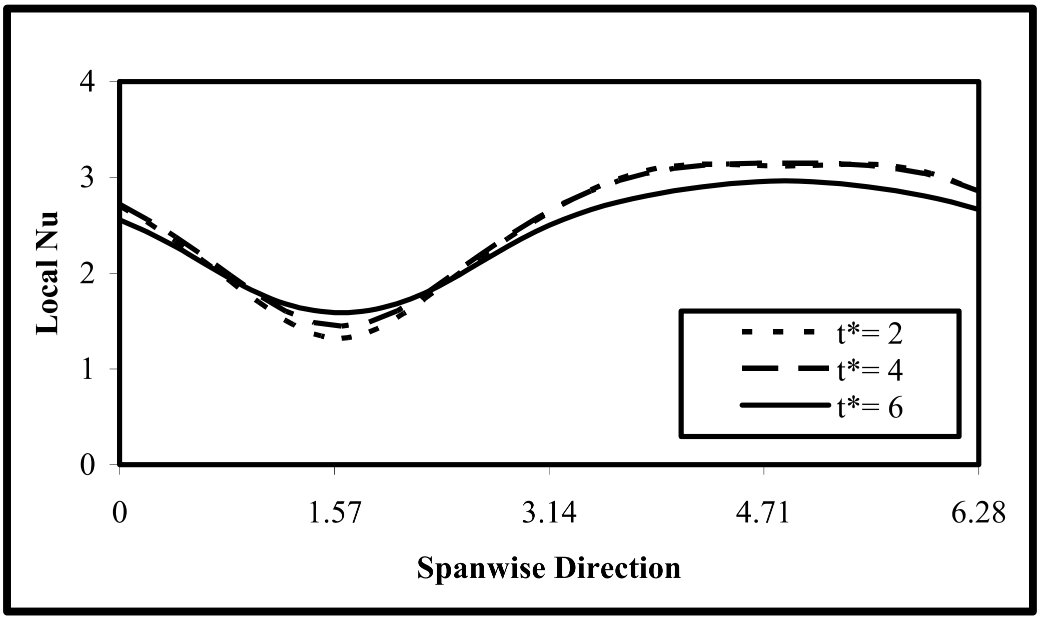

**Figure 5.45.** Local Nu value in spanwise direction where $Ra\cos\varphi = 10000$ and $\varphi = 15^\circ$ with $64 \times 128 \times 64$ grid arrangement

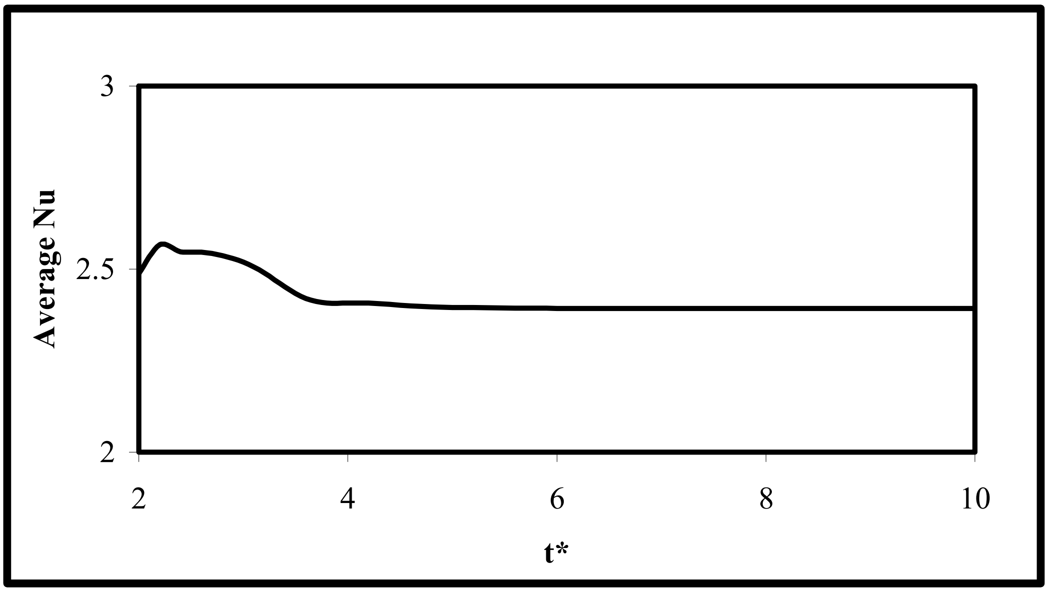

**Figure 5.46.** Average Nu value versus $t^*$ where $Ra\cos\varphi = 10000$ and $\varphi = 15^\circ$ with $64 \times 128 \times 64$ grid arrangement

## 5.7. Critical Tilt Angle Analysis

In order to calculate the critical tilt angle, several successive runs for a specified case at different angles should be performed. For this reason, to save the run time, two dimensional inclined channel case is preferred. The critical tilt angle can be defined as the angle where the flow mode transition occurs. According to the literature, when the channel is inclined from the horizontal, maximum heat transfer occurs at the smaller angles because of the tight alignment of the convection rolls. Furthermore, when the tilt angle is increased, spanwise convection rolls become dominant and streamwise rolls starts to break down. This decreases the heat transfer and at some inclination angle minimum Nu is obtained. At this point, spanwise convection rolls start to rotate their axes by 90 degrees to the direction of z-axis. Finally, these cells merge themselves to a single two dimensional roll with its axis in z-direction. For 2-D runs, $Ra$ is chosen as 20000 and Pr is taken as 0.7 for air. Runs are performed for the inclination angles of $45^\circ$, $60^\circ$, $65^\circ$ and each angle from $70^\circ$ to $80^\circ$. Figure 5.47 illustrates the variation of average Nu with respect to tilt angle for 2-D inclined channel case. The results are smaller than unity and decrease with the increasing tilt angle. This observation shows that natural convection in an inclined channel cannot be considered as two dimensional because Nu cannot be smaller than unity. Nevertheless, the trend of decreasing Nu is caught by 2-D runs, but in order to be sure about the critical tilt angle 3-D runs should also be performed.

Figure 5.48 shows the variation of the average Nu values when $Ra\,cos\,\varphi = 3500$. It is three dimensional analysis and because of the long run times, only the angles between $65^\circ$ and $80^\circ$ are analyzed. The continously decreasing trend can not be achieved because of the constant $Ra\,cos\,\varphi$ term, since when the tilt angle is increased Ra is also increased. Nonetheless, a decline of Nu at an angle is reached and approximately $76^\circ$ can be accepted as the critical tilt angle where Nu is minimum.

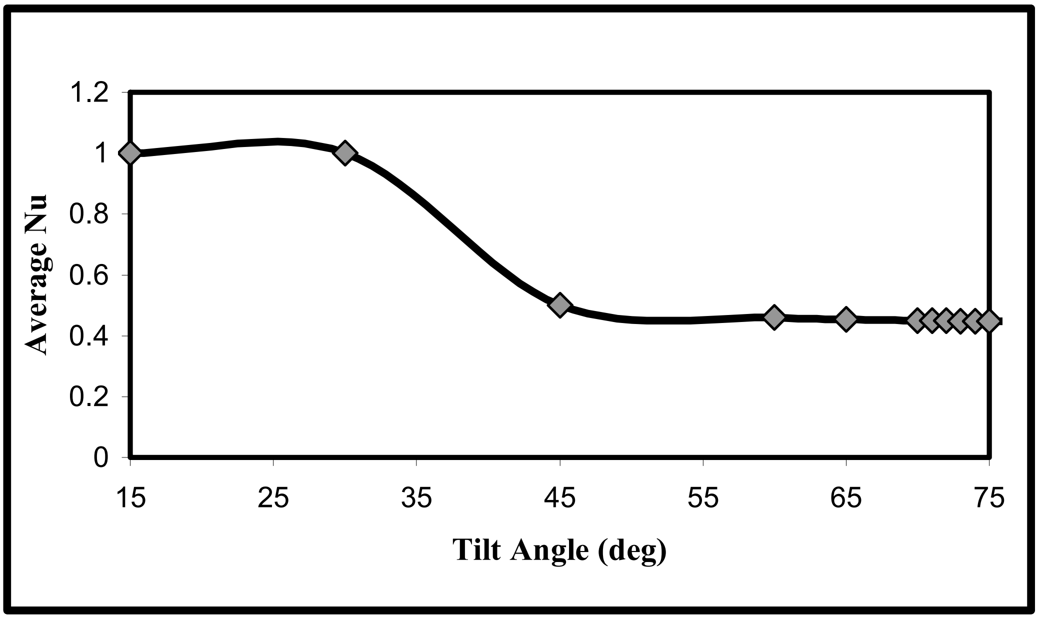

**Figure 5.47.** Average Nu value versus tilt angle for $Ra = 20000$ and $\Pr = 0.7$ for two dimensional case

**Figure 5.48.** Average Nu versus tilt angle when $Ra\cos\varphi = 3500$ for three dimensional case

# CHAPTER 6

# CONCLUSION

Three dimensional natural convection flow and heat transfer between two inclined parallel plates are analyzed by using spectral methods. The channel is heated from the lower plate and both plates are at different but constant temperatures. Periodic boundary conditions are used in streamwise and spanwise directions. No slip and incompressibility assumptions together with Boussinesq approximation are also used. The fluid is taken as air and since air is quiescent in the medium, it is disturbed by using an initial perturbation to its temperature field at a specified point in order to initiate the solver. By considering all these assumptions and approximations, Navier-Stokes equations together with the thermal energy equation are solved using a pseudospectral technique.

In order to compare the results with the literature, average Nu values are calculated and they are plotted with respect to $Ra\,cos\,\varphi$. Additionally, local Nu values, non-dimensional velocities and streamlines are also plotted to understand the flow characteristics in streamwise and spanwise directions more clearly. The study of Hollands et al. [4] is taken as a benchmark in this area, for this reason, the runs are performed for the cases mentioned in their study. $Ra\,cos\,\varphi$ is taken as 1708, 10000, and 50000 for each inclination angle of $\varphi$ as $15^\circ, 30^\circ, 45^\circ$, and $60^\circ$. Additionally, $Ra\,cos\,\varphi = 20000$ is investigated for $\varphi$ values of $15^\circ, 30^\circ,$ and $45^\circ$ and $Ra\,cos\,\varphi = 3500$ is chosen to examine for $\varphi = 60^\circ$. In the experimental study of Hollands et al.[4], $Ra\,cos\,\varphi$ was taken within a broader range of values, i.e. between 1708 and $10^5$. However, since the flow is three dimensional and run time is accordingly long, only four values of $Ra\,cos\,\varphi$ can be considered in this study.

On the other hand, the interval between them is taken somewhat large to see the results in a larger margin.

When $Ra\,cos\,\varphi = 1708$ is taken into account, it was proven in the literature that this number is the critical value for the transition from pure conduction to the convective regime. As expected before, the converged Nu value for this case is found as unity and from Figure 5.5, it is clearly understood that there are no convection rolls between the plates.

When $Ra\,cos\,\varphi$ is increased to 10000, convective rolls are examined especially in the spanwise direction in a wavy manner. These flow characteristics differ with respect to the inclination angle, too. For example, when the tilt angle is $15^\circ$ for this value of $Ra\,cos\,\varphi$, local Nu results in x direction reach to a constant steady state value; on the other hand, when the tilt angle is increased to $30^\circ$, a periodic steadiness is observed. As can be seen from Figure 5.15, local Nu values in the streamwise direction converge by making periodic fluctuations. From Figure 5.17, it can be readily observed that multiple pairs of convective rolls in spanwise direction cause local Nu results in z direction to oscillate more compared to $\varphi = 15^\circ$ results. According to the literature studies, this fact can be presented as follows. When the flow propagates in the streamwise direction, because of the inclination angle and normal buoyancy force, flow starts to make a wave like motion in the spanwise direction. This motion results in upwash and downwash zones of heat transfer. This provides Nu values to construct two extreme points along the spanwise direction. Figure 5.17 shows these wave like motion clearly.

When $Ra\,cos\,\varphi$ is increased to 50000 for $\varphi = 30^\circ$, the streamlines in streamwise direction should be examined carefully. After the half length of the channel, longitudinal wavy motions are observed, thus the flow becomes more complicated. For this reason, convergence becomes very hard to achieve for this type of problem and average Nu values start to oscillate more.

According to the observations mentioned above, it can easily be concluded that Nu values do not only depend on $Ra\,cos\,\varphi$, they also depend on the inclination angle. This phenomenon was observed and included to Eqn. 5.8 by adding a function related to inclination angle to Eqn. 5.9 in the study of Hollands et al. [4].

The average Nu values with respect to $Ra\,cos\,\varphi$ are plotted and the results are compared with Eqns. 5.8-9. In Table 5.1, the results and the relative error percentages are tabulated and it can be stated that for the cases that convergence is achieved, the results of the present study agree well with the ones of the experimental study. However, especially for $\varphi = 60^\circ$ when $Ra\,cos\,\varphi = 10000$ and $Ra\,cos\,\varphi = 50000$, the results deviate between 22 and 28 percent from the results of the experimental study.

The grid independence is searched by increasing the collocation points by doubling them in all three directions. Nu values improved considerably, however the run time increases from two days to one week for each case. For this reason, collocation points are halved in three directions also, and it is observed that $32 \times 64 \times 32$ meshes have approximately the same results with $16 \times 32 \times 16$ grid arrangements. Moreover, approximately five or seven percent difference occurs between the meshes of $32 \times 64 \times 32$ and $64 \times 128 \times 64$. Since this is an acceptable error margin and in order to decrease the run-time, $32 \times 64 \times 32$ grid arrangement is preferred for the calculations. The critical tilt angle analysis is also done in this study and minimum Nu is obtained for the three dimensional case.

Some recommendations can also be made about the present study. Especially, in order to achieve convergence for higher $Ra\,cos\,\varphi$ and $\varphi$, the time increments should be decreased enough and time end of the program has to be increased. Additionally, another time discretization method can be used for this study. The other remedy is increasing the numbers of collocation points at least from $32 \times 64 \times 32$ to $64 \times 128 \times 64$. For this purpose, more developed computers should be preferred and parallel computations should be made.

# REFERENCES

[1] Kakac, S., and Yener, Y., Convective Heat Transfer, 2nd Edition, CRC Press, 1995.

[2] Gebhart, B., Jaluria, Y., Mahajan, R., and Sammakia, B., Buoyancy-Induced Flows and Transport, Textbook Edition, Hemisphere Publishing Corporation, 1988.

[3] Ruth, D. W., Hollands, K. G. T., and Raithby, G. D., On free convection experiments in inclined air layers heated from below, *J.Fluid Mech.*, 1980, 96 (3), 461-479.

[4] Hollands, K. G. T., Unny, T. E., Raithby, G. D., and Konicek, L., Free Convective Heat Transfer Across Inclined Air Layers, *ASME Journal Of Heat Transfer*, May 1976, 98, 189-193.

[5] ElSherbiny, S. M., Hollands, K. G. T., and Raithby, G. D., Effect of Thermal Boundary Conditions on Natural Convection in Vertical and Inclined Air Layers, *ASME Journal of Heat Transfer*, Aug. 1982, 104, 515-520.

[6] Dropkin, D., and Somerscales, E., Heat Transfer by Natural Convection in Liquids Confined by Two Parallel Plates Which are Inclined at Various Angles With Respect to the Horizontal, *Journal Of Heat Transfer, TRANS. ASME, Series C.,* Feb. 1965, 87, 77-84.

[7] ElSherbiny, S. M., Raithby, G. D., and Hollands, K. G. T., Heat Transfer by Natural Convection Across Vertical and Inclined Air Layers, *ASME Journal of Heat Transfer*, Feb.1982, 104, 96-102.

[8] Ozoe, H., Sayama, H., and Churchill, S.W., Natural Convection in an Inclined Rectangular Channel at Various Aspect Ratios and Angles-Experimental Measurements, *Int. J. Heat Mass Transfer,* 1975, 18, 1425-1431.

[9] Azevedo, L. F. A., and Sparrow, E. M., Natural Convection in Open-Ended Inclined Channels, *ASME Journal of Heat Transfer*, Nov. 1985, 107, 893-901.

[10] Inaba, H., Experimental Study of Natural Convection in an Inclined Air Layer, *Int. J. Heat Mass Transfer,* 1984, 27 (8), 1127-1139.

[11] Onur, N., Sivrioglu, M., and Aktas, M. K., An experimental study on the natural convection heat transfer between inclined plates (Lower plate isothermally heated and the upper plate thermally insulated as well as unheated), *Heat and Mass Transfer*, 1997, 32, 471-476.

[12] Onur, N., and Aktas, M. K., An Experimental Study on the Effect of Opposing Wall on Natural Convection Along an Inclined Hot Plate Facing Downward, *Int. Comm. Heat Mass Transfer*, 1998, 25 (3), 389-397.

[13] Ozoe, H., Fujii, K., Lior, N., and Churchill, S. W., Long Rolls Generated by Natural Convection in an Inclined, Rectangular Enclosure, *Int. J. Heat Mass Transfer*, 1983, 26 (10), 1427-1438.

[14] Ozoe, H., Yamamoto, K., and Churchill, S.W., Three-Dimensional Numerical Analysis of Natural Convection in an Inclined Channel with a Square Cross Section, *A.I.Ch.E. Jl,* July 1979, 25 (4), 709-716.

[15] Yang, H.X., and Zhu, Z.J., Numerical Study on Transient Laminar Natural Convection in an Inclined Parallel-Walled Channel, *Int. Comm. Heat Mass Transfer*, 2003, 30 (3), 359-367.

[16] Baskaya, S., Aktas, M. K., and Onur, N., Numerical simulation of the effects of plate separation and inclination on heat transfer in buoyancy driven open channels, *Heat and Mass Transfer*, 1999, 35, 273-280.

[17] Fujii, T., and Imura, H., Natural Convection Heat Transfer from a Plate with Arbitrary Inclination, *Int. J. Heat Mass Transfer,* 1972, 15, 755-767.

[18] Shaukatullah, H., and Gebhart, B., An Experimental Investigation of Natural Convection Flow on an Inclined Surface, *Int. J. Heat Mass Transfer,* 1978, 21, 1481-1490.

[19] Cheng, K. C., and Kim, Y. W., Flow Visualization Studies on Vortex Instability of Natural Convection Flow Over Horizontal and Slightly Inclined Constant-Temperature Plates, *ASME Journal of Heat Transfer*, Aug. 1988, 110, 608-615.

[20] Zuercher, E. J., Jacobs, J. W., and Chen, C. F., Experimental study of the stability of boundary-layer flow along a heated, inclined plate, *J.Fluid Mech.*, 1998, 367, 1-25.

[21] Kierkus, W. T., An Analysis of Laminar Free Convection Flow and Heat Transfer about an Inclined Isothermal Plate, *Int. J. Heat Mass Transfer,* 1968, 11, 241-253.

[22] Haaland, S. E., and Sparrow, E.M., Vortex Instability of Natural Convection Flow on Inclined Surfaces, *Int. J. Heat Mass Transfer,* 1973, 16, 2355-2367.

[23] Chen, T. S., and Tzuoo, K. L., Vortex Instability of Free Convection Flow Over Horizontal and Inclined Surfaces, *ASME Journal of Heat Transfer*, Nov. 1982, 104, 637-643.

[24] Lin, M., Numerical study of formation of longitudinal vortices in natural convection flow over horizontal and inclined surfaces, *Int. J. Heat Mass Transfer,* 2001, 44, 1759-1766.

[25] Jeschke, P., and Beer, H., Longitudinal vortices in a laminar natural convection boundary layer flow on an inclined flat plate and their influence on heat transfer, *J.Fluid Mech.*, 2001, 432, 313-339.

[26] Biertümpfel, R., and Beer, H., Natural convection heat transfer increase at the laminar-turbulent transition in the presence of instationary longitudinal vortices, *Int. J. Heat Mass Transfer,* 2003, 46, 3109-3117.

[27] Peyret, R., Spectral Methods for Incompressible Viscous Flow, Springer-Verlag New York, 2002.

[28] Boyd, J. P., Chebyshev and Fourier Spectral Methods, 2nd Edition, Revised, Dover Publications, 2001.

[29] Canuto, C., Hussaini, M. Y., Quarteroni, A., and Zang, T. A., Spectral Methods in Fluid Dynamics, Springer-Verlag Berlin Heidelberg, 1988.

[30] Kim, J., Moin, P., and Moser, R., Turbulence Statistics in Fully Developed Channel Flow at Low Reynolds Number, *J.Fluid Mech.,* Apr. 1987, 177, 133-166.

[31] Zhang, S. Q., and Tangborn A. V., Flow Regimes in 2-Dimensional Mixed Convection with Spatially Periodic Lower Wall Heating, *Physics of Fluids,* Oct. 1994, 6 (10), 3285-3293.

[32] Tari, I., Spherical Particle Motion Simulation by Spectral Methods, *Ph.D. Thesis*, Northeastern University Dept. of Mech. Indust. and Manuf. Eng. , Boston, MA, 1998.

[33] Greengard, L., Spectral Integration and 2-Point Boundary Value Problems, *SIAM Journal on Numerical Analysis*, Aug. 1991, 28 (4), 1071-1080.